NP-14538

Quarterly Technical Summary Report
on
DIRECT ENERGY CONVERSION SYSTEMS

Prepared for
Advanced Research Project Agency
Director of Material Sciences

Submitted by
Robert H. Eustis, Principal Investigator

For the Period
1 June 1964 - 31 August 1964

ARPA Order Number:	246, Amendment 6
Program Code Number:	3980
Name of Contractor:	Board of Trustees of the Leland Stanford Junior University
Date of Contract:	1 November 1961
Contract Number:	AF 49(638)-1123
Contract Expiration Date:	31 August 1964

September 30, 1964
Stanford, California

STANFORD UNIVERSITY ■ STANFORD, CALIFORNIA

TABLE OF CONTENTS

ABSTRACT

The MGD generator electrode materials problem has been greatly simplified by introducing cooling water into the electrode stems. Runs of over one-half hour duration indicate a negligible recession of the surface so that the same electrodes can be used for several runs. Electrical data from the generator indicates a diffuse current with an applied electric field for currents up to about 10 amperes per electrode (current density of about 1 amp/cm^2). Current leakage through the insulating brick has been examined and some changes in brick design and material are being made to reduce this leakage.

A more complete report than that previously given is made of the investigation of the influence of the Ramsauer effect on nonequilibrium electron temperatures. This report is a preprint of a Research Note that will appear in the Physics of Fluids.

The calculation of electrical conductivity by the Chapman-Enskog method has been compared to the method of Frost. Very satisfactory agreement has been shown and the assumptions of Frost have been given a more rigorous foundation.

Diagnostic methods have been improved with the development of the spectroscopic line reversal technique. Temperature measurements believed accurate to $\pm$ 10°K have been made in seeded flames.

An investigation of the effect of free stream turbulence on the limiting current density at the front stagnation point of a translating cylinder electrode was undertaken. An effect of the cylinder diameter and whether the electrode was cathodic or anodic was observed.

INTRODUCTION

The present report is the fourth quarterly technical report written under supplemental agreement 2(63-604) to Contract AF 49(638)-1123 which is supported by the Advanced Research Projects Agency. Described in this report is a research effort including studies of magnetogasdynamic and fuel cell energy conversion. This effort involves faculty and students in the departments of Mechanical Engineering, Aeronautical Engineering, Chemical Engineering and Chemistry. The faculty members contributing to the program are as follows.

<u>Magnetogasdynamics</u>	
Channel	Professor R. H. Eustis Professor C. H. Kruger Dr. M. Mitchner
Shock Tube	Professor D. Bershader
<u>Fuel Cells</u>	
Kinetic Studies	Professor D. Mason Dr. P. van Rysselberghe
Chemisorption Studies	Professor E. Hutchinson

In addition to this report, two supplementary reports are included which conclude a particular topic of research. These reports are the following:

Supplementary Report Number 1, "Heat and Mass Transfer From the Surface of a Cylinder with Discontinuous Boundary Conditions to an Incompressible Laminar Flow", by Zeev Rotem and David M. Mason.

Supplementary Report Number 2, "Transport Properties of Partially Ionized Monatomic Gases", Steve deVoto and Daniel Bershader.

With this report, the work supported by contract AF 49(638)-1123 on fuel cells and on shock heated plasmas is concluded. Research in these areas is summarized in the present report and detailed descriptions are given in the supplementary reports as well as in previous Quarterly Reports. Work is continuing on studies related to Magneto-gasdynamics energy conversion in a combustion driven generator.

I. MAGNETOGASDYNAMICS

A. Continuous Flow Channel

1) Power Generation - As discussed in the last progress report, the most satisfactory overall generator performance had been achieved with uncoated type 316 stainless steel and molybdenum electrodes. The estimated surface temperatures of these materials during operation were respectively 1800°F and 2200°F, and the exposed surface area of each electrode was 0.4" by 1-1/4".

The first run of the power generation apparatus in the current report period incorporated type 316 stainless steel for all 26 electrode heads. The exposed surface area of each electrode head was 3/4" in the flow direction by 1-1/4" normal to the flow direction. Boron nitride insulating spacers 1/32" thick were used between the backside of the electrode heads and the metallic housing to increase heat transfer and reduce the electrode temperature. In addition to investigation of electrode behavior, the purpose of this test was to measure gas conductivity and leakage resistances.

The following nominal run conditions were used:

combustion-gas flow rate	0.13 lb/sec-in^2
oxidizer to alcohol ratio	stoichiometric
N_2/O_2 ratio	1.0 by weight
seed fraction	0.01 K by weight
inlet stagnation temperature	2700°K
static pressure at exit	1 atm
gas cross-sectional area	5.5 in^2
electrode separation distance	4.4 in
magnetic field intensity	0

Measurements of electrical resistances were made during the preheat and post heat phases (low flow, propane fuel) as well as during the principal run. Data were recorded for resistances from anode to ground (test section housing), cathode to ground, and anode to cathode, in all 13 circuits. Electrical currents during the preheat phase were so low as to produce no ammeter deflections, indicating leakage resistances of at least several thousand ohms under these relatively low temperature, no-seed conditions.

The first 12 minutes of the principal run were occupied by the usual warmup phase followed by recording of voltage-current loading characteristics of all the 13 circuits. The data from each circuit exhibited linear characteristics up to currents of 8-10 amps per circuit. The single data point for the highest applied voltage indicated a corresponding lowering of internal resistance at 10 of the 13 circuits. The loading curve for the central circuit is shown in Figure 1. The average resultant gas resistance at each circuit, estimated from the slope of the loading curves and accounting for the subsequently measured leakage resistances, is approximately 24 ohm. This resistance corresponds to an effective gas conductivity of 3.9 mho/meter. Unfortunately, the conductivity of the hot gas core cannot be determined from this run because wiring from the sidewall-potential probes was apparently destroyed early in the run by gas flow behind the sidewall brick.

One set of data on leakage resistance from electrode to ground was obtained at a run time of 11.5 min. These data, obtained for an applied potential of 70 volts, indicated corresponding leakage resistances ranging from approximately 30 ohm to 400 ohm, depending on circuit location. The central circuits had the highest leakage resistances. Application of a higher potential between electrodes and ground resulted in the blowing of fuses in several circuits making interpretation of subsequent data difficult.

Steady-state temperature data from thermocouples in the MgO sidewall brick were extrapolated to give a surface temperature of approximately 3500°F. Based on data from thermocouples inside the electrode heads, electrode surface temperature ranged from approximately 1400°F to 2000°F, depending on electrode location. Total run time under the previously tabulated flow conditions was 26 minutes.

Examination of the test section after this run showed a dark electrically-conductive deposit on all electrodes and adjacent MgO brick walls. Recession of most electrodes was less than 0.01", but a few had locally receded up to 0.04". Several pits, apparently caused by local arcing, were present in the metallic wall of the test section. The pits seemed to exist at gaps between the boron nitride spacers (see above). In all cases the pits were adjacent to electrode heads in those circuits containing the fuses blown during the measurement of leakage resistances.

Although the electrode lifetime in this test was adequate the associated deposition of contaminant on the inter-electrode brick would short the Hall field in power generation runs. Thermal analysis showed that stainless steel electrodes cannot be run much cooler than in the above test unless the cooling medium is brought close to the entire heated face. It was decided that direct water cooling of the electrodes was required.

The design finally selected is illustrated in Figure 2. It consists of a molybdenum head cooled by conduction to a water-cooled copper shank. The molybdenum head can operate at average surface temperatures several hundred degrees F lower than a similar stainless steel head, due to the large difference in thermal conductivities of the two materials. The head and shank of the electrode are connected by a threaded joint; powdered graphite is added to this joint during assembly in order to improve contact.

The subsequent power generation run incorporated 26 of the electrodes shown in Figure 2. The head size was again 3/4" by 1-1/4". Two types of molybdenum were used: one was commercially pure, sintered molybdenum and the other was a

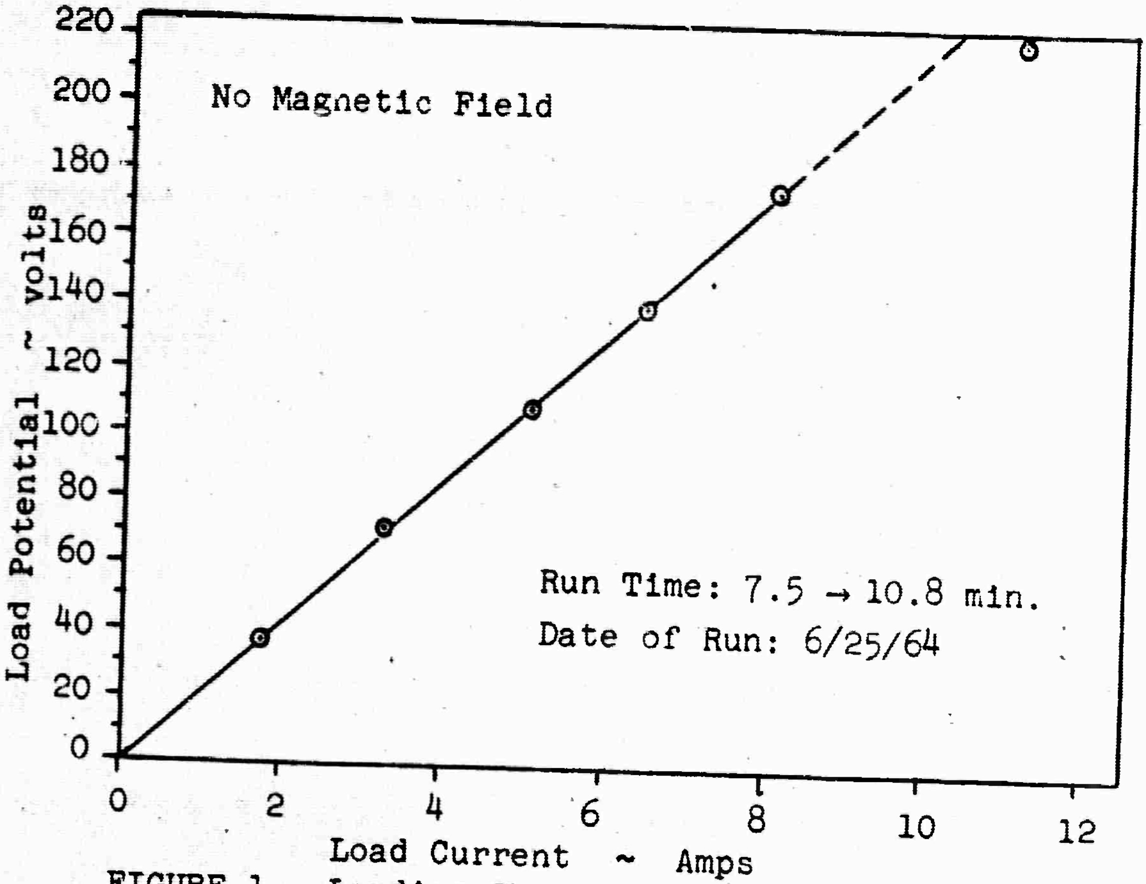

FIGURE 1 Loading Characteristics, Load Circuit #7

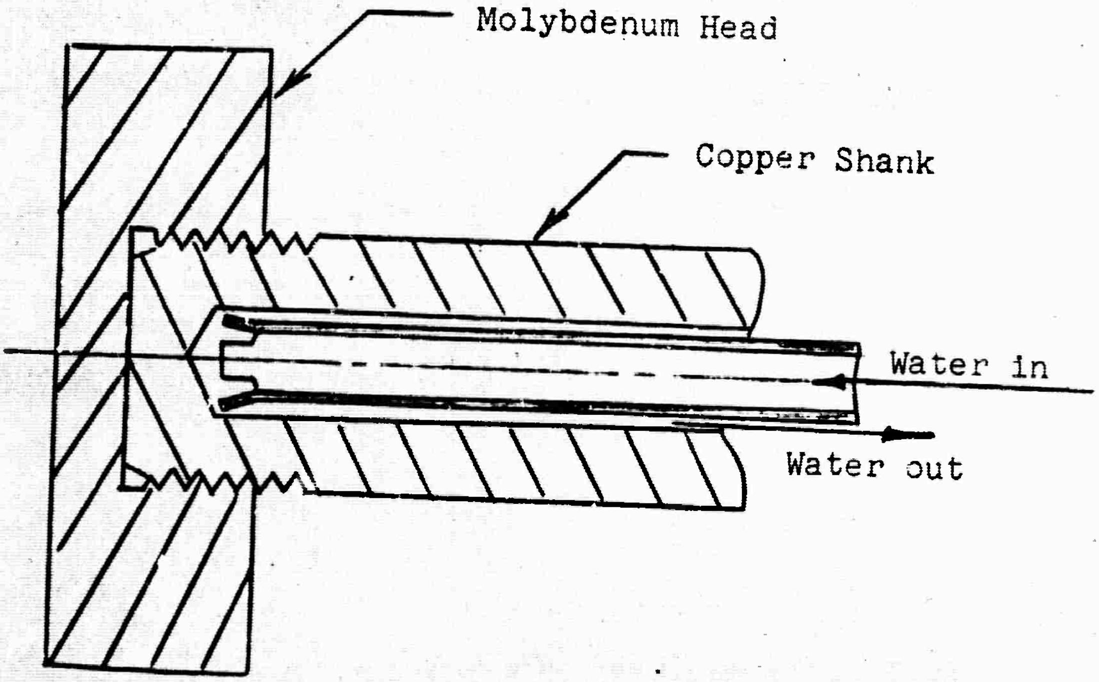

FIGURE 2 Water-Cooled Electrode Used in Run of 8/19/64

titanium-zirconium, arc-cast TZM alloy. MgO spacers, 1/4" thick, were used between the heads and the test section metallic housing (same as in all previous tests except the last one). An attempt was made to electrically insulate the test section and diffuser from the gas flow by applying a 1000°F strain gage cement to all exposed surfaces. The diffuser was also electrically isolated from the test section ground).

The following nominal conditions were used in this run:

combustion-gas flow rate	0.16 lb/sec-in^2
oxidizer to alcohol ratio	stoichimetric
N_2/O_2 ratio	1.0 by weight
seed fraction	0.01 K by weight
inlet stagnation temperature	2700°K
static pressure at exit	1 atm
gas cross-sectional area	5.0 in^2
electrode separation distance	4.0 in
magnetic field intensity	2.6 weber/m^2

The total run time at these conditions was 34 minutes including a 6-1/2 minute interval during which the seeded fuel was replaced by unseeded fuel. At the end of this time, the run was automatically stopped by a flame-out signal from the flame sensor which was caused by an accumulation of opaque deposit on a window in the optical path.

The electrodes withstood the test very well, better than those in any previous test. There was no overall recession which had been typical of electrodes in previous tests. Instead, the heated faces of most electrode heads exhibited local pitting; this pitting occurred over the entire surface of the upstream three pair of electrodes. There was frequent slight head damage, giving the appearance of having been melted, in localities adjacent to the hottest regions of the MgO brick. There was no electrode damage at the interface with cooler regions of the MgO. The heated surface of a few electrodes retained a foreign material which appeared to have flowed from the adjacent upstream MgO spacer. Also, some spacers seemed to have experienced a buildup of material during the test. There was no deposit on/or melting of MgO sidewall brick. Comparison of molybdenum to the TZM alloy is inconclusive.

All leakage resistances measured after the test were several orders of magnitude less than those before the test. For example, the indicated resistance between two adjacent electrodes was: before test - 2 Meg Ω ; after test, with inter-electrode spacer installed - 1000 Ω ; after test, with inter-electrode spacer removed - 4000 Ω .

Temperature was measured at one internal location in each of three molybdenum heads, two in upstream circuit #1 and one in downstream circuit #13. Near the end of the run the corresponding temperatures were approximately 1750°F, 1350°F, and 950°F. Temperatures of the heated surfaces were probably within 100°F of these recorded temperatures.

Internal temperatures were also measured of upstream MgO brick in the test section. These temperatures were relatively constant after warmup. Extrapolations indicate surface temperatures of up to 2800°F on the inter-electrode spacers and about 3500°F on the sidewall.

Figures 3 through 10 present electrical data showing representative behavior of the 13 separate load circuits. More detailed information is presented for two circuits, #2 and #12; these circuits typify the general behavior of circuits in the two halves of the generator. The open-circuit load-potential histories shown in Figure 3 are consistent with previous results. Data indicate that as time increases a gradual decrease in voltage occurs for circuits in the upstream 1/2 to 2/3 of the generator but the voltages remain relatively constant in the downstream circuits. The short-circuit current histories shown in Figure 4 are not as steady as expected. As in previous tests, approximately six minutes were required to reach the apparent steady level; this is consistent with temperature

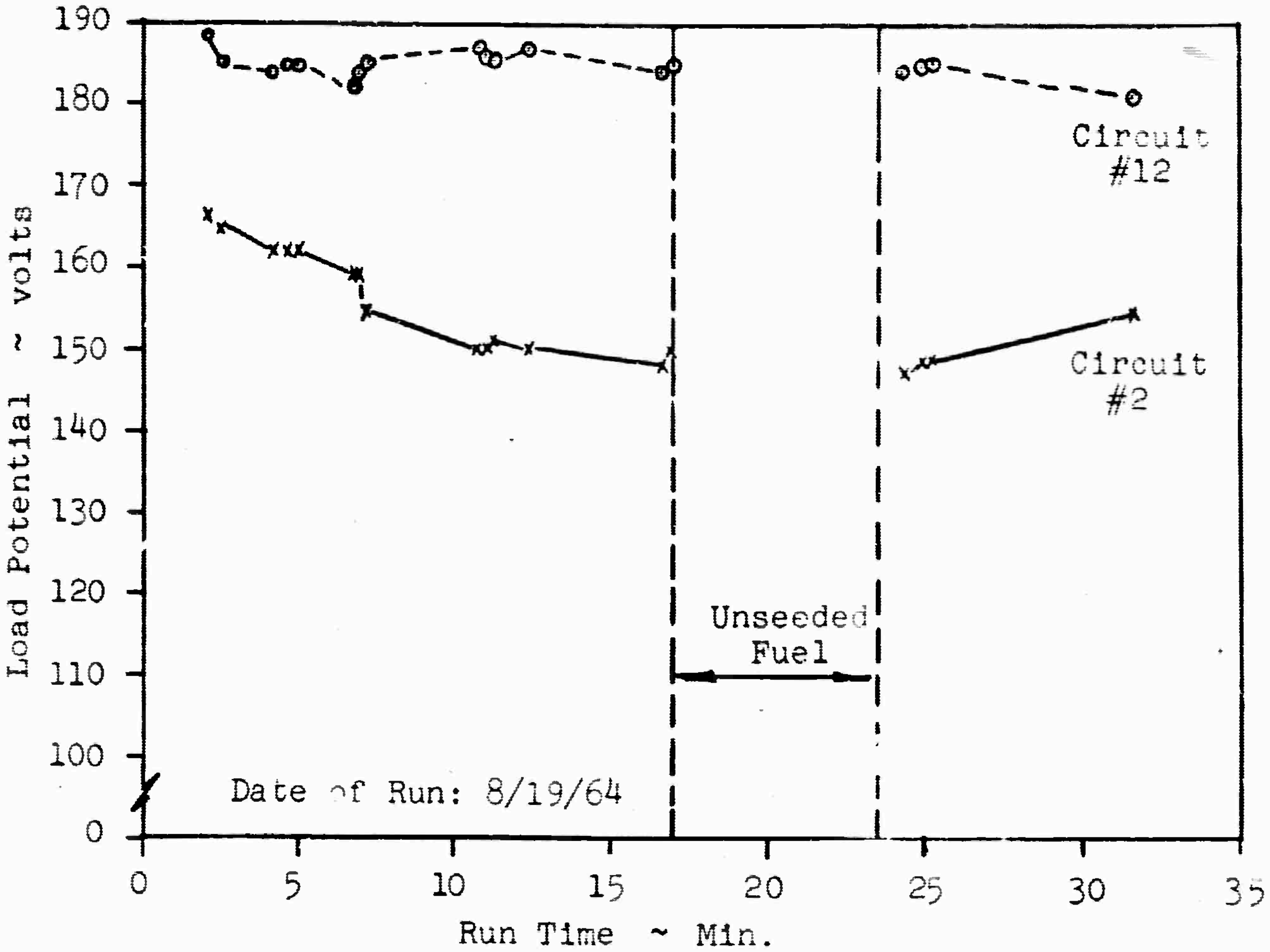

FIGURE 3 Load-Potential History at Open Circuit

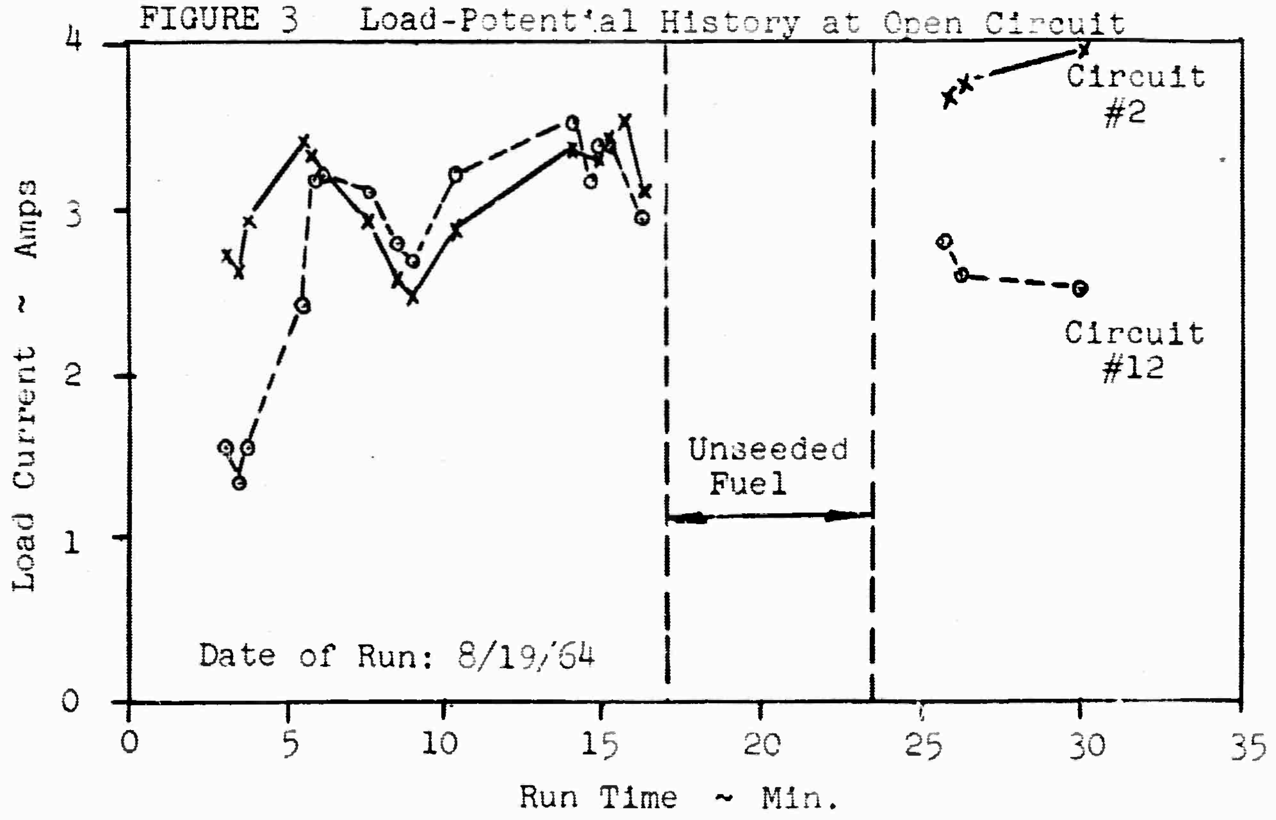

FIGURE 4 Short-Circuit Current History

data from the sidewall brick and cooling water. Comparison of electrical data obtained before and after operation with unseeded fuel have lead only to the conclusion that if a change in leakage resistance occurred during the 6-1/2 minute interval then its effect on open circuit voltage was limited to approximately 2 volts.

Figure 5 presents the axial distribution of open-circuit voltage available to a load. At early times shorting apparently occurred at the center of the generator. All voltage distributions after 3 minutes of running were similar to that shown for 31.5 minutes. Axial distributions of load current at the four loads used in this run are shown in Figure 6. An axial distribution of electrode potential relative to the grounded test section housing is shown in Figure 7 for operation with all circuts essentially short circuited. Figures 5 and 7, and perhaps Figure 6 demonstrate the presence of local shorting within the generator. The difference between electrode potentials at circuts #13 and #1 is herein called the total Hall potential. The measured history of the total Hall potential for those runs with all load circuits shorted is shown in Figure 8. These were the most unsteady data observed in the entire 34 minute run. The expected total Hall potential is 300 volts, based total Hall potential is 300 volts, based on predicted gas properties and measured currents. From Figure 7 it is seen that the expected Hall field was actually achieved between electrodes #7 and #8 and also between electrodes #11 and #13.

Figures 9 and 10 show the loading characteristics of the two circuits for which histories were shown. Most circuits produced more repeatable data and some had significantly more linear characteristics than those shown.

Comparison of loading characteristics and current distribution for all 13 circuits has indicated a sort of equilibrating effect among adjacent electrodes. Frequently a circuit which performed less than the trend was adjacent to a circuit which performed better than the trend. It is therefore meaningful to investigate the cumulative behavior of all circuits in the generator. This is done in Figures 11 and 12.

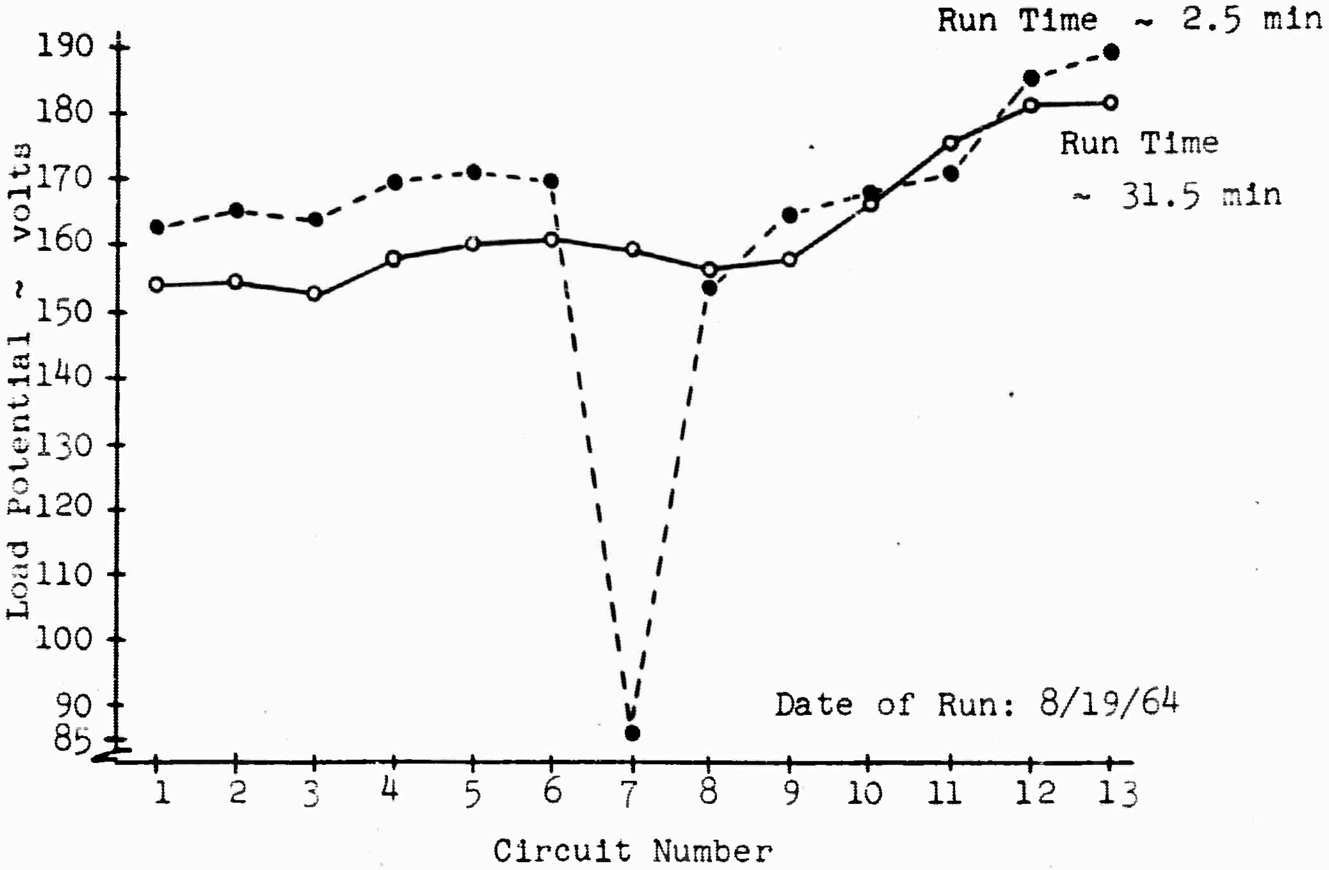

FIGURE 5 Load Potential X-Distribution at Open Circuit

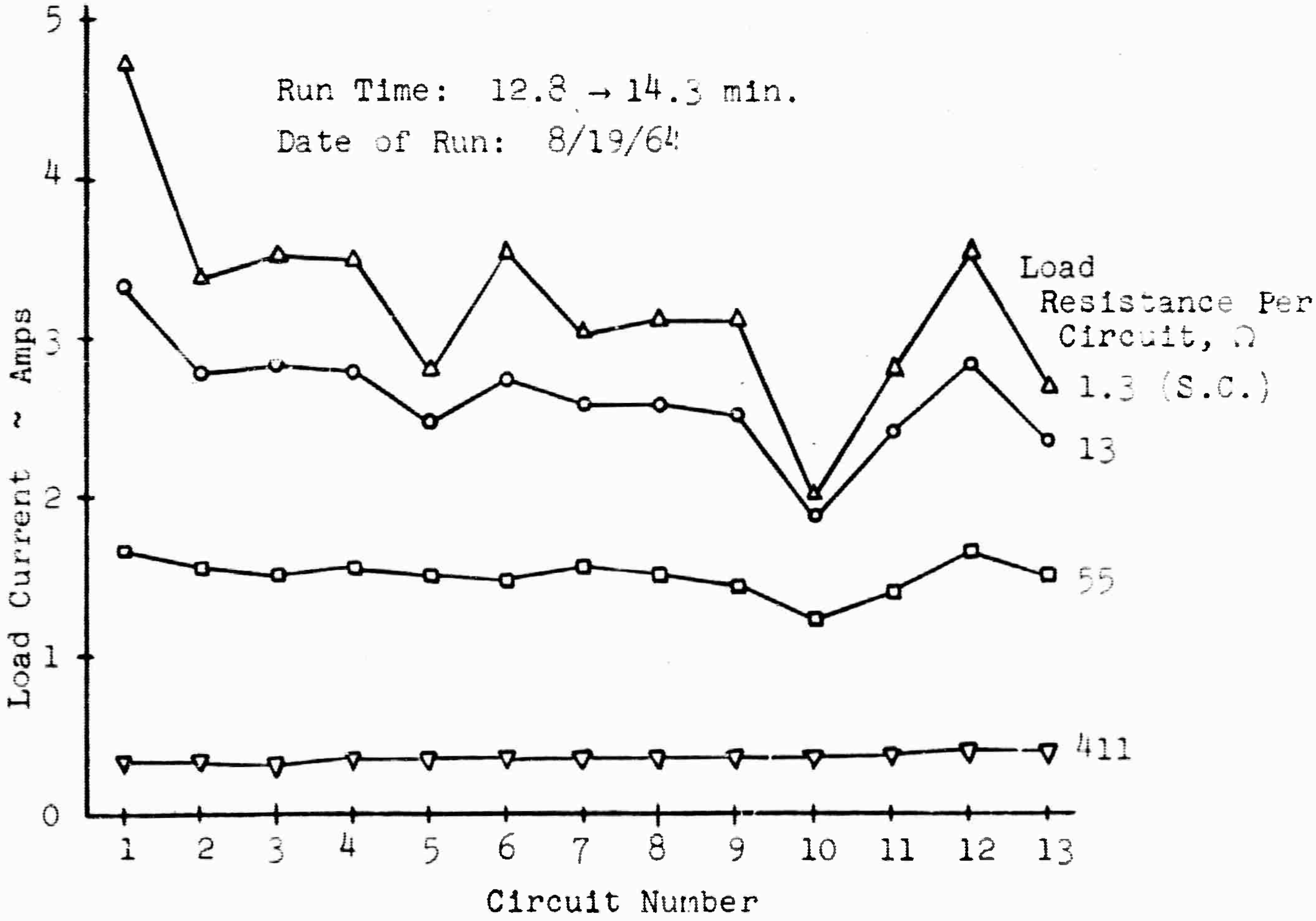

FIGURE 6 Load Current Distribution at Various Loads

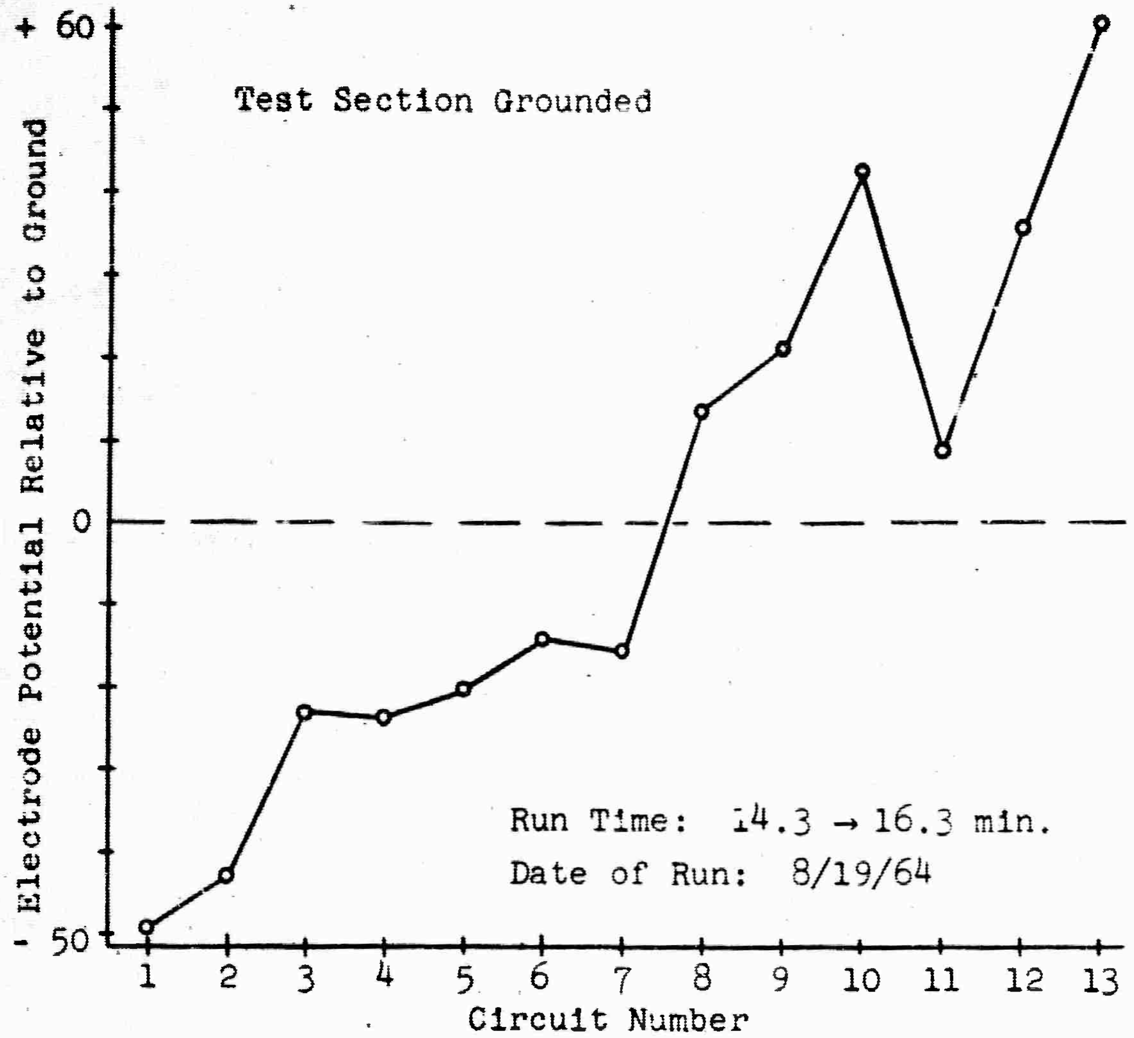

FIGURE 7 Electrode Potential X-Distribution at Short Circuit

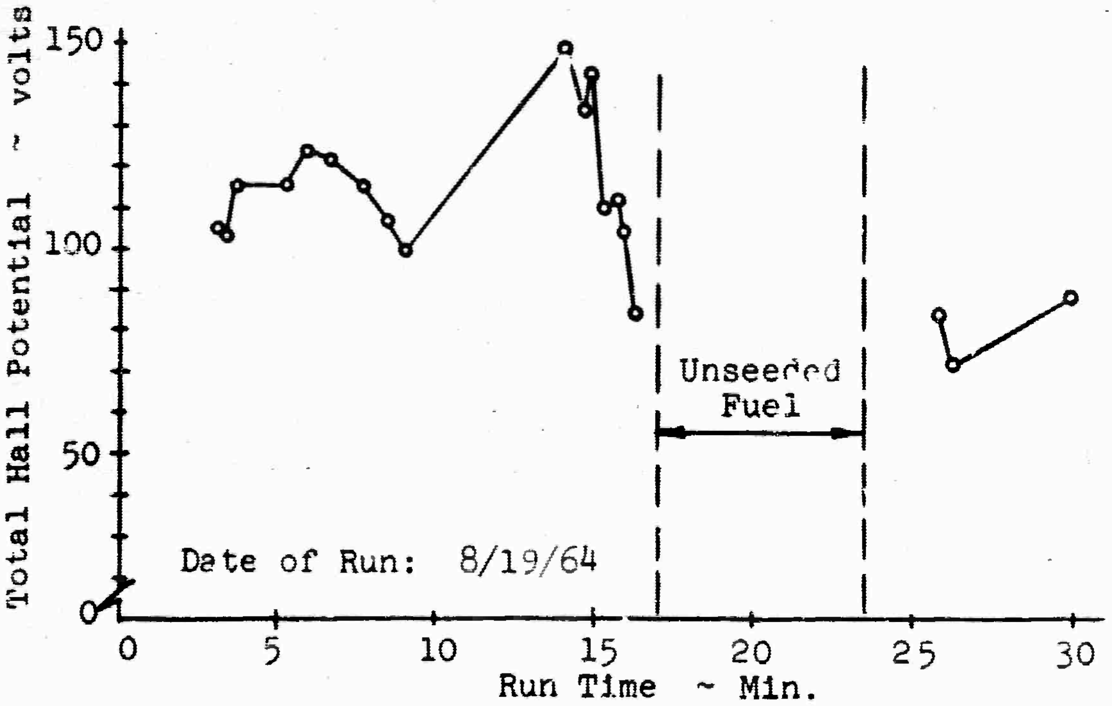

FIGURE 8 Total Hall Poten al History at Short Circuit

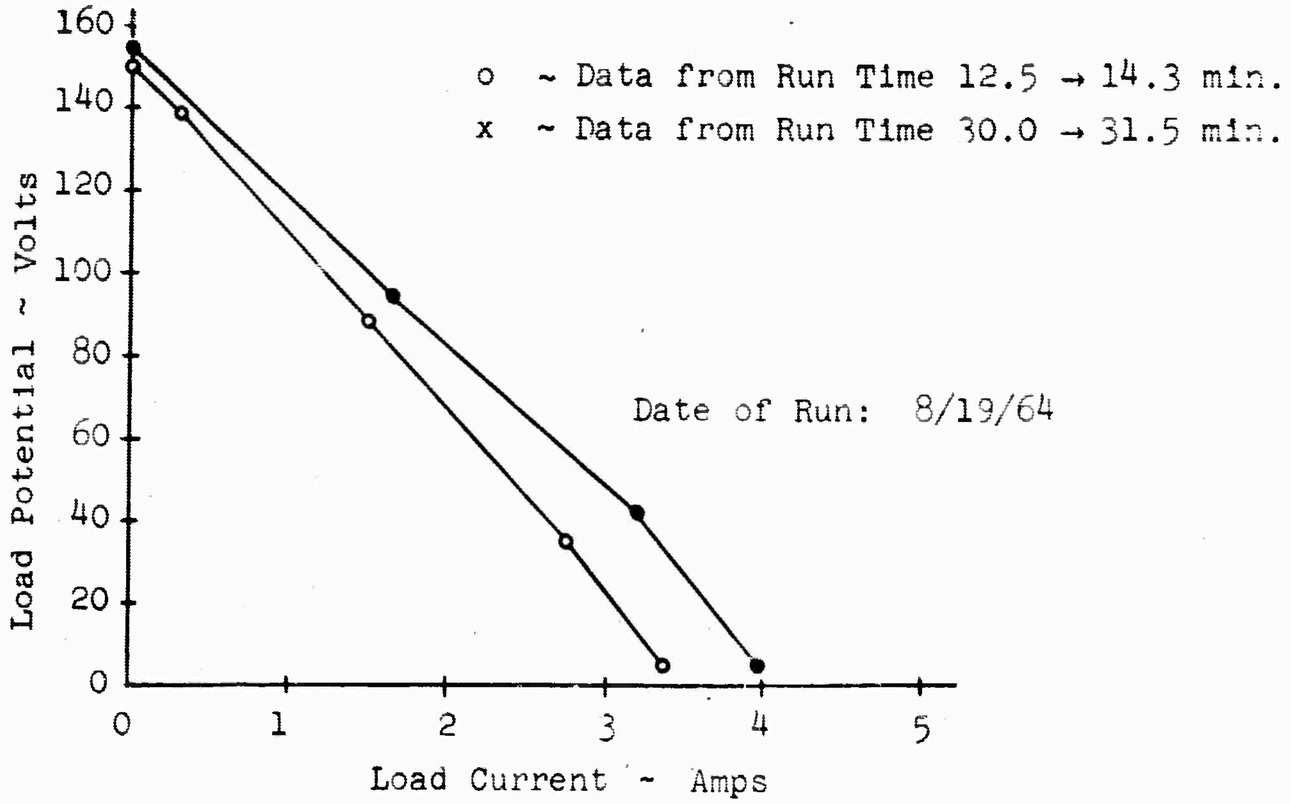

FIGURE 9 Loading Characteristics, Circuit #2

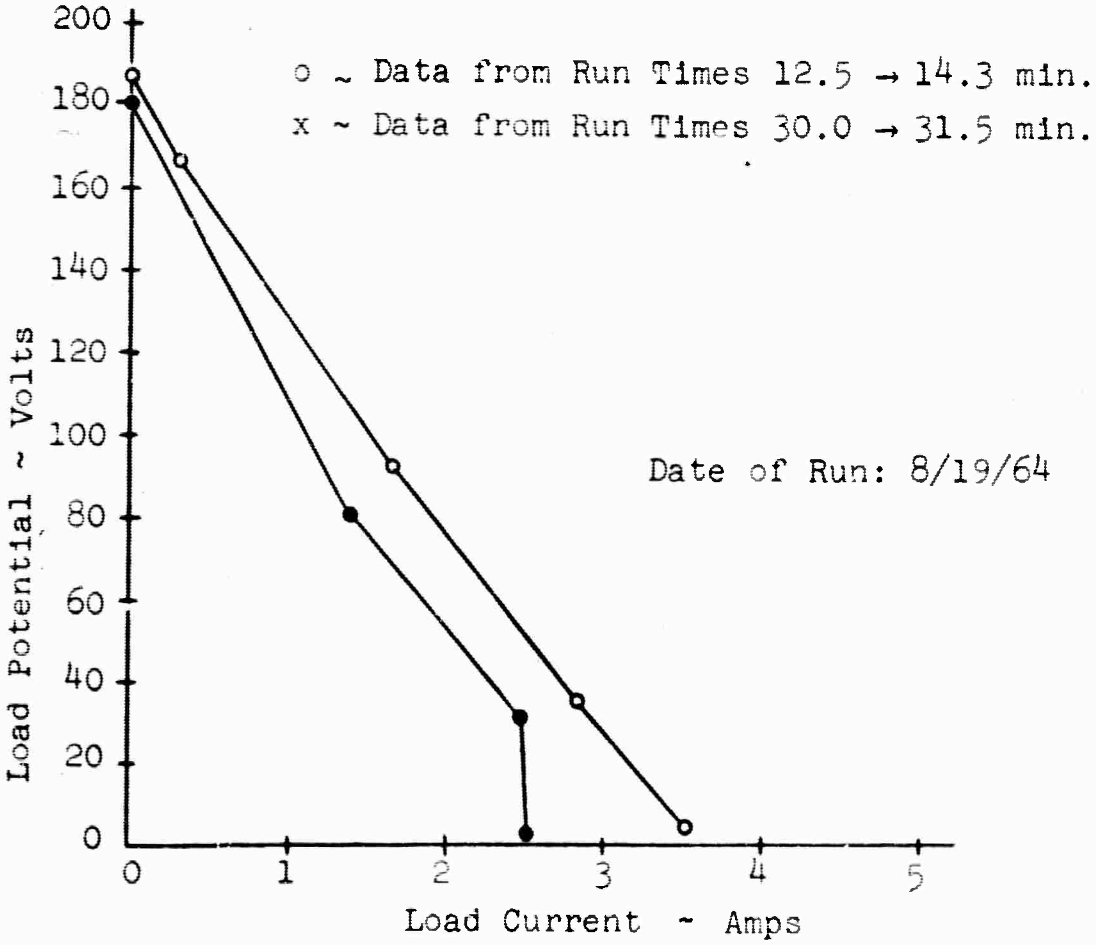

FIGURE 10 Loading Characteristics, Circuit #12

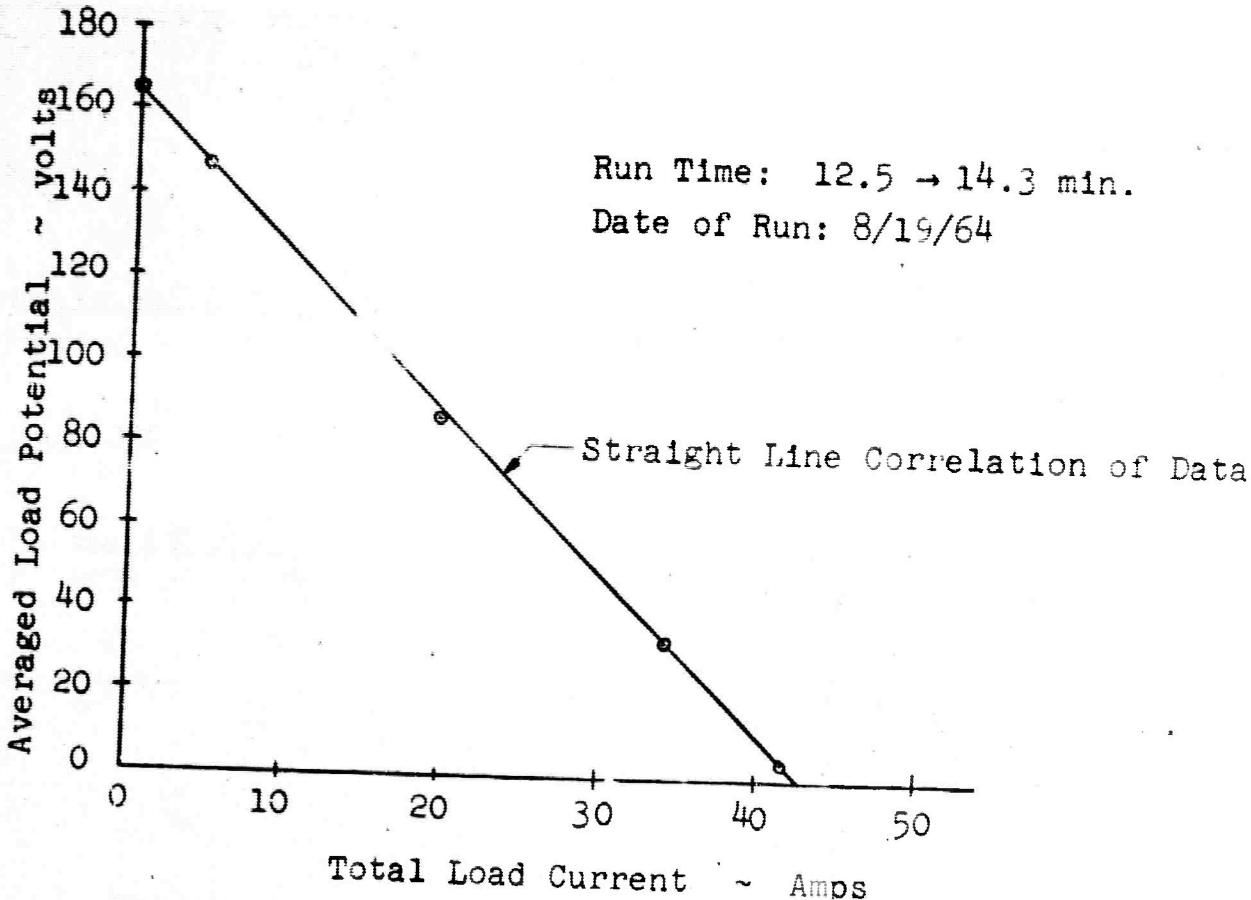

Run Time: 12.5 → 14.3 min.
Date of Run: 8/19/64

Straight Line Correlation of Data

FIGURE 11 Loading Characteristics, Total Generator

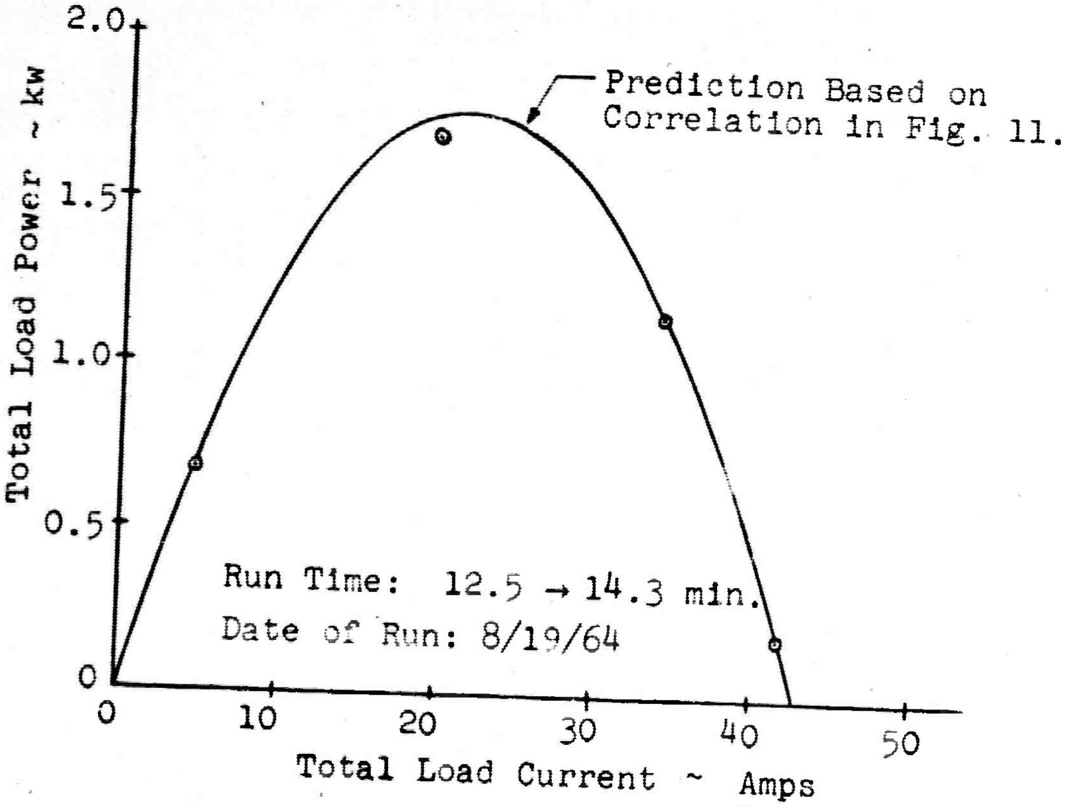

Prediction Based on Correlation in Fig. 11.

Run Time: 12.5 → 14.3 min.
Date of Run: 8/19/64

FIGURE 12 Power Output, Total Generator

Figure 11 presents the averaged loading curve for the total generator. The "Averaged Load Potential" is simply a numerical average of all the 13 simultaneous load voltages, and the "Total Load Current" is the sum of the 13 simultaneous load currents. The straight-line correlation of the data is indicative of constant generator internal resistance, independent of load current. Figure 12 shows the corresponding total generator power output at the various loads. The prediction is for a simple, constant internal resistance generator, namely

$$\text{Power} = V_{oc_{Ave}} \cdot I_{SC}\left[\frac{I}{I_{SC}} \quad 1 - \frac{I}{I_{SC}}\right] .$$

The average open circuit load potential, $V_{oc_{Ave}}$ and the total short circuit current, I_{SC} , are 165 volts and 42.8 amps, as obtained from Figure 11. It is noted that the above form of the equation for generator power is independent of the degree of electrode segmentation.

Figure 13 presents typical gas pressure data at open circuit and short circuit.

A few measurements of end effects were made by short-circuiting all interior electrodes and successively open-circuiting the exterior electrodes. The results showed a significant increase in load current for the two end electrodes of the interior set. The number of interior electrodes which were affected increased as the operating length of the generator was reduced. For example, with circuits #1 through #4 and #10 through #13 open-circuited, the active generator consisted of circuits #5 through #9 operating in the short-circuit condition. For this case the current through circuit #5 (upstream end) was 30% higher than when all 13 circuits were shorted; the corresponding increase for circuit #7 (center) was 11% and for circuit #9 (downstream end) was 16%.

Several measurements of generator internal leakage resistances were made during the 6-1/2 minute interval of

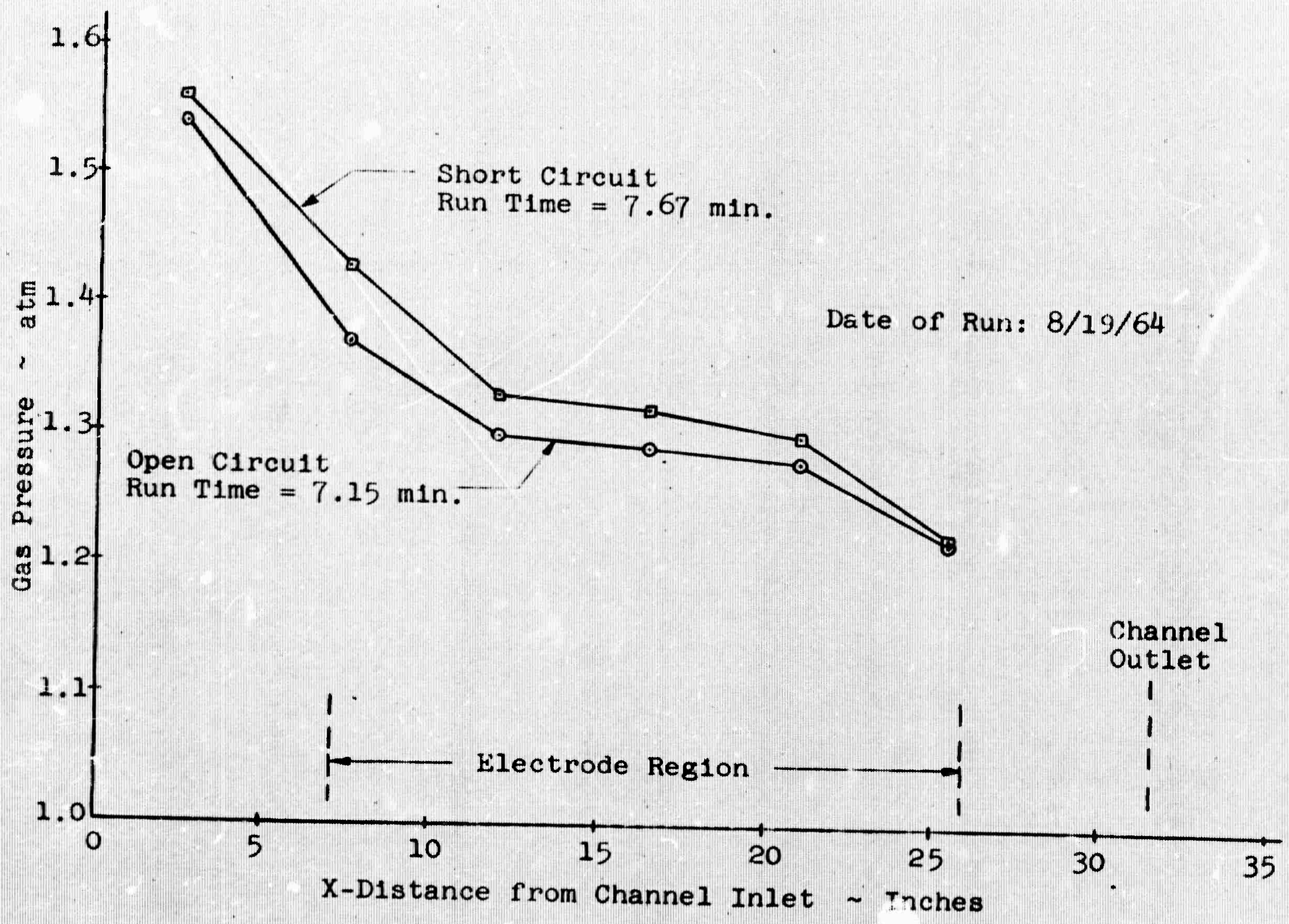

FIGURE 13 Combustion-Gas Pressure X-Distribution

operation with unseeded fuel. Qualitative measurements were made of resistance from electrode to ground, between adjacent electrodes, and between opposing electrodes. Indicated resistance varied from 50 ohm to 600 ohm. All measurements were made in the vicinity of the electrodes in circuit #7. Although the measurements should not be used quantitatively, they indicate leakage resistances of the same order of magnitude as the overall generator resistance and the gas resistance. Slopes of the loading characteristics curves such as in Figures 9, 10, and 11 indicate an overall generator average resistance of approximately 50 ohm per circuit.

The potential between test section and diffuser was measured at several times during the run. In all cases, no potential was measured. Much of the ceramic coating was removed from the diffuser wall during the run. This apparently had relatively little effect on the generator performance because the expected Hall field seemed to be developed in the downstream electrode region.

Very limited data were obtained with the electrodes, connected for continuous electrode operation. Automatic shutdown occurred soon after the electrical connections were made. However, the open-circuit data clearly show the effect of the internal Hall current. The data also indicate a low resistance path to ground in the vicinity of electrode #10; this is consistent with low load-current in circuit #10 (see Figure 6).

The next run in the power generation program will concentrate on the leakage resistance problem. High density low porosity Al_2O_3 will be used in several locations in order to reduce absorption of conductive materials by the brick. Various joints will be tried. The electrodes from the last run will be re-used with the threaded joint between head and shank replaced by a brazed joint.

2) Heat Transfer and Fluid Friction - Three problems are being considered in the area of heat transfer. The first is concerned with the insulator boundary layer in an MGD channel and the second treats the electrode boundary layer. These analyses take into account details of the MGD interaction and in their early stages ignore affects such as compressibility or chemical reaction. A third study is being made of the heat reansfer to a cooled electrode or heat transfer measuring calorimeter and is principally concerned with compressibility and effects due to large temperature differences between the gas and wall.

The preceeding progress report gave a detailed discussion of this research and this work has continued actively during the present quarter. The new results from these investigations, however, are incomplete and a detailed account will be given in the following Quarterly Report.

3) Physics

a) Calculation of Transport Properties in Seeded Combustion Gases - In 1961, Frost[1], proposed calculating the electrical conductivity of a partially ionized gas using Allis'[2] equation, valid for a Lorentzian gas. Frost replaced the electron-neutral collision frequency in Allis' formula with the sum of the electron-neutral and electron-ion collision frequencies. To take into account electron-electron interactions, Frost modified the expression for the electron-ion collision frequency so as to obtain the Spitzer-Harm value of the conductivity in the limiting case of a fully ionized gas.

In order to examine the validity of Frost's procedure, we have determined the electrical conductivity of a partially ionized gas taking into account rigorously e-e and e-i collisions by a modification of the Chapman-Enskog expansion scheme.

For the simple model of electron-neutral collision frequency

$$\nu_{en} = A_m \left(\frac{m_e g^2}{2e}\right)^m \quad , \qquad (1)$$

and the classical electron-electron and electron-ion cross-sections, the first three approximations to the electrical conductivity have been derived for an arbitrary degree of ionization. All three approximations agree, with the known corresponding approximations in the two limits of either a Lorentzian or a fully ionized gas.

In determinant form the third approximation may be written as:

$$\frac{\sigma(3)}{\sigma_{Add}} = \frac{3\pi(1+x)}{32\cdot 0.582} \cdot \frac{\begin{vmatrix} \beta_m + 2.072x & \delta_m + 3.582x \\ \delta_m + 3.582x & \lambda_m + 10.742x \end{vmatrix}}{\begin{vmatrix} \gamma_m + x & \alpha_m + x & \epsilon_m + \frac{15}{8}x \\ \alpha_m + x & \beta_m + 2.072x & \delta_m + 3.582\,x \\ \epsilon_m + \frac{15}{8}x & \delta_m + 3.582x & \lambda_m + 10.742x \end{vmatrix}} \qquad (2)$$

where

$$\frac{1}{\sigma_{add}} = \frac{1}{\sigma_{en}} + \frac{1}{\sigma_{ei}} \quad ,$$

$$x = \frac{\sigma_{en}}{\sigma_{ei}} \propto \text{degree of ionization} \quad .$$

The quantities σ_{en} and σ_{ei} are the exact conductivities of the Lorentzian gas and the fully ionized gas respectively. The remaining quantities depend on the assumed power law of the collision frequency, and are given by

$$\gamma_m = \frac{\Gamma(5/2 - m)\ \Gamma(5/2 + m)}{6 \times 0.582}$$

$$\epsilon_m = \frac{1}{2}(m^2 - m)\gamma_m \qquad \alpha_m = -\frac{2}{3}\, m\, \gamma_m$$

$$\delta_m = -\frac{1}{3}(m^3 + m^2 + 5m)\gamma_m \qquad \beta_m = \frac{2}{g}(2m^2 + 2m + 5)\gamma_m$$

$$\gamma_m = \frac{1}{4}(m^4 + 2m^3 + 13m^2 + 12m + \frac{35}{2})$$

Figures 14 to 17 show the dependence on degree of ionization of the first three approximations to the electrical conductivity. These curves give a clear idea of the rate of convergence of the first three approximations for different models of the electron-neutral cross-section. For high values of ionization, electronic interactions dominate. The conductivity is insensitive to the parameter m and rapidly approaches the value of the corresponding fully ionized case. The behavior at low levels of ionization is different however. As shown by the detailed study of the Lorentzian gas in the last progress report[3], the speed of convergence is highly sensitive to the dependence of cross-section on electron velocity. For $m = -1$ and for $m = 0$ (Maxwellian molecules) convergence is excellent and the third approximation seems to be sufficient for all levels of ionization. For $m = 1/2$ (hard spheres) and for $m = 1$, convergence for low values of ionization is less rapid. While the third approximation, for these two models, is certainly satisfactory at high levels of ionizations, it is not very good at low ionization levels.

At low values of ionization Frost's results seem to be more satisfactory, as expected, since his formulation is rigorous for low ionization and corresponds, in the limit, to the "infinite" Chapman-Enskog approximation, $\sigma(\infty)$.

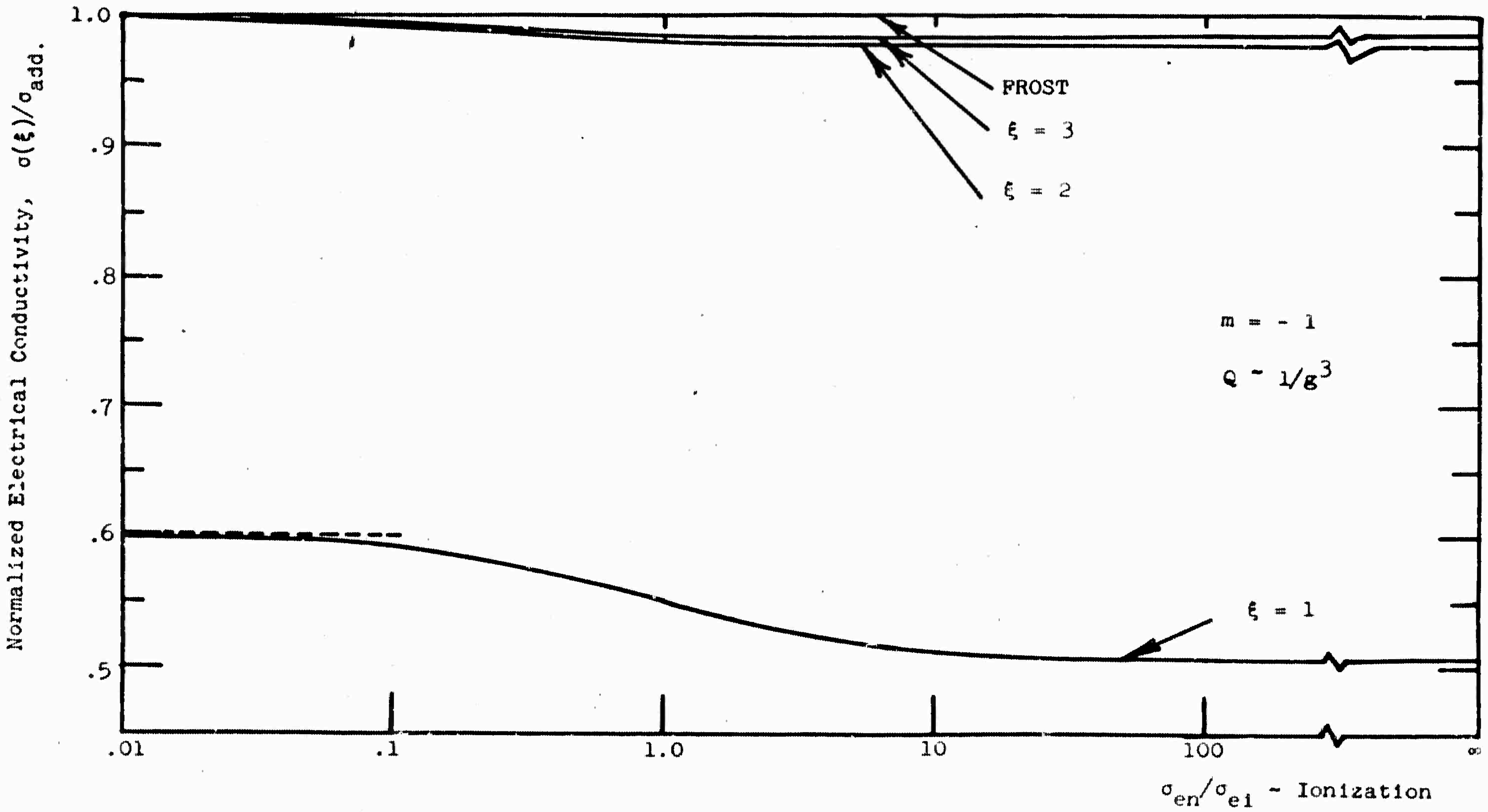

FIGURE 14 Normalized Conductivity of First Three Chapman-Enskog Approximations and of Frost as a Function of Ionization.

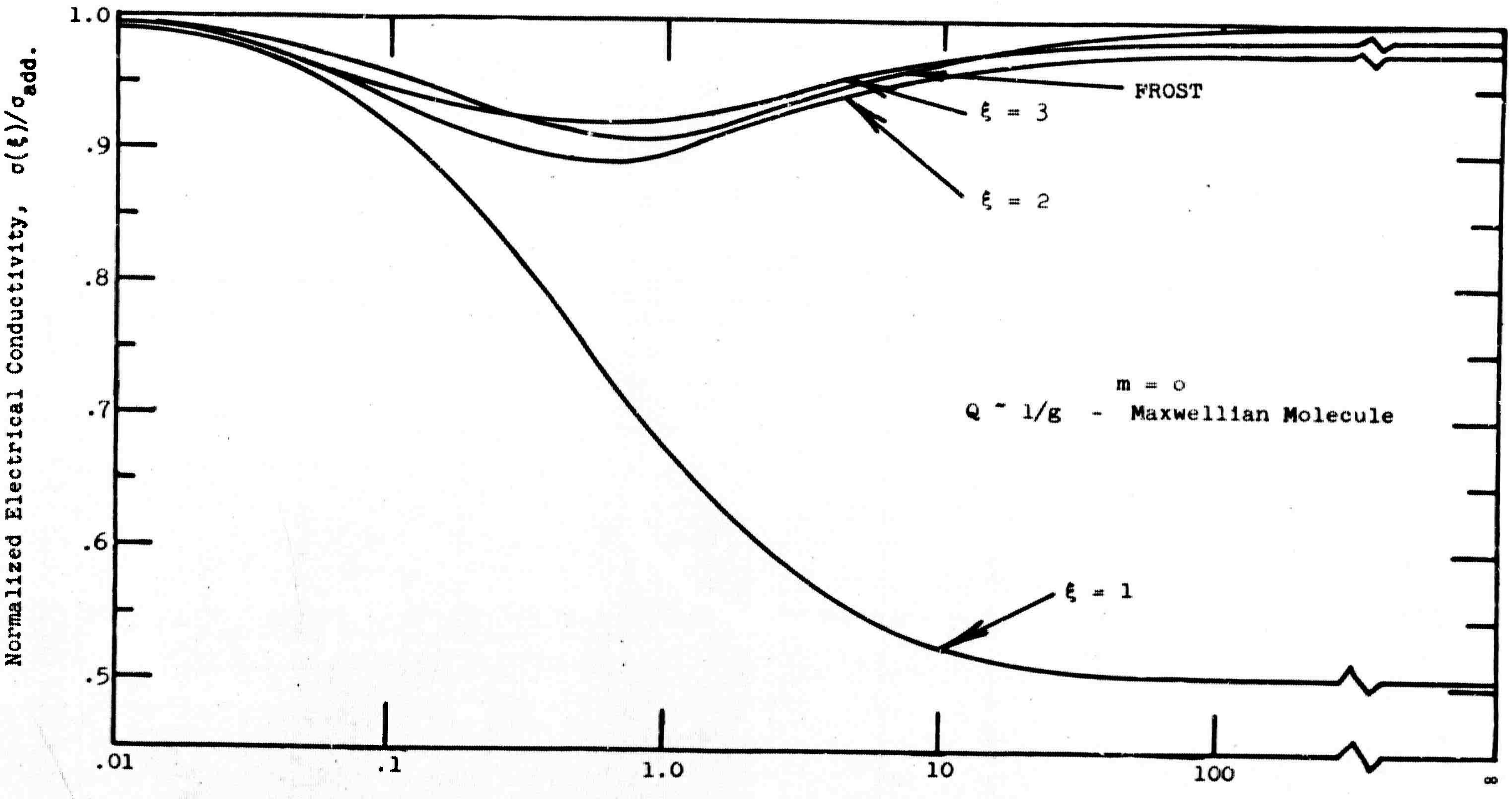

FIGURE 15 Normalized Conductivity of First Three Chapman-Enskog Approximations and of Frost as a Function of Ionization.

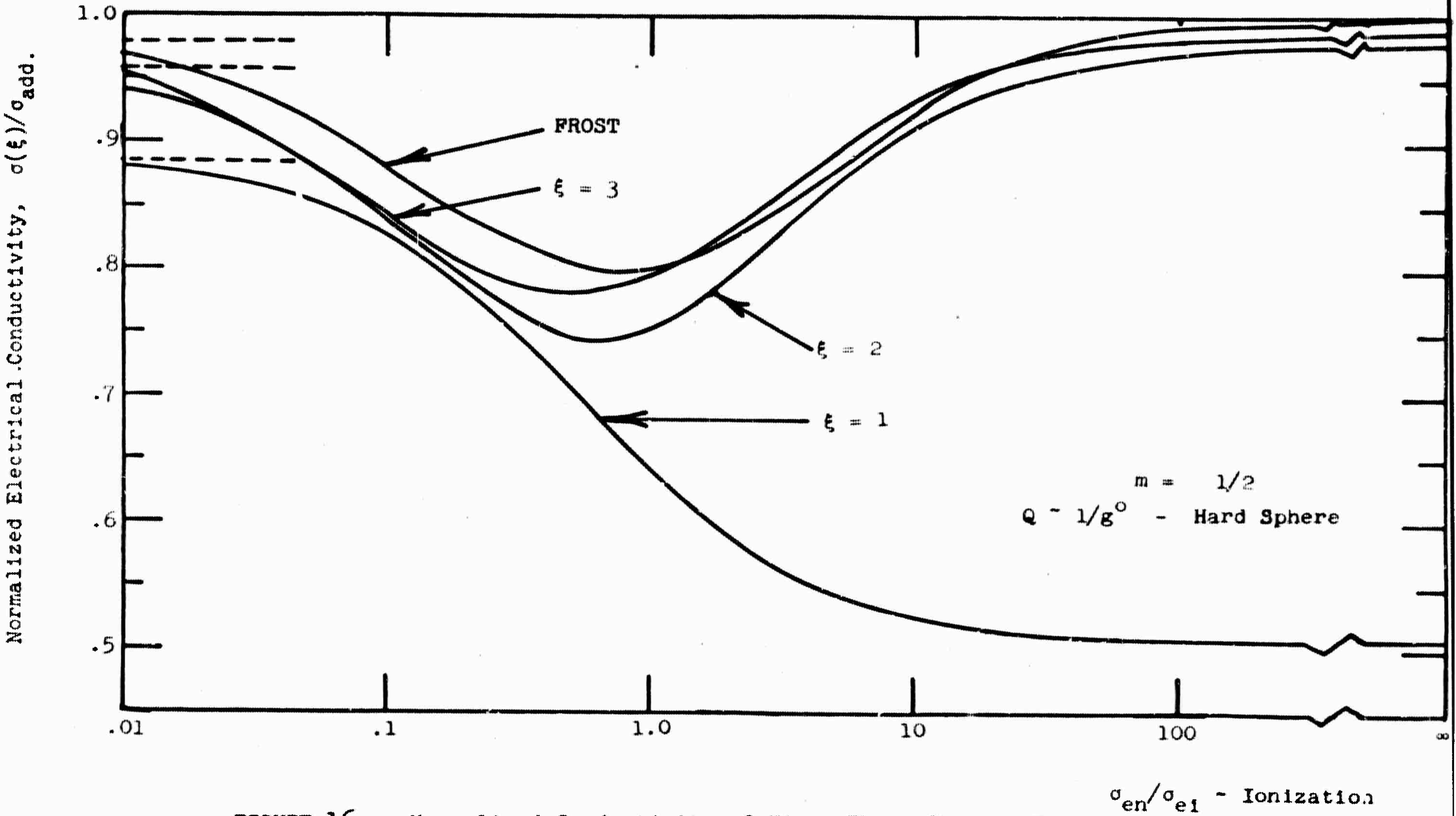

FIGURE 16 Normalized Conductivity of First Three Chapman-Enskog Approximations and of Frost as a Function of Ionization.

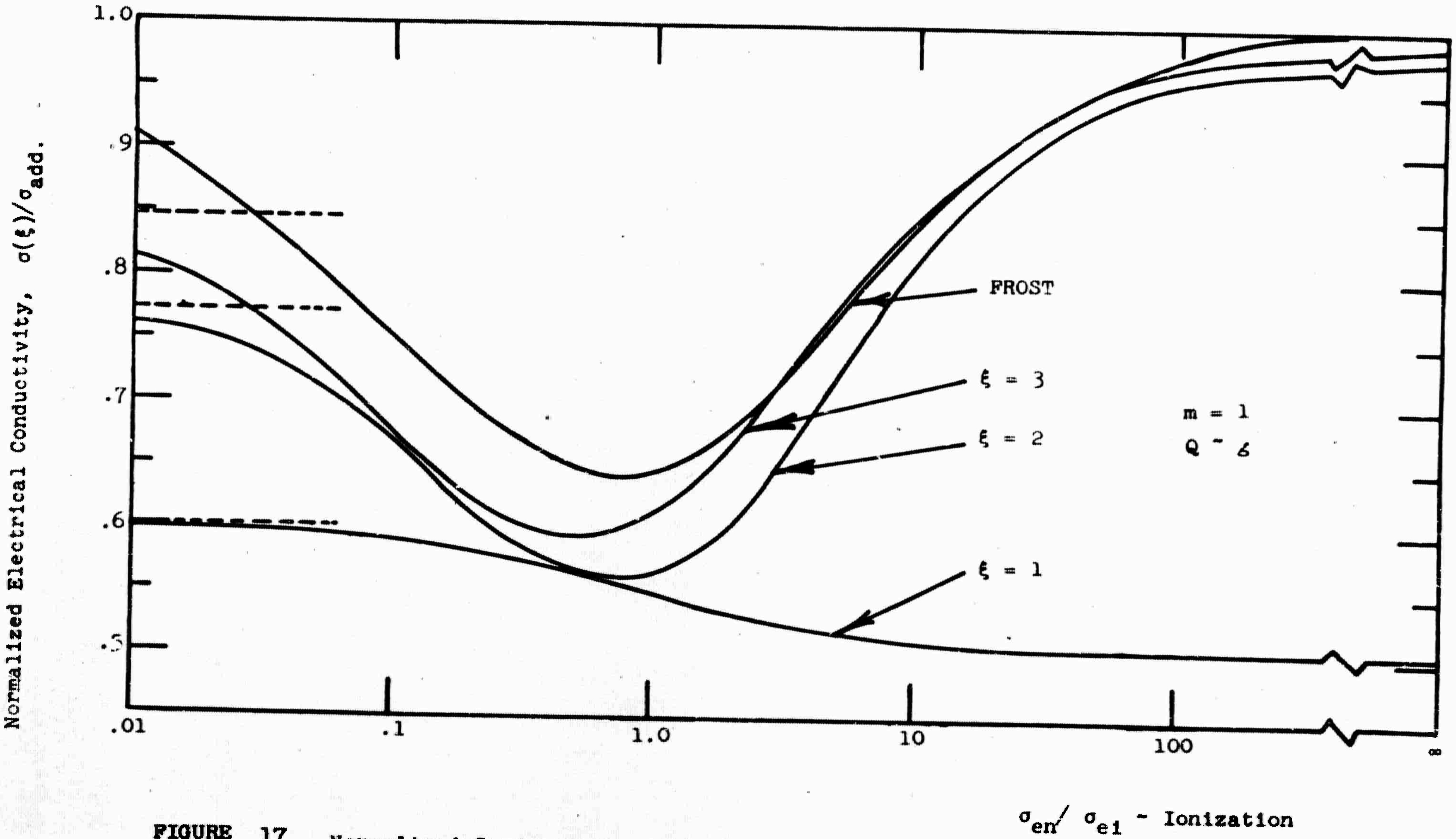

FIGURE 17 Normalized Conductivity of First Three Chapman-Enskog Approximations and of Frost as a Function of Ionization

For high values of ionization, Frost's results agree well with the third Chapman-Enskog approximation which includes the electron-electron interaction rigorously. Since Frost has used a fitting technique to make his results agree with the values of the fully ionized conductivity, his results for infinite degree of ionization are, as expected, slightly (less than 2%) better than the third approximation.

In conclusion, we believe that this study provides thoretical justification for the use of Frost's method in calculating the electrical conductivity of a partially ionized gas in the absence of a magnetic field.

A second related problem was investigated - that of the effect of small $\ln \Lambda$. The kinetic theory description of collisions between charged particles has, until recently[4], required some sort of ad hoc cut-off procedure in order to prevent the occurrence of divergent integrals. The source of this difficulty stems from the long-range nature of the Coulomb interaction and the treatment of all collisions as two-body encounters. In actuality, the interaction potential is essentially shielded by the collective behavior of the particles at sufficiently large distances. A convergent theory is obtained by introducing some device for ignoring collisions with large impact parameters in excess of the Debye length. The resulting theory is valid to order $(\ln \Lambda)^{-1}$, where $\Lambda = 1.24 \times 10^4 (T^3/n)^{1/2}$ is the ratio of the Debye length to the impact parameter for a 90° deflection. (The quantities T and n denote the temperature in °K and the number density per cm^3 respectively). In particular, the widely-quoted value of Spitzer and Harm for the electrical conductivity of a fully-ionized plasma is correct to this order.

In the following table, we have calculated the values of Λ and $\ln \Lambda$ for a range of temperatures and number densities which encompass conditions expected in MHD generators. Typical values of $\ln \Lambda$ are seen to range between 4 and 5 which implies an uncertainty of about 25% in the Spitzer-Harm conductivity.

Values of Λ and ($\ln \Lambda$)

n_e (cm^{-3})

T_e (°K)	10^{12}	10^{13}	10^{14}	10^{15}	10^{16}
1000	392 (5.97)	124 (4.82)	39.2 (3.67)	12.4 (2.52)	3.92 (1.37)
1500	721 (6.58)	224 (5.41)	72.1 (4.28)	22.4 (3.11)	7.21 (1.98)
2000	1110 (7.01)	351 (5.86)	111 (4.71)	35.1 (3.56)	11.1 (2.40)
2500	1550 (7.35)	491 (6.20)	155 (5.04)	49.1 (3.89)	15.5 (2.74)
3000	2040 (7.62)	645 (6.47)	204 (5.32)	64.5 (4.17)	20.4 (3.02)

The region to the left of the heavy line in this table indicates roughly conditions for which this theory is sufficiently accurate (uncertainty less than 20%).

In about 1960, Lenard, Balescu, Rostoker and Rosenbluth as well as others, obtained a kinetic equation which automatically took into account the collective behavior of a plasma, and converged for large impact parameters. However, this so-called "fluid-approximation" diverged for small impact parameters, and so it was necessary to introduce an ad-hoc small cut-off limit.

The most recent important progress in the kinetic-theory of charged particles was made in 1963 by Kihara and Aono[4]. These authors proposed a "unified theory" for combining both the close and distant encounter contributions to the kinetic description of collisions, in such a way as to yield a divergenceless theory without the need of ad-hoc assumptions. The validity of this new theory is of order Λ^{-1}, and thus provides ample accuracy for MHD generator applications. The region to the left of the double-line in the preceding table indicates conditions for which this new theory is sufficiently accurate (uncertainty 10% or less).

The theory of Kihara and Aono has been applied by Ikitawa[5] to the calculation of the electrical conductivity of a fully-ionized plasma. The method of calculation is similar to that of Chapman-Enskog, and involves an expansion in terms of Sonine polynomials. In Figure 18 we have plotted the ratio of Ikitawa's second approximation to the Spitzer-Harm value of the electrical conductivity, as a function of $\ell n\ \Lambda$. For values of $\ell n\ \Lambda \approx 4$, the more accurate value of the electrical conductivity is about 30% higher than the Spitzer-Harm value.

In 1964, Rynn[6] reported a measurement of the electrical conductivity in a fully-ionized plasma which was 20% higher than the Spitzer-Harm theoretical value. The probable error or Rynn's measurement was stated to be ± 10%. At the value of $\ell n = 7$ for which Rynn's experiment was performed, Ikitawa's value of conductivity is about 10% larger than the Spitzer-Harm value, which places Ikitawa's theoretical value within the probable error of the experiment. This comparison with experiment appears to provide some support for the new theory.

Under MHD generator conditions, the plasma is only partially ionized, and so the magnitude of the correction discussed above will be proportionately smaller. When the charged particle encounters are equally important to electron-neutral collisions, we may expect a correction of the order of 15%, and so we plan to incorporate the results of this new theory into our calculations.

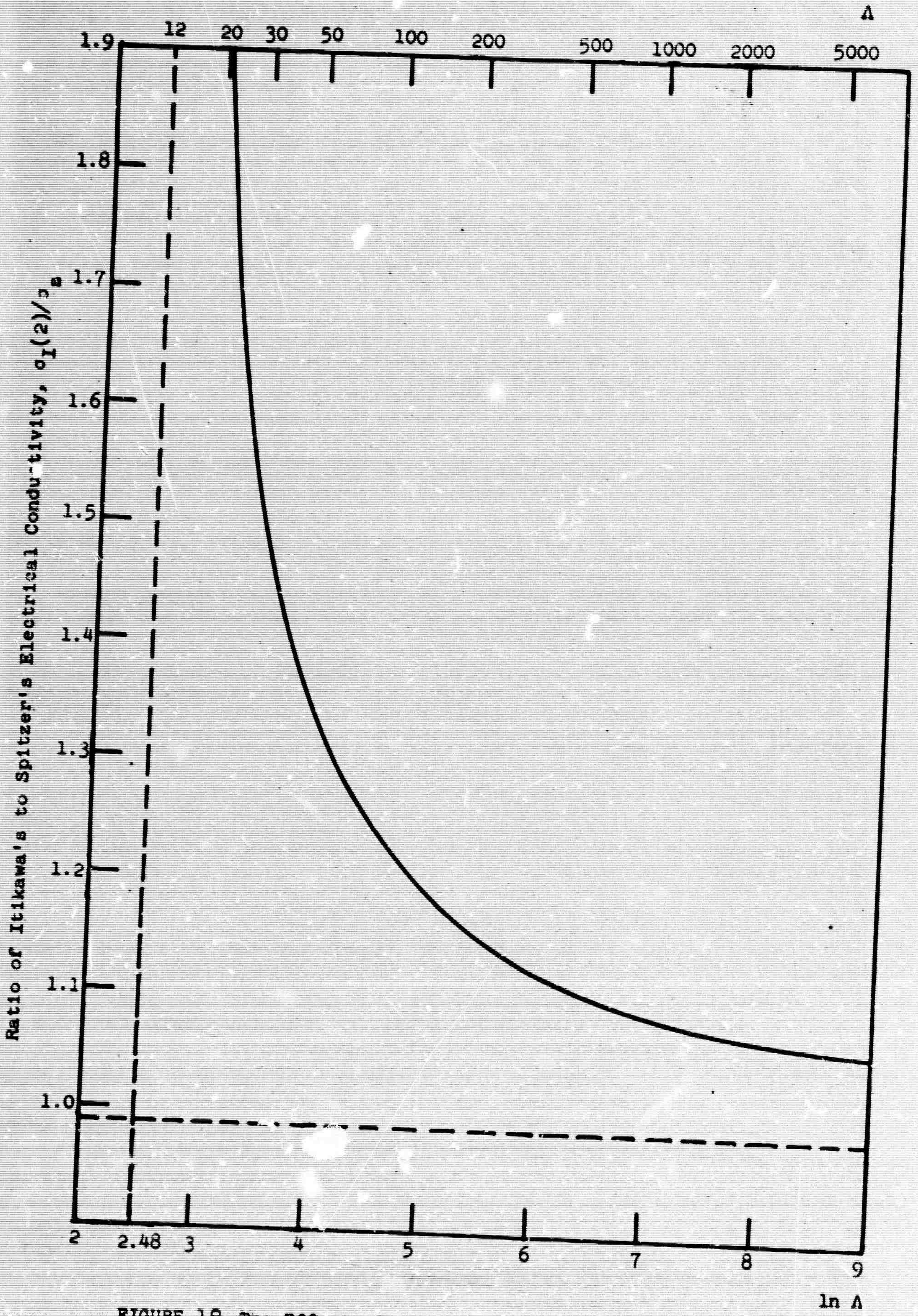

FIGURE 18 The Effect of ln Λ on the Second Approximation to Itikawa's Electrical Conductivity.

b) The Influence of the Ramsauer Effect on Nonequilibrium Electron Temperatures - The following is a Research Note submitted for publication in the Physics of Fluids. We note that recent calculations by Zukoski, Cool, and Gibson (AIAA Journal 2, 1410) confirm the important influence of the Ramsauer cross-section.

Kerrebrock and others[7,8,9] have considered recently the effect of elevated nonequilibrium electron temperatures on the electrical conductivity of partially-ionized seeded noble-gas plasmas. The departure of the electron temperature from the gas temperature has been estimated by means of a balance between the energy gained by the electrons as they drift through the electric field and the energy lost in collisions with the heavy particles. Constant collision cross-sections have been used in these calculations and in the calculation of the electrical conductivity. The electron number density has been found by means of the Saha equation evaluated at the electron temperature and this has been justified by the assumption of a Maxwellian distribution of electron energies. In the present analysis a displaced-Maxwellian electron distribution function is used to assess the importance of the variation of the collision cross-section with electron energy. In particular, for elastic collisions between electrons and noble-gas atoms the pronounced minimum in the cross-section at electron energies of the order of one electron volt (the Ramsauer effect) is shown to have a significant effect upon the variation of the collision frequency with electron temperature.

We adopt a coordinate system for which the mean velocity of the heavy particles is zero and assume a Maxwellian heavy-particle distribution function at the known temperature T_h. The electron distribution function is taken to be Maxellian about the electron drift velocity c_e with an electron temperature T_e. The unknown parameters c_e and T_e are found by means of the momentum and energy moments of the electron Boltzmann equation with only the electric-field term retained on the left-hand side.

With the displaced-Maxwellian distribution our collision integrals are identical to those considered by Morse[10]. For small values of the parameter $m_e c_e^2/(2k\,T_e)$ and with the definitions $j \equiv -em_e c_e$ and $\sigma \equiv j/E$, the results can be put in a form that is similar to familiar phenomenological relations. We then have

$$\frac{1}{\sigma} = \frac{m_e}{e^2 n_e} \frac{4}{3} \sqrt{\frac{8kT_e}{\pi m_e}} \sum_h n_h \bar{Q}_{e,h}(T_e) \qquad (3)$$

and

$$\frac{j^2}{\sigma} = n_e\, 3k(T_e - T_h) \frac{4}{3} \sqrt{\frac{8kT_e}{\pi m_e}} \sum_h \frac{m_e}{m_h} n_h \bar{Q}_{e,h}(T_e) , \qquad (4)$$

where the effective mean cross-section $\bar{Q}_{e,h}(T_e)$ is defined in terms of the differential cross-section $I_{e,h}(g,\chi)$ by

$$\bar{Q}_{e,h}(T_e) \equiv \left(\frac{m_e}{2kT_e}\right)^3 \int_0^\infty e^{-m_e g^2/2kT_e} g^5\, 2\pi \int_0^\pi (1-\cos\chi) I_{e,h}(g,\chi) \sin\chi\, d\chi\, dg . \qquad (5)$$

$\bar{Q}_{e,h}(T_e)$ differs by only a factor from the integral $\Omega_{12}^{(1)}$ (1) that enters the Chapman-Enskog theory. The summation is performed over all species of heavy particles (neutrals and ions). If the masses of all heavy particles are equal, Eqs. (3) and (4) give

$$\frac{m_e j^2}{e^2 n_e^2\, 3K(T_e - T_h)} = \frac{m_e}{m_h} . \qquad (6)$$

The effective cross-section $\bar{Q}_{e,h}(T_e)$ was evaluated for several noble gases, potassium, and cesium by numerical integration over the relative velocity g. Collision probability data were taken from Brown[11] and Massey and Burhop[12] and the references cited therein. From estimates based on the available data for the angular dependence of the differential cross-section, the momentum-transfer cross-section $2\pi \int_0^\pi (1-\cos\chi) I_{e,h}(g,\chi)\sin\chi d\chi$ in Eq. (5) was approximated by the measured total cross-section $2\pi \int_0^\pi I_{e,h}(g,\chi)\sin\chi d\chi$. Our calculations indicate that the effect of uncertainties in the very-low-energy cross-section is small for $T_e>2000°K$; this results from the factor g^5 in Eq. (5). The calculated values of $\bar{Q}_{e,h}(T_e)$ are given in Figure 19. For gases that exhibit a pronounced Ramsauer effect the effective cross-section $\bar{Q}_{e,h}$ varies by as much as a factor of 8(argon) in the range of electron temperatures shown. These values of $\bar{Q}_{e,h}$ are significantly greater than the total cross-section at the Ramsauer minimum. The effective electron-ion cross-section, calculated from Eq. (5) with the Rutherford cross-section and the Debye cutoff, is

$$\bar{Q}_{e,i}(T_e) = \frac{\pi e^4}{2(kT_e)^2} \ln \Lambda \quad . \qquad (7)$$

With this displaced-Maxwellian cross-section the electron-ion resistivity (Eq. 3) is higher than the Spitzer-Harm resistivity by a factor of 1.98.

Calculations based on Eqs. 3, 4, 5 and 6 and the Saha equation evaluated at the electron temperature were compared with the measurements of Kerrebrock[8] and Zukoski[3]. These experiments were conducted with flowing, partially-ionized, potassium-seeded argon at atmospheric pressure with an applied electric field. The comparisons, shown in Figures 20 and 21, are favorable in view of the fact that no corrections to the theory or empirical information, other than measured cross

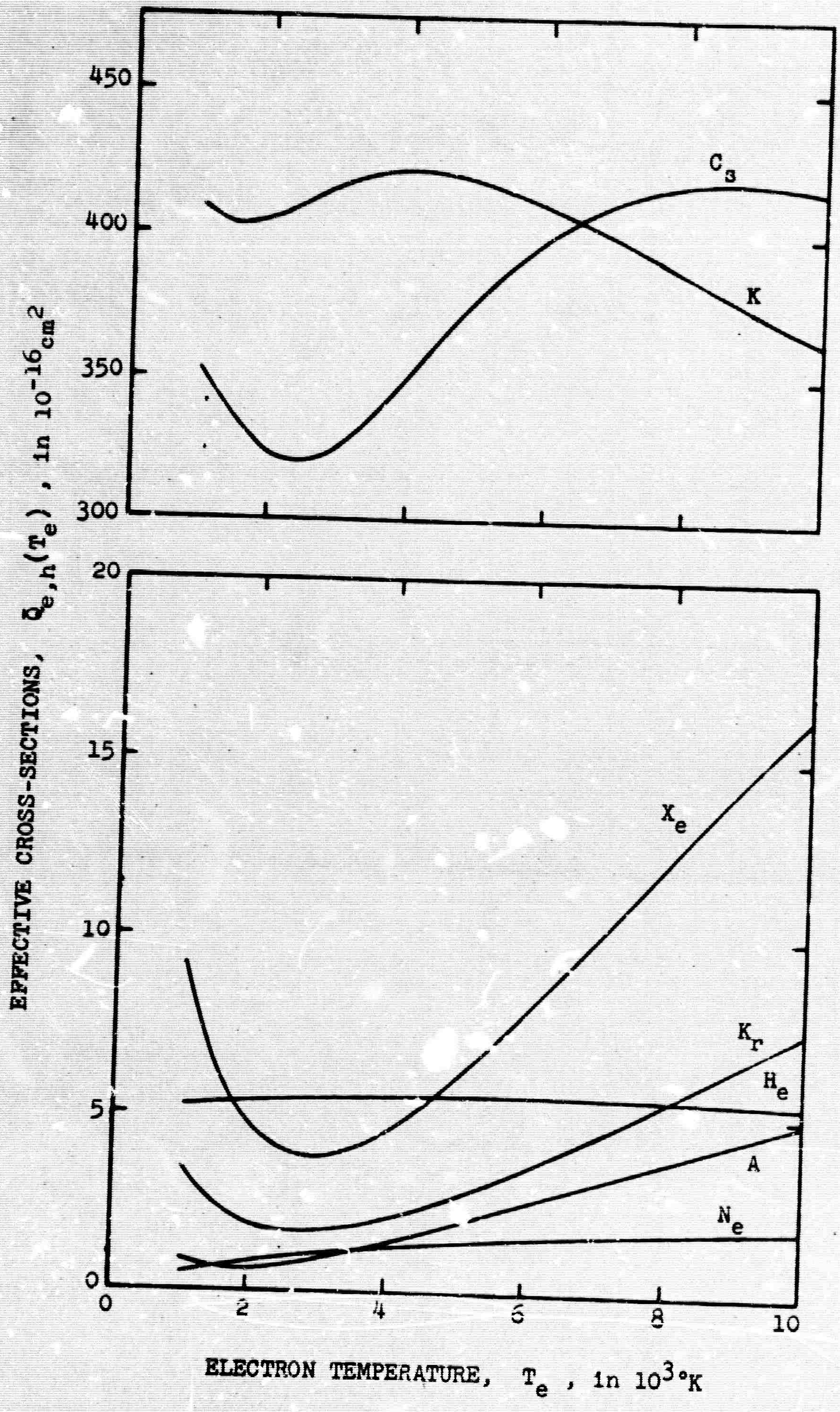

FIGURE 19 Calculated effective cross-sections as a function of electron temperature.

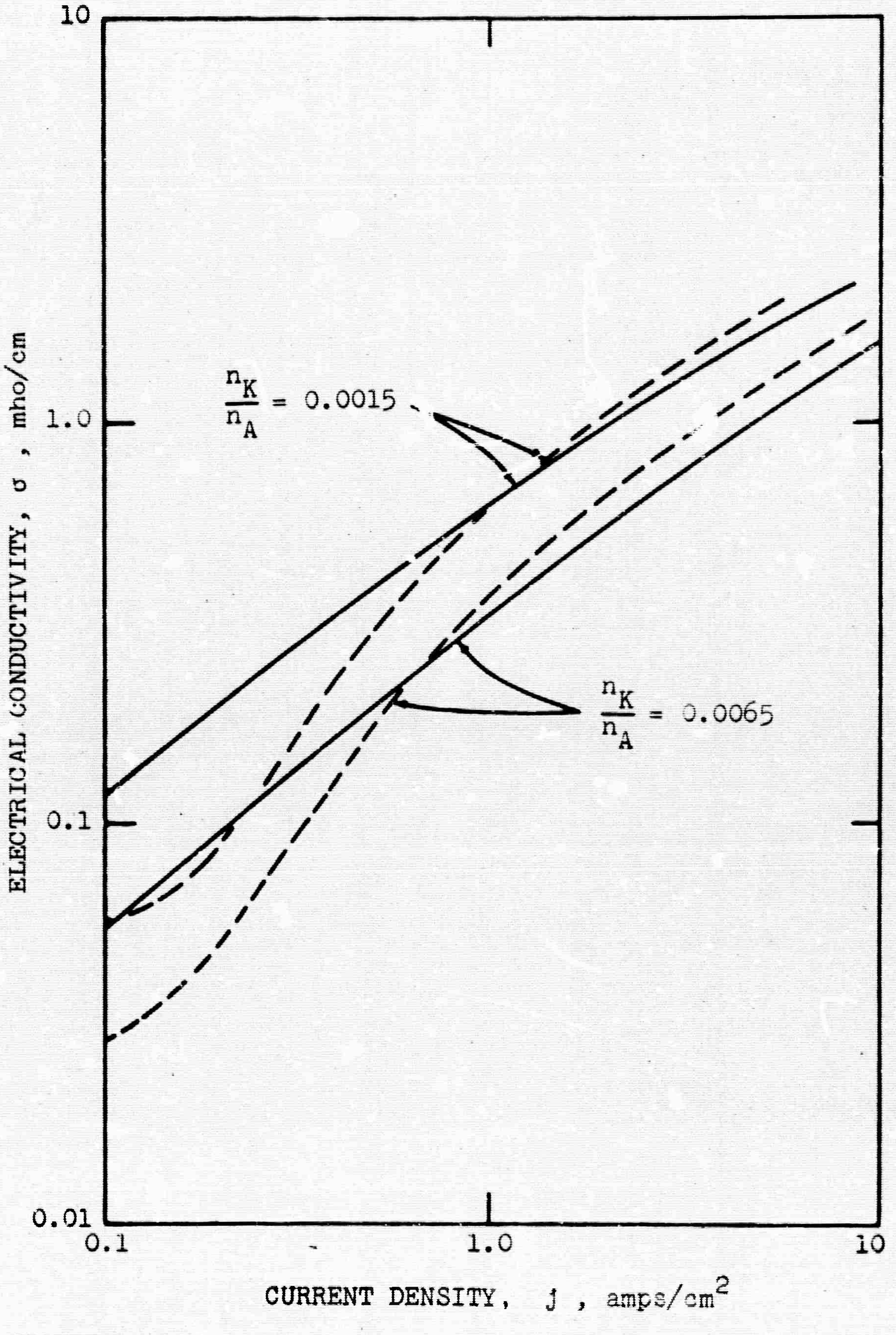

FIGURE 20 Comparison of the present theory (———) with the experiments (------) of Kerrebrock[2]. $T_h \approx 2000$°K.

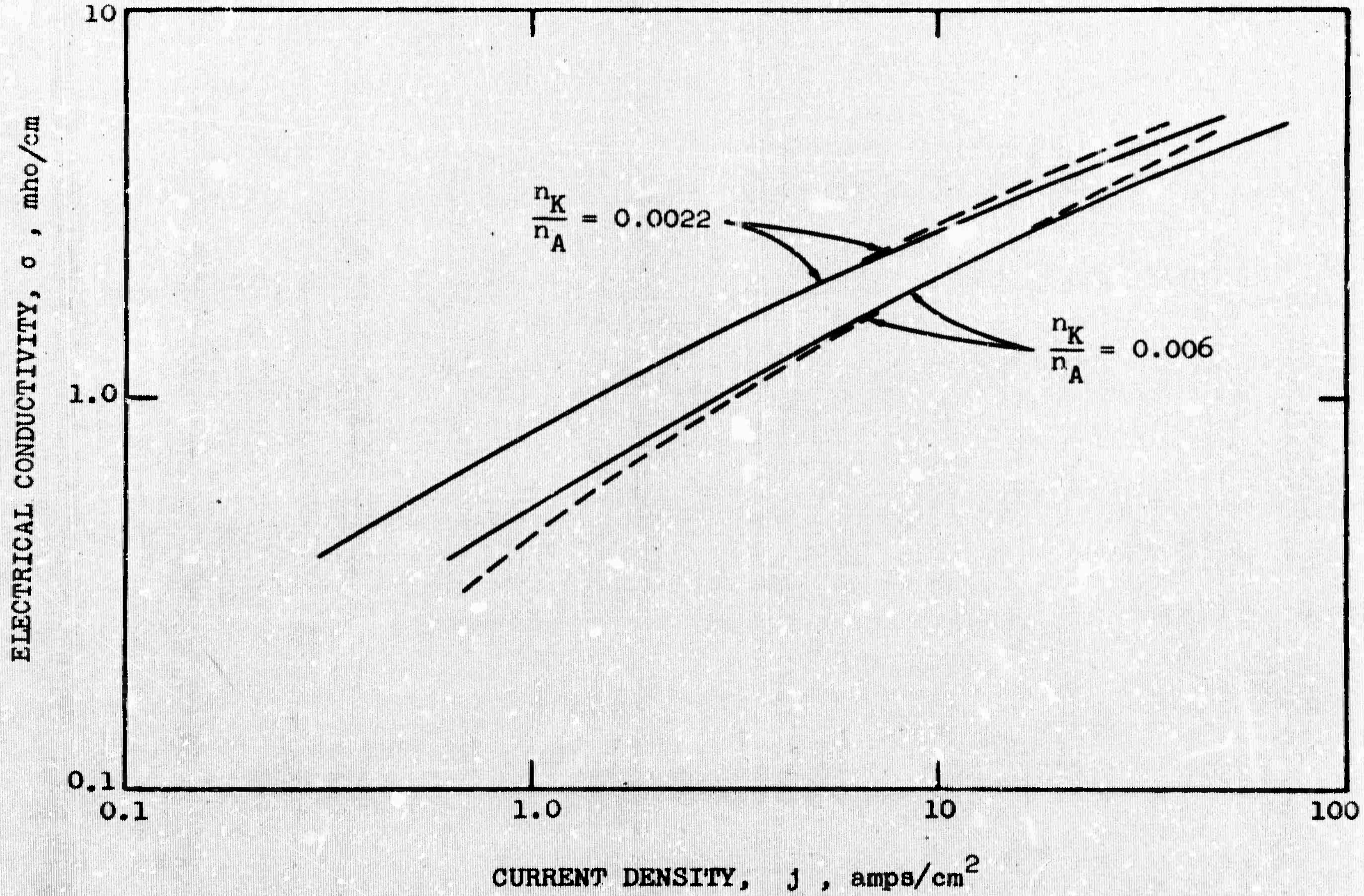

FIGURE 21 Comparison of the present theory (———) with the experiments (------) of Zukoski^3. $T_h \approx 2000°K$.

sections, were used*. Calculations made in reference 8 and 9 with the constant cross-sections $Q_A = 0.7 \times 10^{-16}$ cm^2 and $Q_K = 250 \times 10^{-16}$ cm^2 lie significantly above the data. Although our results indicate the importance of the variation of the differential cross-section with electron energy on nonequilibrium electron temperatures and tend to support the use of a displaced-Maxwellian distribution, the situation will not be fully understood until the electron distribution function can be accurately predicted. Such an investigation is currently in progress.

4) Diagnostics - A sodium line reversal apparatus has been developed in conjunction with the Stanford MGD generator channel to provide a check on the calculated temperature and to measure directly the electron temperature in the presence of induced currents. A description of the method and its application to the Stanford channel is given in detail in Appendix A of this report.

A light source which is a calibrated tungsten ribbon lamp is used in conjunction with an optical system and a Jarrell-Ash half meter Ebert scanning spectrometer. Experimental results obtained with the present apparatus have been performed on small propane-air torch arrangements, with small amounts of sodium added to the flame by means of a ceramic rod coated with NaD inserted into the base of the flame. In this phase of development the temperature of the flame has been determined to an observable experimental accuracy of 10°K. By this it is meant that two different output spectral line shapes corresponding to a difference of 10°K in flame temperature are easily distinguished and accurately measured. Figures A-2, A-3, A-4, and A-5 in Appendix A-1 are

---

*The fact that losses by radiation and the effects of inelastic collisions were not included in the analysis must be considered, however, in the interpretation of these comparisons.

typical examples of the NaD lines as seen in the small propane flame.

Attempts were made to obtain line reversal with a potassium seeded small propane flame for the potassium lines at 4042 and 4044 Å . The signal received from these lines was very weak due to the small amounts of potassium added which the physical size of the flame dictated. Emission lines were obtained, but the reversal condition signal was immeasurable.

At the present time testing is underway to determine flame temperature for various constituent percentages in the MHD generator. The temperatures are obtained at the plenum chamber exit, exhausting to the atmosphere. The preliminary results from this testing show that the percentage of sodium in the flame should be in the order of 1/100 percent or less to avoid self absorption in the emission lines. Reversal conditions have been observed for several constituent percentages at low flow rates.

B. Shock Tube

The following paragraphs constitute a brief summary of the shock tube phase of the MHD energy conversion program.

The function of the shock tube work has been to perform quantitative experiments with shock-heated plasmas which would augment our understanding of their physical properties and dynamic behavior. The tube used here was designed to cover and extend somewhat the range of parameters having importance for the performance of MHD power generation equipment. Details of the design have been given in previous reports of this series. Performance of the device has been in close accord with its design, and has, in general, been very satisfactory. It remains the most quantitative device available for producing a well-defined sample of plasma having precise physical and dynamic characteristics in the temperature and density range of interest to this project.

The major initial effort in the program concerned the abovementioned shock-tube design, acquisition and fabrication of components, shakedown tests of subsystems, and a series of calibration shots. Initial operation took place in mid-fall 1962 according to schedule, and the facility has seen regular use since that time in a series of research investigations. By now, the following results have been accomplished:

(1) Calibration of shock tube performance over a wide range of operating conditions;

(2) Evaluation of the overall precision and limitations on the use of optical interferometry to measure electron density in the dense plasma range, $10^{15} - 10^{18}$/cc ;

(3) Measurement of the thermal equilibration of a shock-heated plasma;

(4) Calculation of the high temperature transport properties of monatomic gases, using the higher approximations of the Chapman-Enskog formalism.

In addition, a series of systematic investigations is now under way in the following areas:

(5) Recombination processes in a flowing plasma cooled by a stationary expansion wave;

(6) Radiative thermal transport.

Details of portions of the above studies have been given in earlier reports in this series. In particular, items (2) and (3) were treated in Supplement 2 to the Quarterly Report 1 March – 31 May 1964 (see listing below). In particular, this work did verify the high precision of optical interferometry for measuring the electron density of dense plasmas. It also verified the atomic collision model leading to thermal ionization, with indication of the order of magnitude of atom-atom collision cross sections. The work also yielded results for the electron temperature variation in the non-equilibrium regime, and showed at what stage of the equilibration process recombination events become important. The variation of the electron density downstream of the equilibration point gives further quantitative data on the radiation cooling rate in an otherwise uniform plasma.

The work just described also provided implicit verification of the Saha equation, in that the measured equilibrium value of electron density was in good agreement with that predicted by a combination of the Rankine-Hugoniot and Saha relations applied to the measured shock velocity and shock tube conditions. This result was further verified by an additional independent series of experiments which formed the basis of another student's Engineer's Thesis (see listing below).

The analysis of high temperature transport properties of a partially ionized monatomic gas, item (4) above, has helped to resolve the disagreement which develops when partially-ionized conductivity expressions are extended, in the limit, to full ionization – the trouble being that these do not agree with results calculated explicitly for a fully ionized plasma. The present work has shown that satisfactory agreement can be obtained if one goes to the third approximation in the Chapman-Enskog theory. Expressions have been obtained to the fourth approximation in the thermal conductivity, thermal diffusion coefficient and ordinary diffusion coefficient. The viscosity is treated to the second approximation. It is noteworthy that thermal diffusion plays an important role in an ionized gas.

In connection with item (5) above, recent interferograms have shown the need for obtaining greater fringe shifts, since it is desired to measure the variation of fringe shift along a radial line of the Prandtl-Meyer expansion and along the streamline running close and parallel to the downstream wall. The total fringe shift plot given in the last quarterly progress report was for a wavelength of 4500Å . This has now been extended to wavelengths of 5890Å and 6900Å (corresponding to the radiation from a ruby laser). Since the major contribution to the fringe shift is from the free electrons, it turns out that the higher wavelengths yield greater fringe shifts (proportional to wavelength).

Turning to item (6), we remark only briefly that preliminary experiments have given clearly defined interference fringes in the shock layer of a cylinder immersed in a shock-heated flow of argon plasma. The masking effects of the intense shock layer radiation have been eliminated by use of a Kerr cell shutter on loan through the courtesy of the nearby Lockheed Research Laboratory. The optical experiments have been supplemented by a series of preliminary thick film heat transfer measurements along the stagnation line. The present work aims to measure both the convective and radiative heat transfer from the shock layer-boundary layer plasma, with independent measurement of the electron density as a control. As such it will represent an extension of the work of Rutowski and Bershader.*

For reference purposes, the following listing of output of the shock tube phase of the program is given:

Technical Supplements to Progress Reports:

H. Wong and D. Bershader, "Interferometric Study of Thermal Equilibration of a Shock Heated Plasma," Supplement 2, April 20, 1964.

R. S. deVoto, "Transport Properties of Partially Ionized Monatomic Gases," being issued as a supplement to this report.

---

*Rutowski, R. and Bershader, D., Physics of Fluids, 7, 568-577, 1964.

Technical Society Presentation:

H. Wong, "Interferometric Study of Shock-Induced Reaction Rates in Argon," AIAA Annual Meeting, Washington, D.C., July 1, 1964.

Journal Publications:

The work of both Wong and deVoto will appear as publications in an archive journal.

Graduate Thesis Programs:

Howard Wong, Ph.D. (awarded June 1964), "Interferometric Study of Thermal Equilibration of a Shock Heated Plasma."

R. S. deVoto, Ph.D. (to be completed January 1965), "Transport Properties of Partially Ionized Monatomic Gases."

The following thesis programs were independently supported but made use of the shock tube facility and dealt with the closely related subjects:

Charles Elliott, Engineer's Degree (completed August 1964), "Interferometric Study of the Shock Layer of a Cylinder Immersed in a Flowing Plasma."

William Y. Cole, Engineer's Degree (completed August 1964), "Measurement of Electron Density in a Shock-Heated Plasma and Comparison with the Saha Equation."

All in all, the program to date has been a fruitful one, and it will be continued as a long-range program emphasizing quantitative optical measurements of dense, shock-heated plasmas.

APPENDIX A

Spectral Line Reversal Method for Equilibrium Flows

I. Introduction

The sodium line reversal method of flame temperature measurement was introduced by Féry in 1903[13], its validity established by Kohn in 1914[14], and engineering measurements of combustion temperatures well underway in 1933[15]. Numerous references describe the basic theory and experimental design of the method, some of the best are references[16,17], and later by Mak[18]. The apparatus developed for the flame temperature measurements in the Stanford MHD generator is shown in Figure A-1. A tungsten filament lamp shines through the flame containing sodium atoms, whose temperature is to be measured, and then passes through the slit of the spectrometer. Adjustment of the lamp brightness temperature to the temperature of the flame will cause the NaD lines (3s-3p transition) to match with the lamp background. Precise determination of the calibrated lamp current will then yield the flame temperature after the appropriate corrections for brightness temperature, wavelength, and optical effects have been made.

For this method of temperature measurement to be valid there are several assumptions which must be made about the flame. The first is that the flame must be optically transparent in the wavelength region of interest (5890-5896 for NaD lines). This necessitates the use of small amounts of sodium in the flame. Secondly the flame must be in thermodynamic equilibrium if flame temperatures are to be measured. Other assumptions are listed as they occur.

II. Sodium Line Reversal Method: Theory

a. Basic Equations and Nomenclature*

---

*General reference for this section is 18.

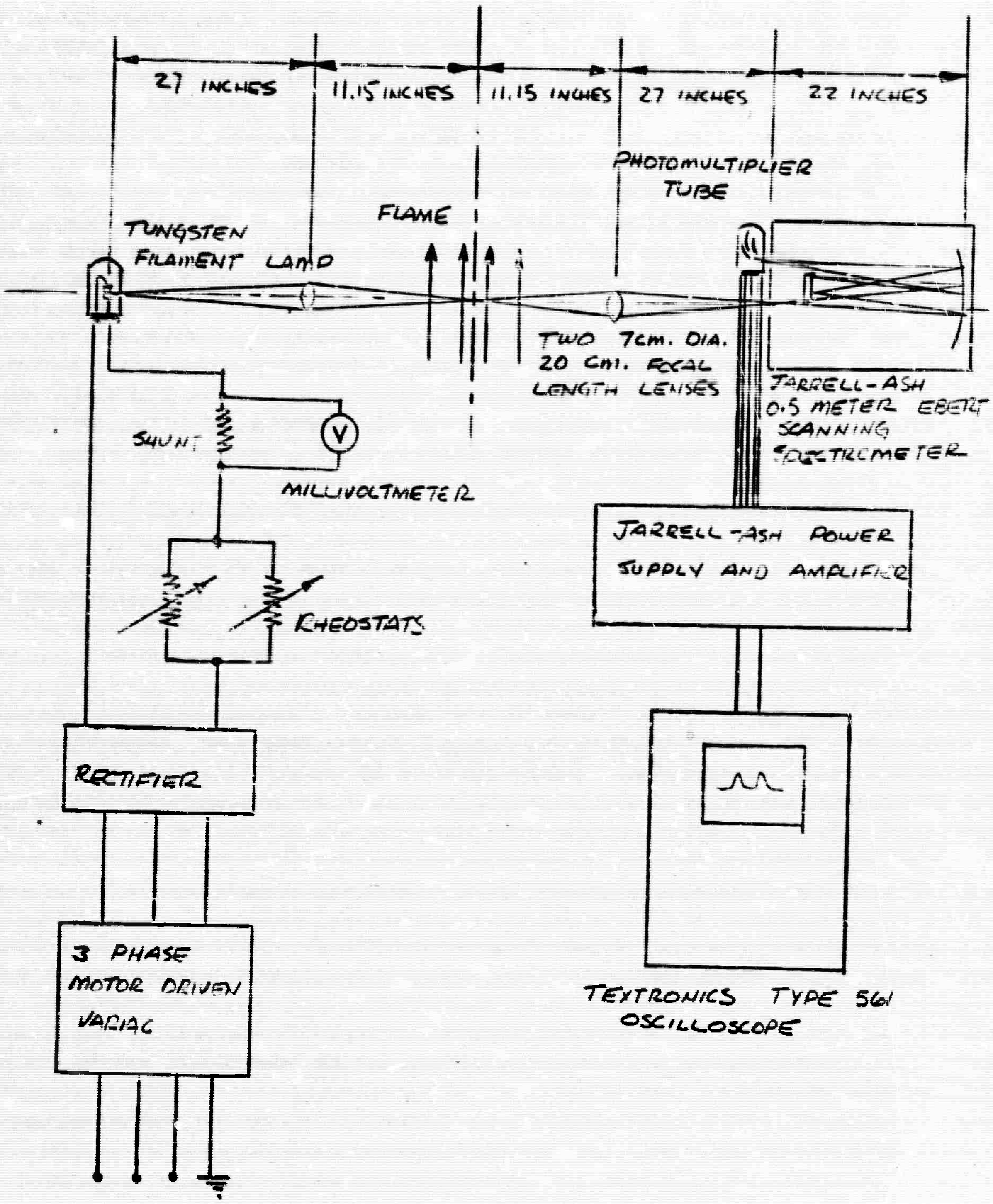

FIGURE A-1 Schematic Apparatus Diagram for Special Line Measurements

1) The radiation density in energy per cm^3 of a black body at temperature T, °K, having wavelengths between λ and $\lambda + d\lambda$ can be formulated by Planck's law

$$u_\lambda d\lambda = \frac{8\pi hc\lambda^{-5}}{\exp \frac{h\nu}{kT} - 1} d\lambda = \frac{c_1\lambda^{-5}}{\exp \frac{c_2}{\lambda T} - 1} \quad d\lambda \qquad (1)$$

where c_1 and c_2 are the first and second radiation constants, $c_1 = 4.992 \times 10^{-15}$ erg cm, $c_2 = 1.439$ cm°K.

2) The radiation intensity I_λ in ergs per sec (watts) per unit solid angle normal to the surface of the blackbody of area A is

$$I_\lambda = \frac{2A\ c_1\lambda^{-5}}{\exp \frac{c_2}{\lambda T} - 1} \qquad (2)$$

3) Wien's law is a very good approximation for $c_2/\lambda T > 5$ in the visible range of the spectrum[18] so that

$$I_\lambda = 2Ac_1\ \lambda^{-5} \exp\left(-\frac{c_2}{\lambda T}\right) \qquad (3)$$

4) The radiation flux over a solid angle Ω is then

$$\phi_\lambda = I_\lambda \Omega \qquad (4)$$

4a) For a non-blackbody with a spectral emissivity ϵ_λ the radiation flux is reduced to

$$\phi_\lambda = \epsilon_\lambda I_\lambda \Omega \qquad (5)$$

5) The brightness temperature of a light source (or non-black body) at a wavelength λ is the temperature at which it is necessary to heat a blackbody so that its

brightness matches that of the light source at the same wavelength. The brightness temperature can be deduced from Equations (3) and (4a) above as

$$\frac{1}{T_o} = \frac{1}{T_t} - \frac{\lambda}{c_2} \ln \epsilon_\lambda \qquad (6)$$

where ϵ_λ is the spectral emissivity at wavelength λ of the emitting body under consideration, T_t is the true temperature, and T_o is the brightness temperature.

6) Correction of light source brightness temperature to different spectral values is frequently necessary in NaD line reversal methods. This is accomplished by means of Eq. (6) above. Let λ be the wavelength of the spectrum line used, i.e., for NaD lines $\lambda = 0.589\mu$, and let λ_ϵ be the calibration wavelength of the light source. Then

$$\frac{1}{T_o(\lambda)} = \frac{1}{T_t} - \frac{\lambda}{c_2} \ln(\epsilon_\lambda)$$

$$\frac{1}{T_o(\lambda_e)} = \frac{1}{T_t} - \frac{\lambda_e}{c_2} \ln(\epsilon_{\lambda e}$$

Subtracting gives

$$\frac{1}{T_o(\lambda)} = \frac{1}{T_o(\lambda_e)} + \frac{\lambda_e}{c_2} \ln(\epsilon_{\lambda e}) - \frac{\lambda}{c_2} \ln(\epsilon_\lambda) \qquad (7)$$

7) For the tungsten filament light source used, the emissivity must be known. Larabee[19] has developed empirical equations in different wavelength regions by assuming linear temperature and wavelength dependence. For $\lambda = 0.450$ to 0.680μ.

$$\epsilon_{\lambda,T} = 0.4655 + 0.1558\lambda + 0.2675 \times 10^{-4}T - 0.7305 \times 10^{-4}\lambda T \qquad (8)$$

8) The brightness temperature required for comparison in the NaD line reversal method is that of the light source at its image position in the flame. It is thus necessary to correct for the absorption and reflection loss of light by any lenses, windows, or filters in the system up to the flame image position. (Such losses after the light has passed through the flame merely reduce the intensity of both the NaD lines and the background light source radiation simultaneously.) A good assumption for most neutral glasses is that the spectral transmission is constant except in the ultraviolet and infared regions where it drops off rapidly[18]. If I_λ is the transmissivity of the glass, the emergent flux will be

$$\phi_{\lambda,\mathrm{emergent}} = t_\lambda \, \phi_{\lambda,\mathrm{incident}} \qquad (9)$$

From this relation, substitution for ϕ_λ from Planck's law[1] can be made to obtain the final corrected brightness temperature T_B of the source at the image position in the flame as

$$\frac{1}{T_B(\lambda)} = \frac{1}{T_o(\lambda)} + a_{\mathrm{lens}} + a_{\mathrm{windows}} + a_{\mathrm{filters}} \qquad (10)$$

where

$$a = \frac{\lambda}{c_2} \ln \frac{1}{t_\lambda} \qquad (11)$$

a is the pyrometric absorption expressed in mireds $(10^{-6} {}^\circ K^{-1})$

b. Theoretical Basis of the Sodium Line Reversal Method

The basis of the NaD line reversal theory is developed below first by the energy balance method for clarity, and the theory is then developed from the equation of transfer for a better understanding of the physical assumptions involved.

1. Energy Balance method

The light beam from the light source at a brightness temperature T_B passes through a gaseous body at temperature T_G. The radiation flux is then specularly isolated by the spectrometer, received by a photomultiplier tube, and displayed for measurement by a suitable instrument. The radiation flux thus measured is the sum of the spectral emission of the gas and the continuous lamp radiation transmitted by the gas. Thus,

$$\phi_{Tot} = \epsilon_\lambda \, \phi_G(\lambda, T_g) + t_\lambda \, \phi_B(\lambda, T_B)^{*} \qquad (12)$$

By assuming thermal equilibrium and applying Kirchoff's law $(\epsilon_\lambda = \alpha_\lambda)$, $t_\lambda = (1 - \alpha_\lambda)$ the above becomes

$$\phi_{Tot} = \epsilon_\lambda \, \phi_G(\lambda, T_G) + (1 - \epsilon_\lambda) \, \phi_B(\lambda, T_B) \qquad (13)$$

The reversal condition is that the total radiative flux is unchanged in the presence of the gaseous body, when this happens, i.e., when $\phi_{Tot} = \phi_B$, then $T_G = T_B$, or the temperature of the gas is equal to the corrected brightness temperature of the light source. When T_G is greater than T_B, ϕ_{Tot} is larger than ϕ_B and the NaD lines appear in emission. When T_G is less than T_B, ϕ_{Total} is less than ϕ_B and the NaD lines appear in absorption. When $T_G = T_B$ the lines are neither in absorption nor emission but would appear to be a continuum on a low resolution spectrometer. When there is a cool boundary layer surrounding a central core region of higher temperature the lines will be a combination of emmission and absorption as viewed by a high

---

*Many references, 4 , 6 , for example, wrongly omit the gas emissivity ϵ_λ before the $\phi_G(\lambda_1 T_G)$ in Equation 12. This would yield the result that the gas emissivity, or absorption coefficient is required before the gas temperature could be determined from the NaD line reversal method. This conclusion is not true, as the following section will demonstrate.

resolution spectrometer. The observable criteria for reversal is then that the integral of the observed flux over the wavelength region of the lines be zero. Reference 16 discusses this effect in detail.

2. Solution of the Equation of Transfer[20]

Assumptions:

a) The flow is one dimensional and planar.
b) The gas is in local thermodynamical equilibrium.
c) The gas is optically transparent.
d) The presence of small amounts of sodium does not affect the properties of the test gas.
e) The electronic excitation of the sodium atoms is in equilibrium with the test gas.

The equation of transfer under these assumptions is

$$\frac{dI_\lambda}{dx} = k_\lambda \, \rho(B_\lambda - I_\lambda) \qquad (14)$$

where k_λ is the mass absorption coefficient of the gas, B_λ is the Planck function*, and ρ is the density of the gas. ($\lambda = 1/k_\lambda\rho$ is the radiation mean free path of the gas). Solving Eq. (14),

$$\int \frac{dn}{n} = - s_\lambda \qquad (14a)$$

where $n \equiv I_\lambda - B_\lambda$ and s_λ is the optical depth of the gas,

$$s_\lambda \equiv \int h_\lambda \, \rho \, d\,x$$

From Eq. (14a),

$$I_\lambda - B_\lambda = c\ e^{-s_\lambda} \qquad (14b)$$

---

*B_λ is derivable from Eq. 1 by use of the relations $\lambda\nu = c$ and $B_\nu = (c/4\pi)u_\nu$; $B_\lambda = 2h\lambda^{-3}c/[\exp(h_\nu/h_T) - 1]$.

Applying the boundary condition that $I_\lambda = I_{\lambda,B}$ (lamp intensity) the above becomes

$$I_\lambda = B_\lambda(1 - e^{-s_\lambda}) + I_{\lambda,B}\, e^{-s_\lambda} \qquad (14c)$$

Integrating Eq. (14c) over the wavelength region of the NaD line gives

$$\int_{NaD} I_\lambda d_\lambda = \int_{NaD} B_\lambda(1 - e^{-s_\lambda})\, d\lambda + \int_{NaD} I_{\lambda,B}\, e^{-s_\lambda}\, d\lambda \qquad (14d)$$

A typical NaD line at the reversal condition is shown below as seen by a spectroscope of high resolving power through a gas with cool edges.

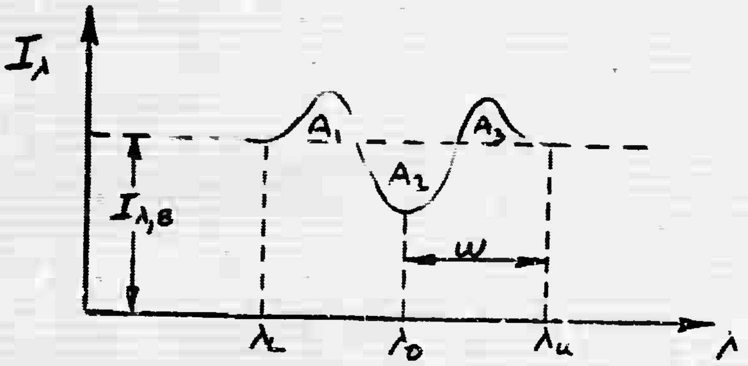

NaD Line at Reversal Condition. The reversal condition is that $A_1 + A_3 = A_2$.

Then, assuming symmetrical wavelength distribution

$$\int_{NaD} I_\lambda\, d\lambda = I_{\lambda,B}(\lambda_u - \lambda_L) = 2w\, I_{\lambda,B} \qquad (14e)$$

Taking B_λ independent of λ over the short region of integration gives

$$2w\, I_{\lambda,B} = B_\lambda \int_{NaD} (1 - e^{-s_\lambda})\, d\lambda + I_{\lambda,B} \int_{NaD} e^{-s_\lambda}\, d\lambda \qquad (14f)$$

or

$$I_{\lambda,B} = B_\lambda + \frac{(I_{\lambda,B} - B_\lambda)}{2w} \int_{NaD} e^{-s_\lambda} d\lambda \qquad (14g)$$

rearranging gives

$$I_{\lambda,B}(1 - \frac{1}{2w} \int_{NaD} e^{-s_\lambda} d\lambda) = B_\lambda(1 - \frac{1}{2w} \int_{NaD} e^{-s_\lambda} d\lambda) \qquad (14h)$$

Thus the condition for reversal gives

$$I_{\lambda,B} = B_\lambda \quad \text{or} \quad T_B = T_G \qquad (14i)$$

which is independent of the optical depth s_λ .

The above analysis contains the additional assumptions that

a) B_λ = constant with respect to wavelength over the NaD line wavelength region.
b) $\lambda_u - \lambda_o = \lambda_o - \lambda_L$; i.e., line symmetry.
c) $I_{\lambda,B}$ = constant with respect to wavelength over the NaD line.

3. Cool Boundary Layer Effects

In actual flow in an MHD generator there is a boundary layer growth along the walls. Any sodium vapor trapped in this cool layer will absorb radiation from the emitted radiation of the central core region of hot gas. The quantities ϕ_{Tot} and ϕ_G measured will then be some mean quantities along the optical path length in the test section. The gas temperature measured is thus a mean temperature $T_{G,m}$ which is less than the true free-stream value $T_{G,t}$. $T_{G,m}$ will depend on the boundary conditions, thermal gradients present in the cool boundary layer, and the number density of sodium atoms present.

Consider a flow consisting of three separate temperature regions, designated 1, 2 and 3. The solution of the equation of transfer through one of these layers is given by Eq. (14.c) as

$$I_1 = B_1(1 - e^{-s_1}) + I_B e^{-s_1} \qquad (15a)$$

where I_B is the radiation intensity incident on layer 1 (corresponding to lamp intensity) and I_1 is the intensity leaving layer 1 and passing on to layer 2. Likewise

$$I_2 = B_2(1 - e^{-s_2}) + B_1(1 - e^{-s_1}) e^{-s_2} + I_B e^{-(s_1 + s_2)} \qquad (15b)$$

where I_2 is the intensity leaving layer 2 and passing on to layer 3.

$$I_3 = I_{Tot} = B_3(1-e^{-s_3}) + B_2(1-e^{-s_2})e^{-s_3} + B_1(1-e^{-s_1})e^{-(s_3+s_2)}$$

$$+ I_B e^{-(s_1 + s_2 + s_3)} \qquad (15c)$$

By taking layers 1 and 3 to be boundary layers with identical temperatures and optical depths, and assuming s_1 and s_3 small, Eq. 15c can be solved for the core condition is

$$B_2 = \frac{I_{Tot} - s_1 B_1(1 + e^{-s_2}) - I_B e^{-s_2}(1 - 2s_1)}{(1 - e^{-s_2})(1 - s_1)} \qquad (15d)$$

The observed mean value is $B_{G,m}$, where for reversal conditions $B_{G,m} = I_{Tot} = I_B$. Thus the relation between the core temperature and the mean temperature observed is

$$B_2 = \frac{B_{G,m}(1 - e^{-s_2}(1 - 2s_1)) - s_1 B_1(1 + e^{-s_2})}{(1 - e^{-s_2})(1 - s_1)} \qquad (15e)$$

For order of magnitude estimates which do not involve the optical depths or B_1, the following equation is convenient[18]

$$\frac{1}{T_{G,m_{min}}} = \frac{1}{T_{G,t}} - \frac{\lambda}{c_2} \ell n\left(1 - \frac{2\delta}{L}\right) \qquad (16)$$

where $T_{G,m_{min}}$ is a minimal mean temperature, $T_{G,t}$ is the true core region gas temperature, δ is the boundary layer thickness, and L is the flow width across which the light beam passes. The temperature measured lies somewhere between $T_{G,m_{min}}$ and $T_{G,t}$.

III. Sodium Line Reversal Method: Experimental

a. Apparatus

1. Light Source

The light source used in the present experimental facility (see Figure 1) is a calibrated General Electric tungsten filament lamp, model number 18A(T10)1. The calibration covers the true temperature range from 2600°K to 3200°K. The lamp power supply is a motor driven three phase variac and rectifier which provides up to 25 amperes of rectified direct current. Two 27 ampere rheostats are connected in parallel to provide fine current control. The current to the lamp is determined by precisely measuring the voltage drop across an accurate 25 ampere shunt. Due to the thermal lag of the lamp filament, the rectification ripple is not observable when the lamp radiation is measured with the spectrometer appratus utilized. The power supply-lamp system has proven to be extremely stable and thus reliable for the spectral line reversal method.

2. Spectrometer System

A Jarrell-Ash half-meter Ebert scanning spectrometer has been temporarily borrowed for determination of spectral intensities. This instrument has proved to be highly successful for the spectral line reversal measurements. The Jarrell-Ash power supply for the photomultiplier and the photomultiplier output amplifier for the above spectrometer are combined into one unit, the output is recorded on a Textronics Type 561 oscilloscope with maximum sensitivity of 1 mv/centimeter. The spectral line profile is obtained by photographing the sweep of the oscilloscope over the spectral line wavelength region by a time exposure with the Polaroid attachment provided with the oscilloscope. The spectral line can also be observed directly on the oscilloscope.

3. Lenses

The lenses utilized for the present apparatus are two glass 7 centimeter diameter, 20 centimeter focal length identical lenses. Their arrangement in the optical design is dictated by the internal optical arrangement of the Jarrell-Ash spectrometer. The optical design is shown in Figure 1.

b) Experimental Observations

Typical examples of the NaD lines as seen in the small propane flame are shown on Figures 3, 4, 5, and 6. The temperature of the flame is determined to be 2135°K as seen from Figure 6, bottom. The temperature measurements have been determined to an observable experimental accuracy of 10°K. By this it is meant that two different output spectral line shapes corresponding to a difference of 10°K in flame temperature are easily distinguished and accurately measured. Measurements on the MHD channel at the plenum chamber exit, exhausting to the atmosphere, have shown good results with the existing apparatus. Preliminary results show excellent line shapes and reversal lines with a sodium seed concentration of less than 0.001%. The temperatures determined by the spectral line reversal method agree well with the theoretical calculations for the particular flow rates chosen.

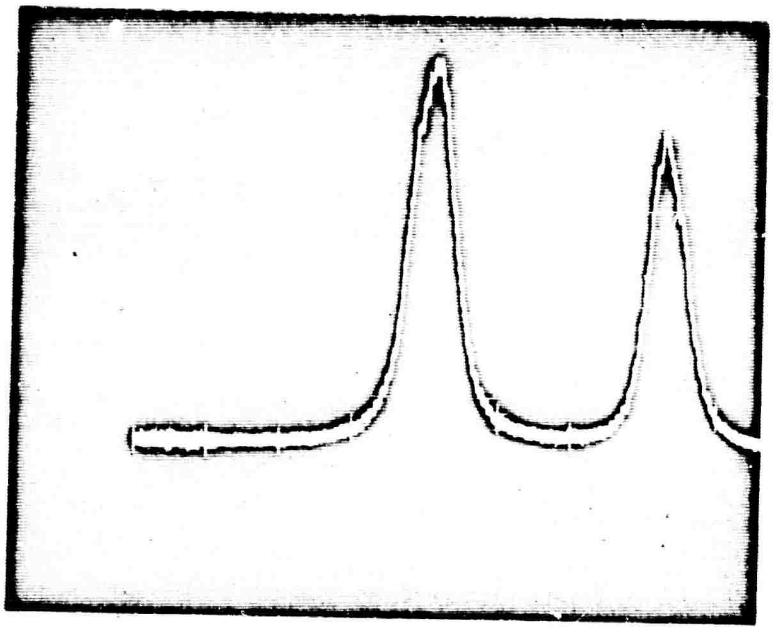

FIGURE A-2 5890 and 5896 Å NaD lines in emission. Light source off. 10 millivolt per division, 0.2 seconds per division.

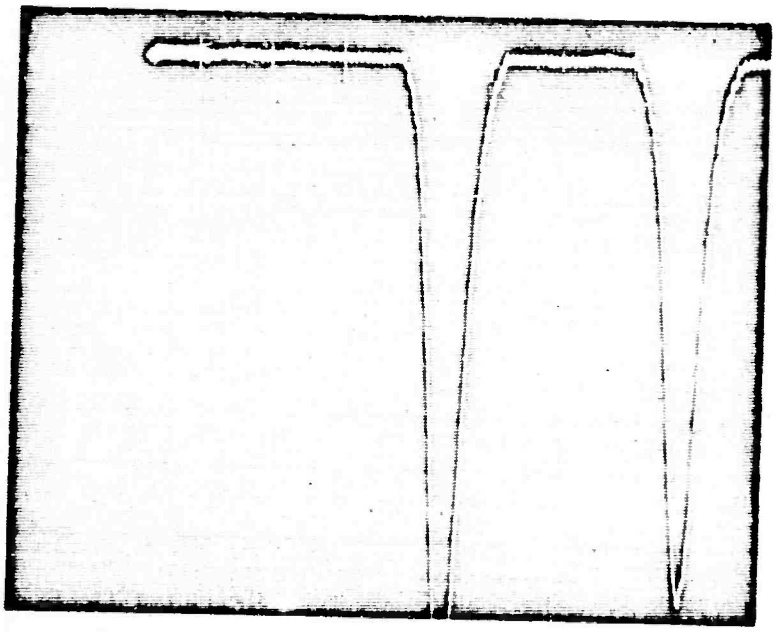

FIGURE A-3 5890 and 5896 Å NaD lines in absorption. 15.80 amperes lamp current.

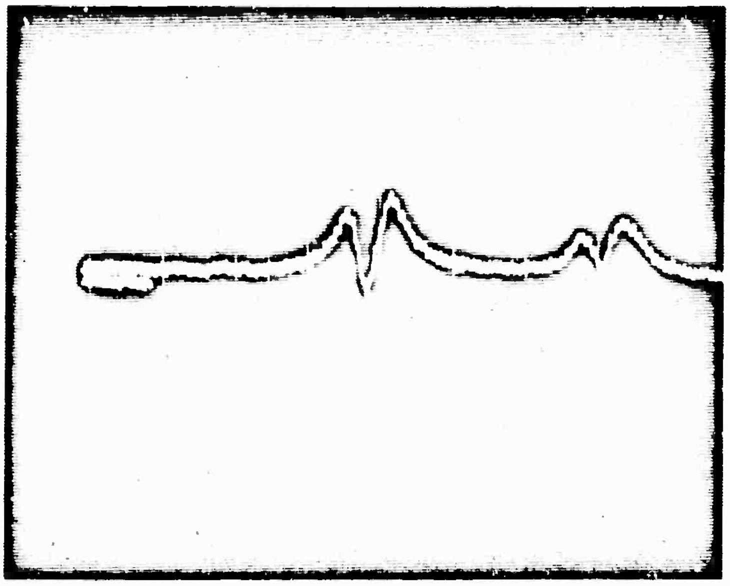

FIGURE A-4 NaD lines near reversal condition but slightly in emission. 12.65 amperes lamp current, corresponding to a gas temperature of 2125°K.

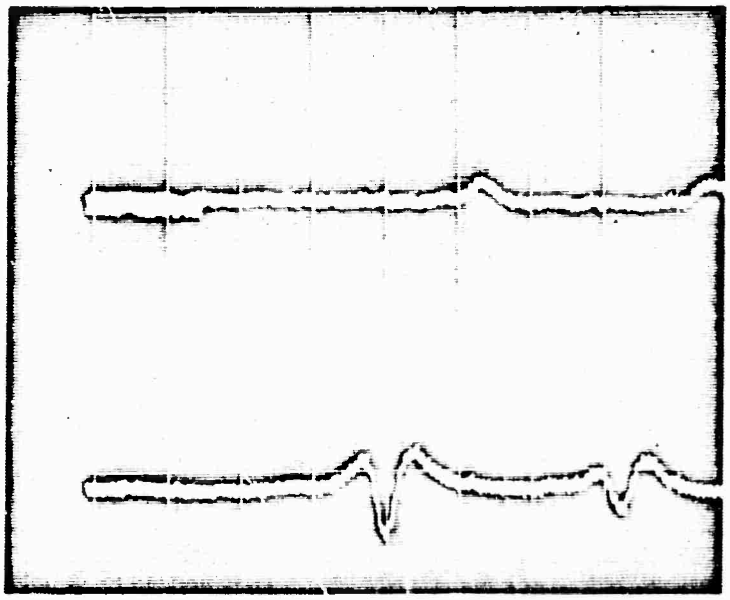

FIGURE A-5 Top: NaD lines near reversal conditions. 12.50 amperes, 2110°K.

Bottom: NaD lines at reversal conditions. 12.78 amperes. Gas temperature determined to be 2135°K.

REFERENCES

1. Frost, L. S., Jour. Appl. Phys. 32, p. 2029, 1961.
2. Allis, W. P., "Handbuch der Physik", 21, Springer, Berlin, 1956.
3. Quarterly Technical Summary Report on Direct Energy Conversion Systems, Contract AF 29(638)-1123, June 30, 1964.
4. Kihara, T., and Aono, O., Jour. Physical Society of Japan, 18, p. 837, 1963.
5. Itikawa, Y., Jour. Physical Society of Japan, 18, p. 1499, 1963.
6. Rynn, N., "Macroscopic Transport Properties of a Fully Ionized Alkali-Metal Plasma", Phys. Fluids, 7, 284(1964).
7. Kerrebrock, J. L., "Conduction in Gases with Elevated Electron Temperatures," Second Symposium on Engineering Aspects of Magnetohydrodynamics, (Columbia University Press, New York, 1962), pp. 327-346; and AIAA Journal 2, 1072(1963).
8. Kerrebrock, J. L., and M. A. Hoffman, AIAA Journal 2, 1080 (1963).
9. Zukoski, E. E., T. A. Cool and E. G. Gibson, "Experiments Concerning Nonequilibrium Conductivity in a Seeded Plasma," AIAA Aerospace Sciences Meeging, New York, New York, Jan. 1964.
10. Morse, T. F., Phys. Fluids, 6, 1420 (1963).
11. Brown, S. C., Basic Data of Plasma Physics, (Technology Press, MIT, and John Wiley and Sons, Inc., New York, 1959), pp. 5-7.
12. Massey, H. S. W., and E. H. S. Burhop, Electronic and Ionic Impact Phenomena (Clarendon Press, Oxford, 1952.
13. Fery, Ch., Compt. rend. 137, 909 (1903).
14. Kohn, H., Ann. Physik, 44, 749 (1914).
15. Hershey, A. E. and R. F. Paton, "Flame Temperatures in an Internal Combustion Engine Measurement by Spectral Line Reversal," Univ. of Ill. Bulletin, Vol. XXXI, No. 9, (1933).

16. Bundy, F. P. and H. M. Strong, "Measurement of Flame Temperature, Pressure, and Velocity," Vol. IX, Part 2, Section I; High Speed Aerodynamics and Jet Propulsion, Princeton University Press, (1954).

17. Gaydon, A. G. and H. G. Wolfhard, "Flames, Their Structure, Radiation, and Temperature," Chapman and Hall Ltd. (1960).

18. Mak, W. H., "Sodium Line Reversal Temperature Measurements in Shock-Tube Flows," UTIA Technical Note No. 66, (May 1963).

19. Larabee, R. D., "Spectral Emissivity of Tungsten," Journal of the Optical Society of America," Vol. 29, 619, (1959).

20. Private Communication, Dr. R. Wienecke.

II. ELECTROCHEMICAL CONVERSION

A. The Effects of Free-Stream Turbulence on the Limiting Current Density at the Front Stagnation Point of a Translating Cylinder Electrode

Introduction

The overall rate of conversion in an electrochemical reaction may be controlled by either of two processes· the rate of conversion at the electrode surface, or the diffusion of the reactants through the boundary layer. For the systems which are chemically slow-reacting, the diffusion process is relatively fast and the electrode surface concentration of reactants is equal to the bulk concentration. The bulk concentration would be a known parameter of the system.

Controlled hydrodynamical techniques are used to study the very fast electrochemical reactions, where the process may be, at first diffusion controlled. If the rate of diffusion may be systematically controlled, it may be possible to approach a regime where the overall rate is again governed by the kinetics. If, in addition, it is possible to express the diffusional process from a theoretical standpoint, it would be possible to study the kinetics during the intermediate regime since the surface concentration would be known from theoretical considerations. It would be impossible to say anything about the surface concentration in a completely diffusional-controlled system.

The rotating disk electrode and the translating cylinder electrode have been used, successfully, to study the faster electrochemical reactions. Both of these devices offer an electrode surface of uniform concentration; if, in addition, the entire surface is maintained at a constant potential. The laminar boundary layer theory for the rotating disk was first presented by Levich (4). The theory for the translating cylinder and its possible use as an electrochemical tool was first suggested by Bopp and Mason (2).

The interest here lies in the effect of the free stream turbulence generated by the cylinder upon the laminar boundary layer at the front stagnation region. It must be demonstrated that the laminar boundary layer theory is, indeed, applicable, and to within what experimental limitations it may be applied.

Experimental Apparatus and Procedure

With the exception of a few modifications, the experimental arrangement which was used here corresponds to that used in the studies by Bopp and Mason (2). The tank was a standard cylindrical pyrex jar, 25. 4 cm. high and 25. 7 cm. O. D. , closed at the top by a 1. 9 cm. thick lucite flange . The tank rested on an aluminum plate which contained four vertical studs. The studs rose up through the top flange with the flange then being secured to the tank by four nuts (See Fig. 2, Ref. 2). A Viton A ring gasket offered an effective seal between the lucite flange and the top of the pyrex tank. Four vertical baffles were placed inside the tank and connected to the top flange by nylon screws. Any number of the baffles could then be removed if it was so desired. The bearing housing and shaft arrangement is shown schematically in Fig. 7 of Bopp and Mason (2). The shaft rotated on two bearings, 3. 8 cm. apart. The bearings were sealed from the solution in the tank by a Teflon-lined Viton-A annular cylinder, 0. 25 inch I. D. by 1. 0 inch O. D. and 0. 5 inch thick. The entire essembly was attached to the top flange by six screws at the base of the bearing housing. The shaft was coated with an epoxy resin to reduce the damage due to chemical attack. A Heller type GT21 laboratory mixer and controller was used to rotating the shaft. By varying the pully ratios between the motor and the shaft, rotational speeds of from 2 rpm to 170 rpm could be maintained and controlled quite successfully. The auxiliary electrode, a 3. 57 cm. by 4. 45 cm. piece of platinized platinum, was placed on the base of the tank. A 60 cm. length of 25 ml. platinum wire was spot-welded to the auxiliary electrode and drawn up along one of the baffles and out the fuel port. The lead from the test electrode in the cylinder was drawn up through the hollow shaft into a mercury dish, which rotated on the shaft. The circuit was then completed by dipping another external lead into the dish. A lugin-type calomel electrode was used as a reference electrode. The capillary tube extended down into the supporting electrolyte through the top flange. A gas-bubbler was also supplied through the top flange. Nitrogen gas was continually swept through the solution to prevent the build-up of dissolved oxygen in the supporting electrolyte. Three Teflon Swagelock fittings were used in conjunction with the three ports in the top flange. A model 855B power supply from the Harrison Laboratories was used to control the potential between the test and the reference electrodes. A J-Omega type 21A D. C. volt-Ohm meter was used to monitor the applied potential. The current was recorded on a Moseley Autograph X-Y Plotter. The rotational speeds were measured, to within an accuracy of about 2 °/o, by a hand stop watch.

The electrode surfaces were cleaned in a strong solution of KOH for periods up to one-half hour. They were then used and placed in a 50 °/o aqua regia solution for fifteen minutes. Finally the electrodes were cathodized for one to two hours in 0. 1N H_2SO_4 at 100 $\frac{ma}{cm^2}$ before being placed into the test solution.

Procedure:

The voltage was first adjusted, either cathodically or anodically, until the system was operating on the current plateau (Fig. 1). Once a rotational speed was selected, three minutes were allowed before the X-Y Plotter was engaged. After each run, five minutes elapsed before the cylinder was again rotated. Any turbulence which had been previously generated was, by then, dampened out.

Discussion

Electrochemical

Consider the electrochemical reaction occurring between species R and Ox:

$$R \rightleftarrows Ox + ne^-$$

where n electrons are transfered per mole of reactant. One may write the rates of reaction for the forward and reverse steps, assuming for example 1st order, as:

$$\left.\begin{aligned} r_f &= C_R^{(s)} j_o \exp.\left[\frac{-\alpha \eta n F}{RT}\right] \\ r_b &= C_{Ox}^{(s)} j_o \exp.\left[\frac{(1-\alpha)\eta n F}{RT}\right] \end{aligned}\right\} \qquad (1)$$

where

r_b, r_f - rate of reverse and forward reaction

$C_R^{(s)}$, $C_{Ox}^{(s)}$ - surface concentration of R and Ox

j_o - rate constant

α - transfer coefficient

F - Faradays constant 96,500 $\frac{\text{coulombs}}{\text{equivalent}}$

n - number of equivalents per mole

R - gas constant

T - temperature

η - overvoltage

At the equilibrium rest potential, $\eta = 0$. The sign of η determines whether one is operating cathodically or anodically. As the overvoltage is increased anodically, the rate of the forward reaction increases with respect to the reverse reaction (Eq. 1). The current density measured at the electrode will then increase from zero and reach a plateau. The plateau will occur when $(r_f - r_b)$ is sufficiently large that the system becomes diffusion controlled. The ratio of the forward to reverse rates of reaction may be formed directly from Eq. 1:

$$\frac{r_f}{r_b} = \frac{C_R^{(s)}}{C_{ox}^{(s)}} \exp.\left[\frac{\eta n F}{RT}\right] \tag{2a}$$

In the diffusion controlled regime, the value of $C_R^{(s)}$ is at least two orders of magnitude less than the bulk concentration. If the two species have Schmidt numbers of the same order of magnitude, $C_{Ox}^{(s)}$ will be about double the bulk value. Thus, if the solutions are equimolar in the bulk, for $n = 1$

$$\begin{aligned}\frac{r_f}{r_b} &= \frac{10^{-2} C^{(\infty)}}{C^{(\infty)}} e^{-35\,\eta} \\ &= 10^{-2} e^{-35\eta}\end{aligned} \tag{2b}$$

The surface concentration of R may be less than $10^{-2} C_R^{(\infty)}$ but an anodic overvoltage of 0.300 - 0.400 volts (η is negative) is usually sufficient to reach the plateau. Figure 1 shows a polarization curve obtained for the oxidation of the ferrocyanide ion to the ferricyanide ion in 1 M KCl.

Hydrodynamics

The co-ordinate system which is used for two dimensional boundary-layer flow past a cylinder is chosen such that the positive y-axis extends out away from the cylinder in the radial direction and the positive x-axis increases clockwise in the circumferential direction from the front stagnation point. Of interest here is the asymptotic case of $Re \to \infty$, $Sc \to \infty$. The flow and continuity equations may be written in dimensionless form with all velocities relative to U_∞ and all lengths relative to the cylinder diameter, d:

$$\left.\begin{aligned} u\frac{\partial u}{\partial x} + v\frac{\partial u}{\partial y} &= \frac{1}{Re}\frac{\partial^2 u}{\partial y^2} - U(x)\frac{dU(x)}{dx} \\ \frac{du}{dx} + \frac{dv}{dy} &= 0 \end{aligned}\right\} \qquad (3a)$$

For flow past the front stagnation point of a cylinder $U(x) = x$ (4). Letting $u = xf'(\eta)$, with $\eta = \sqrt{Re}\, y$, Eq. 3a may be transformed to

$$f''' + ff'' + (1 - f'^2) = 0 \qquad (3b)$$

Equation 3b has been solved numerically and $f(\eta)$ is tabulated in Schlichting (4).

Defining a dimensionless concentration, $\theta = \frac{C - C^{(\infty)}}{C^{(s)} - C^{(\infty)}}$ where $C^{(\infty)}$ is bulk and $C^{(s)}$ is the surface concentration, one may write the mass transfer equations as:

$$u\frac{\partial \theta}{\partial x} + V\frac{\partial \theta}{\partial \eta} = \frac{1}{Sc}\frac{\partial^2 \theta}{\partial \eta^2} \qquad (4)$$

where $V = \sqrt{Re}\; v$

Boundary conditions

$\eta = 0 \qquad \theta = 1$

$\eta \to \infty \qquad \theta \to 0$

For $Sc \to \infty$, the mass boundary layer is much thinner than the momentum boundary layer. One may, then, expand u linearly in η. Thus:

$$u = \left.\frac{\partial u}{\partial \eta}\right|_{\eta=0} \eta = \beta(x)\eta$$

and

$$V = -\frac{1}{2} \frac{d}{dx} \left[\beta(x)\right] \eta^2 \tag{5}$$

One may eliminate Sc from Eq. 4 by letting $z = Sc^{1/3}\eta$. Under the above transformations, one obtains the new equation (1):

$$\beta(x) \frac{\partial\theta}{\partial x} - \frac{z^2}{2} \frac{d}{dx} \left[\beta(x)\right] \frac{\partial\theta}{\partial z} - \frac{\partial^2\theta}{\partial z^2} \tag{6}$$

Let

$$\theta = \theta\left(\frac{z}{g(x)}\right) = \theta(\xi)$$

Thus

$$\frac{\partial^2\theta}{\partial\xi^2} + \xi^2 \frac{\partial\theta}{\partial\xi} \left[\beta(x) g^2 g' + \frac{g^3}{2} \frac{d\beta}{dx}\right] = 0 \tag{7a}$$

If one sets

$$\beta(x) g^2 g' + \frac{g^3}{2} \frac{d\beta}{dx} = 3$$

then

$$g = \frac{(9)^{1/3}}{\sqrt{\beta}} \left[\int_0^x \sqrt{\beta(t)}\, dt\right]^{1/3}$$

The choice of 3 is quite arbitrary. Eq. 7a becomes

$$\frac{\partial^2\theta}{\partial\xi^2} + 3\xi^2 \frac{\partial\theta}{\partial\xi} = 0 \tag{7b}$$

Boundary Conditions

$\xi = 0 \qquad \theta = 1$

$\xi \to \infty \qquad \theta \to 0$

Solving Eq. 7b under the imposed boundary conditions

$$\theta = \frac{\int_{\xi}^{\infty} e^{-t^3}\, dt}{\Gamma\left(\frac{4}{3}\right)} \qquad (8)$$

The diffusional flux of the i^{th} component to the surface may now be easily calculated.

$$= -D_{im} \left.\frac{\partial c}{\partial y}\right|_{y=0} = \frac{D_{im} Re^{1/2} Sc^{1/3}\left(C^{(\infty)} - C^{(s)}\right)_i}{d} \; \frac{\sqrt{\beta}}{9^{1/3}\,\Gamma\left(\frac{4}{3}\right)} \left[\int_0^x \sqrt{\beta(t)}\, dt\right]^{-1/3} \qquad (9a)$$

with

$$\beta(x) = f''(0)\, U(x) = 1.2326x$$

Thus

$$= \frac{D_{im}\left(C^{(\infty)} - C^{(s)}\right)_i}{d}\left[0.660\, Re^{1/2}\, Sc^{1/3}\right]. \qquad (9b)$$

The diffusion-controlled current depicted by the plateau of Fig. 1 corresponds to the condition $\left(C^{(s)}\right)_i \rightarrow 0$. The current is related simply to the concentration gradient at the electrode by:

$$I = -n F D_{im} \left.\frac{\partial c_i}{\partial y}\right|_{y=0} \qquad (10)$$

where

n = charge of i^{th} component

$F = 96{,}500 \; \frac{\text{coulombs}}{\text{equivalent}}$

For the translating electrode, Eq. 9 may be put into a more convenient form. Let:

$$U_{\infty} = \frac{R_s \pi}{30} \Omega$$

where

Ω = rotational speed (rpm)

R_s = shaft radius

Thus

$$I_i = (4.025 \times 10^4) n \nu^{1/6} D_{im}^{2/3} \left(\frac{R_s}{d}\right)^{1/2} \Omega^{1/2} C_i^{(\infty)} \qquad (11)$$

Figs. 4, 5, and 6 are graphs indicating the linearity of I with $\Omega^{1/2}$ for the ferricyanide-ferrocyanide system.

The theory presented above is for free stream flow past a stationary cylinder. It is more practical, however, to rotate the cylinder in a stationary bed of fluid. The equations presented above are applicable to both flow systems if the boundary conditions are the same. Translating the cylinder through a stationary fluid does, however, create a certain degree of free stream turbulence. The boundary conditions at the outer edge of the boundary layer will not, therefore, be identical to those used in the formulation of Eq. 11. The use of laminar boundary layer theory to describe the translating cylinder must be justified experimentally. It is clear at the outset that there will be certain limitations. The size of the cylinder will determine the intensity of the free stream turbulence, and if deviations from the laminar theory occur, they will be predominant with the larger cylinders.

Experimental Results

The potassium ferricyanide-ferrocyanide system has been selected for this work since it has been studied by other investigators and has been shown to be, electrochemically, a relatively rapid reaction. Of initial interest are the values of the diffusion coefficients for the reduced and oxidized species. These values have been calculated by other workers (3, 6) using various techniques and supporting electrolytes. The values which have been obtained here are given in Table III. The values have been obtained from a least squares analysis of the slopes of the graphs shown Figs. 4, 5, and 6 in accordance with the laminar boundary layer theory presented in the previous section. These graphs are bound in a region of Reynolds number from 200 to 8,000 and are well within the limits of the laminar boundary layer theory.

The tank, as mentioned in the previous section, has been equipped with four equally spaced baffles around its perimeter. The baffles offer resistance to the main body of the fluid and reduce the overall rotation of the bulk. Observations of small particles in the fluid indicated that at least until the point where free stream turbulence began to control the transport process the bulk rotation was negligible. If the fluid were rotating in the bulk the apparent Reynolds number would be greater than the actual value and in curves similar to Figs. 7, 8, 9, and 10 the values of the current density would tend to fall below the line given by the laminar theory. This was, however, never observed.

Figure 3, which is a graph of the frequency of turbulence as a function of rotational speeds indicates that turbulence may be present in the tank at relatively low Reynolds numbers. The frequency increases rapidly at the lower rotational speeds and then tends to level off with increase speed of rotation. The graph shows points taken with all of the cylinders, and with the exception of the large electrode on the 1" cylinder, the frequencies are of the same order of magnitude independent of Reynolds number, and a function only of the rotational speed. The 1" cylinder gave lower frequencies for a given speed. The amplitude of the fluctuation is, however, a marked function of the cylinder size, decreasing with decreasing diameter of the cylinder. This is, indeed, what one might intuitively expect if it is the cylinder itself which is creating the free stream disturbances which are in turn causing the current fluctuations. The variation of current amplitude with cylinder size is given in Table IV. The current fluctuations which were recorded are direct measures of the fluctuations in the concentration gradient through the mass boundary layer. Since $C^{(\infty)}$ is a constant and $C^{(s)} \rightarrow 0$, the fluctuations indicate that the boundary layer thickness is oscillating due to the influence of the free stream turbulence.

As would be expected, the size of the cylinder is a key factor in determining the turbulent characteristics of the system. Figures 7 through 16 are graphs of the current and the square root of the rotational speed. The currents have been taken as the mean of the fluctuations. In Figure 12, where there is no apparent curvature, the linear portion extends from a frequency of 0.08 c.p.s. to about 3.00c.p.s. Since the line extends to such small frequencies, where the laminar theory would apply, if anywhere at all, it can be argued that the mean of the fluctuation is given by the laminar theory up to the point of curvature. It is upon this basis that the linear portion has been used to determine diffusion coefficients.

Equation 11 indicates that from the standpoint of the boundary layer theory it would be advantageous to make the size of the cylinder as small as feasible. Thus, although for a given rotational speed the Reynolds number has decreased, the concentration gradient has increased. As will be indicated subsequently, however, there is a practical limitation to the cylinder size as governed by the size of the electrode. Figures 7, 8, 9, and 10 show that the rotational speed at which curvature begins increases as the cylinder diameter decreases, with no apparent curvature present in Figures 11, 12, and 13. The increase in Nusselt number must be attributed to free stream turbulence and not premature tripping of the momentum boundary layer. Indeed, curvature has been observed in the region of Reynolds numbers from 3,000 - 10,000 where the boundary layer should be quite stable with respect to external effects.

It can also be shown that the width of the electrode surface governs the onset of curvature. Figures 7, 8, and 9 depict the current-speed behavior in the same tank with the same size cylinder, but with different size electrodes. When one averages the Nusselt number over a larger surface area, the curvature begins at a lower speed. By reducing the angle of the electrode from 8° to less than 1° the speed at which curvature begins may be increased by 45 °/o. This effect is brought about even more vividly in Figure 14 where the current-speed graph is given for the 0.125" cylinder. Although this cylinder was small enough to cause small amplitude fluctuations, as given in Table IV, the angle of the electrode was 14°, large enough to cause curvature at a Reynolds number of 3,000. The average Nusselt number will vary linearly with the square root of the Reynolds number, and independently of the size of the electrode, if the velocity in the potential flow regime varies linearly with x. Since curvature appears with the small cylinder at an angle of 14°, the free stream turbulence introduces higher order terms in x much sooner than the laminar theory would predict. For the boundary layer theory an angle of 20° should still suffice for the stagnation region. Figures 7, 8, and 9 with the 1" cylinder indicates that the higher order terms come into play at smaller values of the x-coordinate when the scale of turbulence increases.

It is also of interest to note that in Figures 7 and 9 after the transition from the initial straight line occurs, the graph assumes a new line with a larger slope. It is possible to explain this behavior if a quasi-steady state mechanism is assumed for the mass and momentum transport processes in the presence of turbulence. In a quasi-steady state sytem the velocity and concentration profiles are assumed to satisfy the time-independ transfer equations (Eq. 3) at any instance of time. Under the framework of the boundary layer transformation the spacially dependent Nusselt number may be expressed, for any geometry or potential velocity field, as

$$Nu(x) = b(x) Re^{1/2} Sc^{1/3} \tag{12}$$

This is the asymptotic expression for $Sc \to \infty$. For stagnation regime flows $b(x) \equiv$ constant. In Equation 12 the $N\bar{u}(x)$ has been time averaged, and the average value is assumed to be time independent. Observations of the current fluctuations in Figure 2, indicate that the mean current is independent of time, supporting this assumption. As the free stream velocity alters its spacially dependent character with changes in the intensity of turbulence, b(x) becomes a function of rotational speed. As mentioned above, the frequency of turbulence appeared to level off after its initial rapid rate increase. If this may be taken as also a region where the turbulent effects level off, then b(x) would become only a function of x again. Thus

$$\frac{\int_0^{x_0} Nu(x)dx}{x_0} = N\bar{u} = \frac{Re^{1/2} Sc^{1/3} \int_0^{x_0} b(x)dx}{x_0}$$
$$= Re^{1/2} Sc^{1/3} a(x_0).$$

In Figs. 7, 8, and 9 the size of the electrodes were constant, thus $a(x_0)$ would be a parameter of the system. The system would then become linear again with the square root of Reynolds number. This argument can only be substantiated more conclusively after further studies on the effects of the electrode size on the average value of the Nusselt number.

At the present there is no clear explanation for the difference in the observed points of curvature anodically and cathodically. The solutions were equimolar in ferri-and ferro-constituents and diffusion coefficients. This result was reproducible in a series of runs. It might be possible that an explanation lies in the elucidation of the effects of transporting a charged species through an oscillating velocity field. The curvature cannot be attributed entirely, however, to the charge of the species being transported to the surface of the electrode since curvature was also obtained with the hydrogen gas ionization reaction as shown in Figs. 15 and 16. Here the species of importance is the neutral H_2 molecule. Also, decreasing the size of the electrode increased the rotational speed at which the onset of curvature was noted for the hydrogen system. This is shown in Fig. 16.

Conclusions

Although the frequency of turbulence did not appear to be a function of the cylinder size, the amplitude did decrease as the cylinder diameter decreased. The 1" and 3/4" cylinders gave curvature whereas the 1/2" and 1/4" cylinders obeyed the laminar theory in the range of rotational speeds that were investigated (2 - 170 rpm). The curvature in the 1/8" cylinder is attributed to the large angle (14°) which the electrode subtends in the front face of the cylinder. Changing the angle from 8° to 1° in the 1" cylinder increased the speed at which curvature commenced by 45 °/o. It should be observed, though, that although curvature in the 1/8" cylinder occurred at a Reynolds number of about one-third that of the 1" cylinder, the current corresponding to the point of curvature was about three times as large for the 1/8" relative to the 1" cylinder. It would, of course, be possible to use a cylinder-electrode arrangement that gave curvature if the kinetics-controlled regime remained bounded below the region of curvature. It still must be verified experimentally that when one approaches the kinetics-controlled regime, that the presence of a non-vanishing surface concentration does not initiate deviations from the laminar theory. As was noted above, the point of curvature was different anodically than cathodically, suggesting that the charge of the species plays some role in the deviation from linearity. It should also be possible, after further experimentation, to correlate the data and obtain an empirical fit for the second linear portion of the graphs in Figures 7 and 9. The correlation would involve varying the size of the cylinder, electrode, and possibly the ratio of the shaft radius to tank radius. An empirical relation, if so obtained, would greatly increase the region of applicability of the translating cylinder electrode.

Acknowledgment

The authors would like to express their graditude for the many helpful criticisms and suggestions offered by Dr. Z. Rotem and Dr. P. Stonehart pertaining to the various aspects of the problem at hand. The many hours of actual experimental work performed by Mr Edward Sakata and Mr. Charles Lappel are also gratefully acknowledged. The financial support for the project was supplied by the Advanced Research Projects Agency, Contract Number AF 49(638)1123.

Table I

Nomenclature

C	concentration (moles/cc)
D	diffusion coefficient $\frac{cm^2}{sec.}$
d	diameter of lucite cylinder (cm)
e^-	electrons
F	Faraday equivalent 96,500 $\frac{\text{coulombs}}{\text{equivalent}}$
f	dimensionless stream function
g(x)	function of x used in similarity transformation $\frac{(9)^{1/3}}{\sqrt{\beta}}\left[\int_0^x \sqrt{\beta(t)}\ dt\right]^{1/3}$
I	current density $\frac{ma}{cm^2}$
i	total current (ma)
n	number of electrons transferred in electrochemical reaction
Re	Reynolds number
Sc	Schmidt number
P	total pressure-atmospheres
R	universal gas constant $\frac{2\ \text{calories}}{\text{gm-mole-}^{\circ}\text{K}}$
R_s	radius
T	absolute temperature °K
t	dummy integration variable
u	x-component of velocity in boundary layer
U(x)	x-component of velocity at outer edge of boundary layer
U_∞	free stream velocity
V	$\sqrt{Re}\ v$
v	y-component of velocity in boundary layer
x	co-ordinate measured along circumferential direction from leading edge of cylinder

y	co-ordinate measure radially from surface of cylinder
z	$Sc^{1/3}\,\eta$ - radial co-ordinate scaled by $Sc^{1/3}$

Greek Symbols

β	dimensionless velocity gradient at wall $- \left.\frac{\partial u}{\partial y}\right\|_{y=0}$
Γ	gamma function
η	overvoltage-dimensionless radial co-ordinate scaled by $Re^{1/2}$ - $Re^{1/2}\,y$
Ω	angular velocity (rpm)
ν	kinematic viscosity $\frac{cm^2}{sec}$
ρ	density $\frac{gms}{ml}$
ξ	similarity transformation variable $\frac{z}{g(x)}$
Θ	dimensionless concentration ratio $\frac{C - C^{(\infty)}}{C^{(s)} - C^{(\infty)}}$

Subscripts and Superscripts

i	individual species
m	mixture
s	conditions at electrode surface
∞	conditions in bulk electrolyte

Table II

Calculation of Diffusion Coefficients for $K_4Fe(CN)_6$ and $K_3Fe(CN)_6$ in KCl

Electrode - Platinized Platinum
Area - 0.42 cm^2
Voltage - 0.600^v N. H. E.
Electrolyte - 1.0 M KCl

Ω (rpm)	$\Omega^{1/2}$	i(ma)	I $\frac{ma}{cm^2}$
2.1	1.45	0.345	0.823
3.8	1.95	0.450	1.074
6.1	2.47	0.560	1.337
9.5	3.08	0.680	1.623
12.5	3.54	0.790	1.885
16.2	4.03	0.900	2.148
20.3	4.51	1.020	2.434

$$D_{Fe(CN)_6^{-4}} = 5.19 \times 10^{-6} \text{ cm.}^2/\text{sec.}$$

2.32	1.52	0.350	0.835
0.979	0.989	0.220	0.525
5.43	2.33	0.520	1.241
7.06	2.66	0.590	1.408
3.48	1.87	0.425	1.014
2.30	1.52	0.350	0.835
5.54	2.35	0.520	1.241
11.10	3.33	0.730	1.742
14.10	3.76	0.810	1.933
18.20	4.27	0.920	2.196

$$D_{Fe(CN)_6^{-4}} = 5.11 \times 10^{-6} \text{ cm.}^2/\text{sec.}$$

Table II (cont)

Electrode - Platinized Platinum
Area - 0.42 cm^2
Voltage - -.175^v N. H. E.
Electrolyte - 1.0 M. KCl

Ω (rpm)	$\Omega^{1/2}$	i(ma)	I $\frac{ma}{cm^2}$
10.2	3.19	0.73	1.742
11.62	3.41	0.77	1.838
14.90	3.86	0.87	2.076
17.75	4.21	0.94	2.243
24.30	4.93	1.10	2.625
22.90	4.79	1.050	2.506
21.25	4.61	1.025	2.446
19.70	4.44	0.980	2.339
26.10	5.11	1.130	2.697
28.60	5.35	1.180	2.816
27.50	5.24	1.150	2.745
9.61	3.10	0.710	1.695
8.64	2.94	0.670	1.599
7.80	2.79	0.630	1.504

$$D_{Fe(CN)_6^{-3}} = 6.20 \times 10^{-6}\ cm^2/sec$$

Table III

Diffusion Coefficients

Component	D	Supporting Electrolyte	Reference
$K_4Fe(CN)_6$	$5.0 \times 10^{-6} \frac{cm^2}{sec}$	1.0 M KCl	5
$K_3Fe(CN)_6$	$7.0 \times 10^{-6} \frac{cm^2}{sec}$	1.0 M KCl	5
$K_4Fe(CN)_6$	$4.9 \times 10^{-6} \frac{cm^2}{sec}$	0.5 M K_2SO_4	5
$K_3Fe(CN)_6$	$7.2 \times 10^{-6} \frac{cm^2}{sec}$	0.5 M K_2SO_4	5
$K_3Fe(CN)_6$	$5.8 \times 10^{-6} \frac{cm^2}{sec}$	2 N NaOH	2

From the Translating Electrode

$K_4Fe(CN)_6$	$5.15 \times 10^{-6} \frac{cm^2}{sec}$	1.0 M KCl
$K_3Fe(CN)_6$	$6.20 \times 10^{-6} \frac{cm^2}{sec}$	1.0 M KCl

Table IV

Amplitude of Current Fluctuations

Cylinder Size	Speed (rpm)	Current (ma)	$\frac{\Delta i}{i} \times 100$
1"	82.8	0.73	19.1
	35.7	0.45	16.7
	12.9	0.28	14.3
	52.2	0.52	19.2
	17.1	0.32	18.8
	20.4	0.35	14.3
3/4"	10.9	0.89	11.2
	61.5	0.66	13.6
	22.2	0.40	11.2
	85.7	0.79	15.2
1/4"	129.0	0.98	3.1
	50.8	0.61	3.3
	22.2	0.40	5.5
	35.3	0.51	5.3
1/8"	131.0	2.0	2.5
	118.0	1.83	2.7
	24.2	0.80	3.8
	5.35	0.42	5.2

where $\Delta i = i_{max} - i_{min}$

B. Heat and Mass Transfer From the Surface of a Cylinder with Discontinuous Boundary Conditions to an Incompressible Laminar Flow

(See Supplement No. 1 accompanying this report.)

References

1. Acrivos, A., "The Asymptotic Form of the Laminar Boundary-Layer Mass-Transfer Rate for Large Interfacial Velocities," J. Fluid Mech. 12, 337 (1962)
2. Bopp, G.R., "Electrode Kinetics and Diffusion Using a Translating Electrode," Advanced Research Projects Agency Contract Af 49(638)1123, Supplement No. II, (October, 1963)
3. Grassmann, P., Ibl, N., Trüb, J., "Elektrochemische Messung von Stoffübergangszahlen." Chemie-Ingenieur-Technik 8, 529-533 (1961)
4. Levich, F.G., Physicochemical Hydrodynamics, Prentice-Hall, Inc., Englewood Cliffs, N.J. (1962)
5. Schlichting, H., Boundary Layer Theory, McGraw-Hill Book Co., Inc., New York, (1955)
6. John, D., Vulstich, W., J. Electrochemical Society 109, 849 (1962)

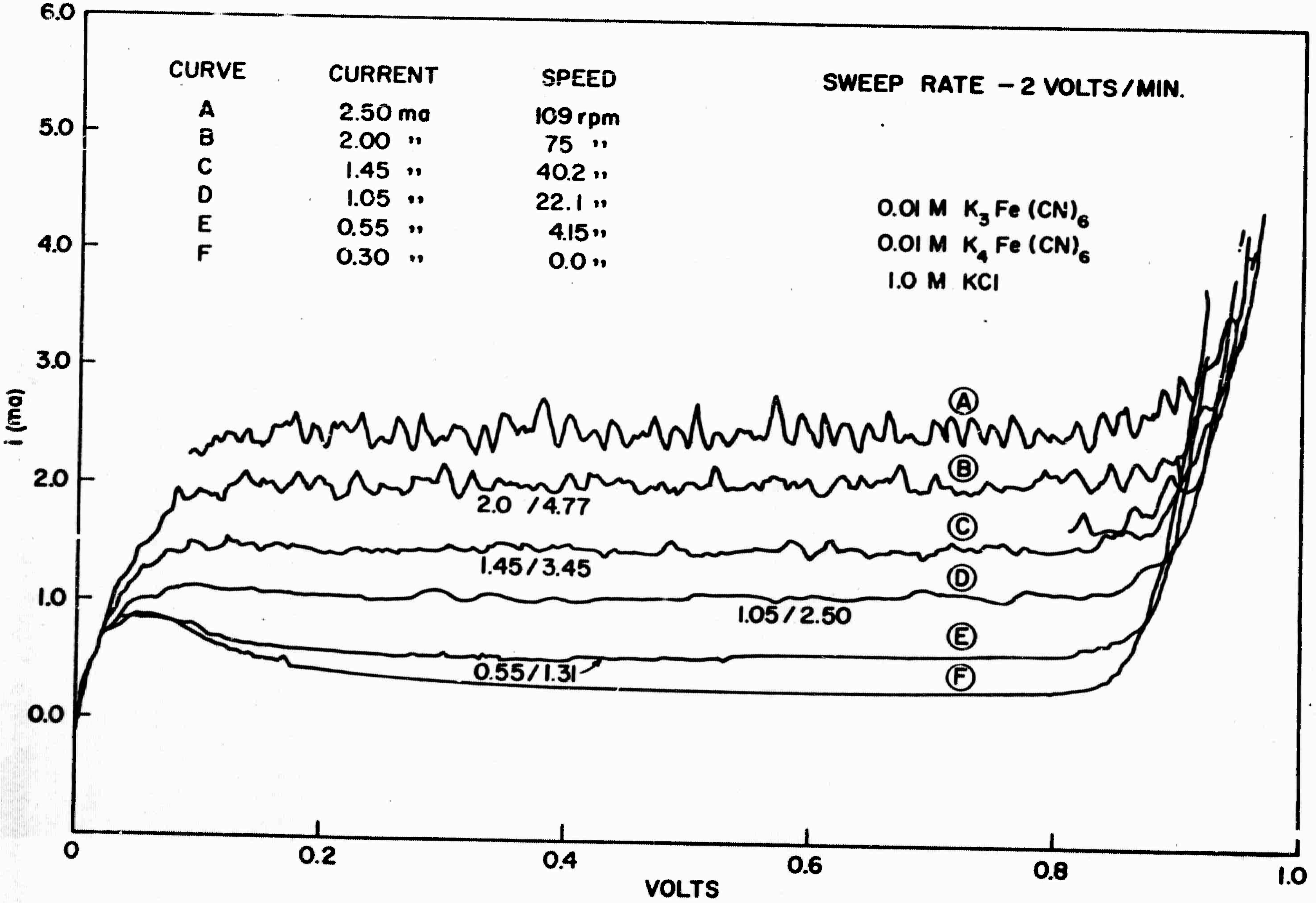

Figure 1 Anodic Polarization Curves at Various Rotational Speeds

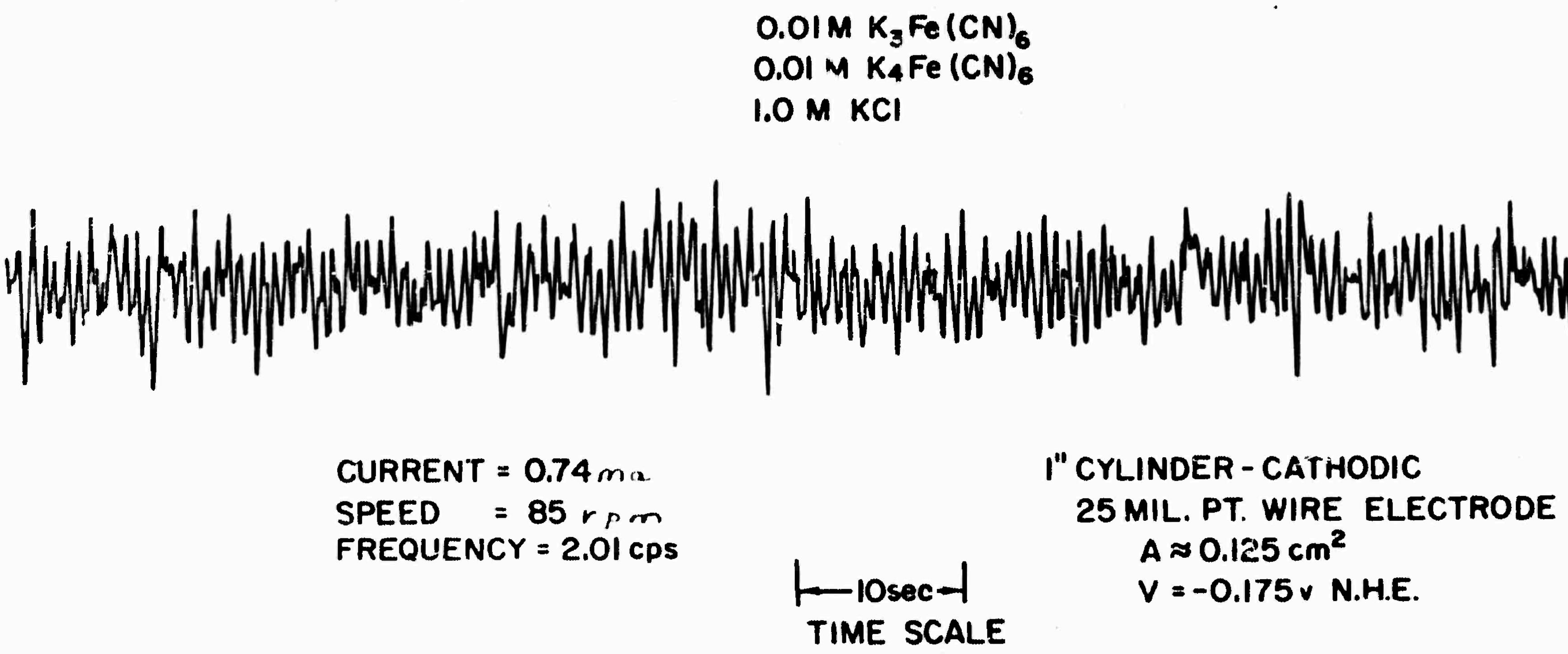

Figure 2 Current Response on the X-Y Plotter at a Sweep Rate of 10 sec per division

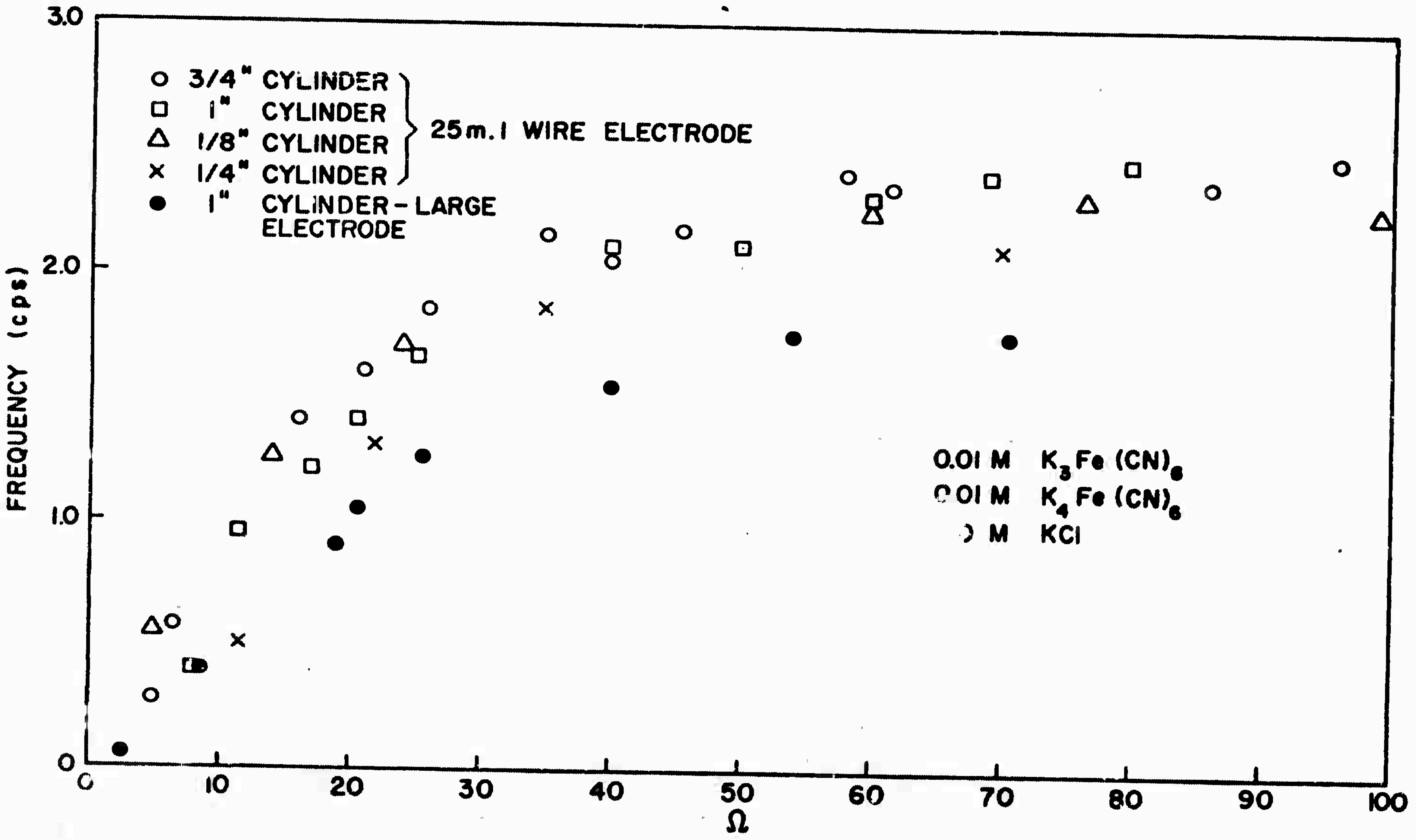

Figure 3 Frequency of Current Fluctuations vs. Rotational Speed

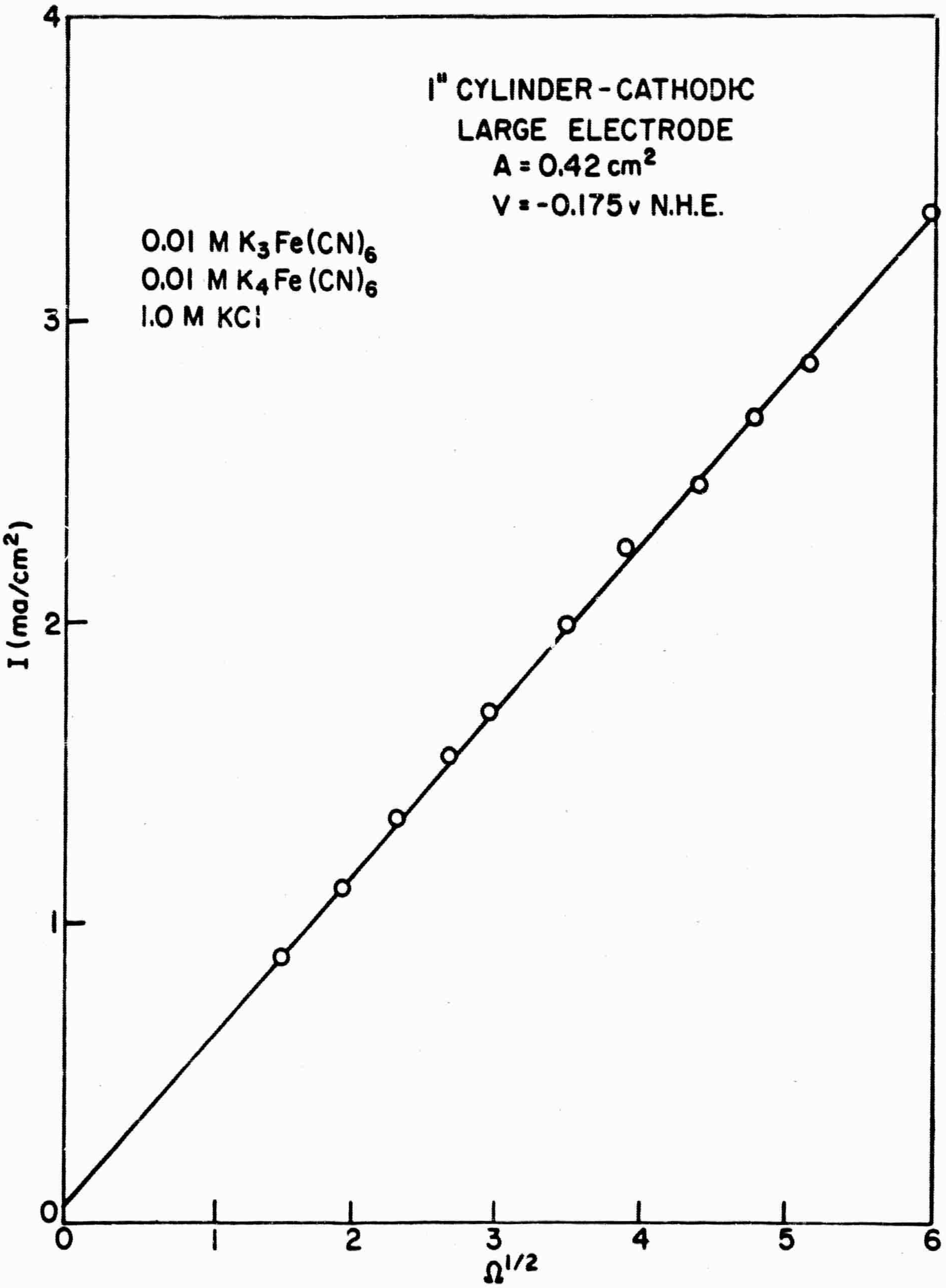

Figure 4 Current Density vs. Square Root of Rotational Speed

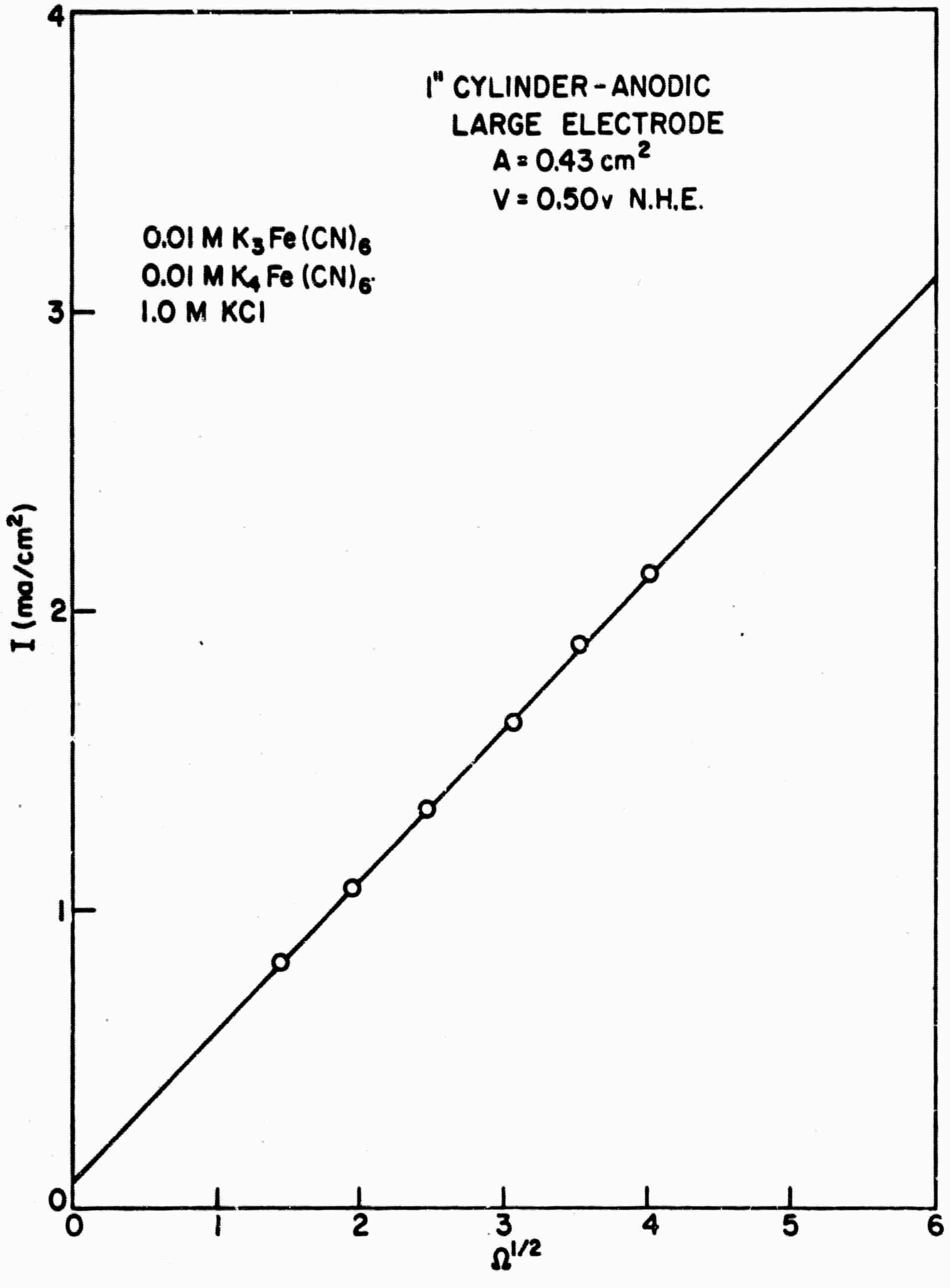

Figure 5 Current Density vs. Square Root of Rotational Speed

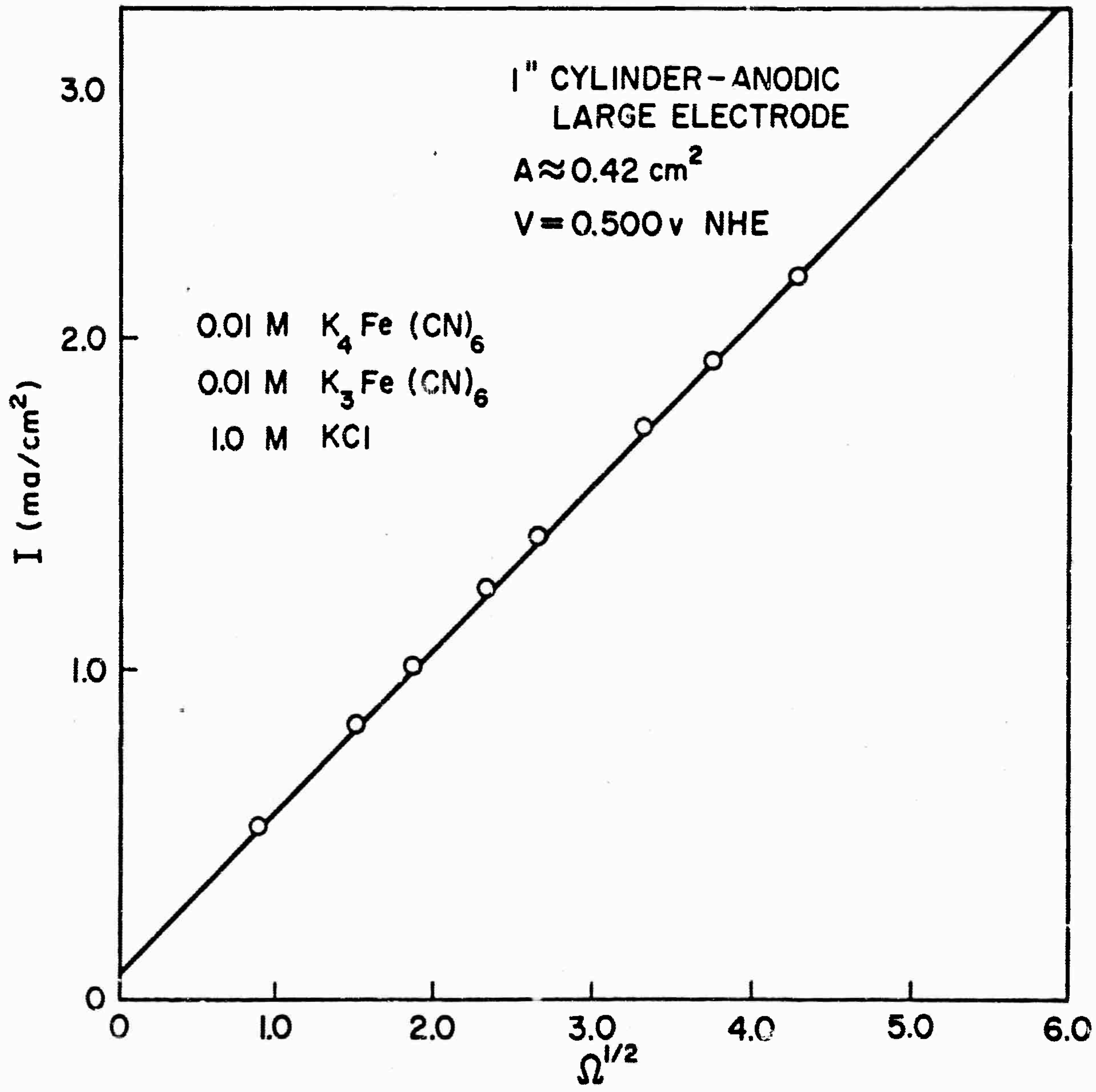

Figure 6 Current Density vs. Square Root of Rotational Speed

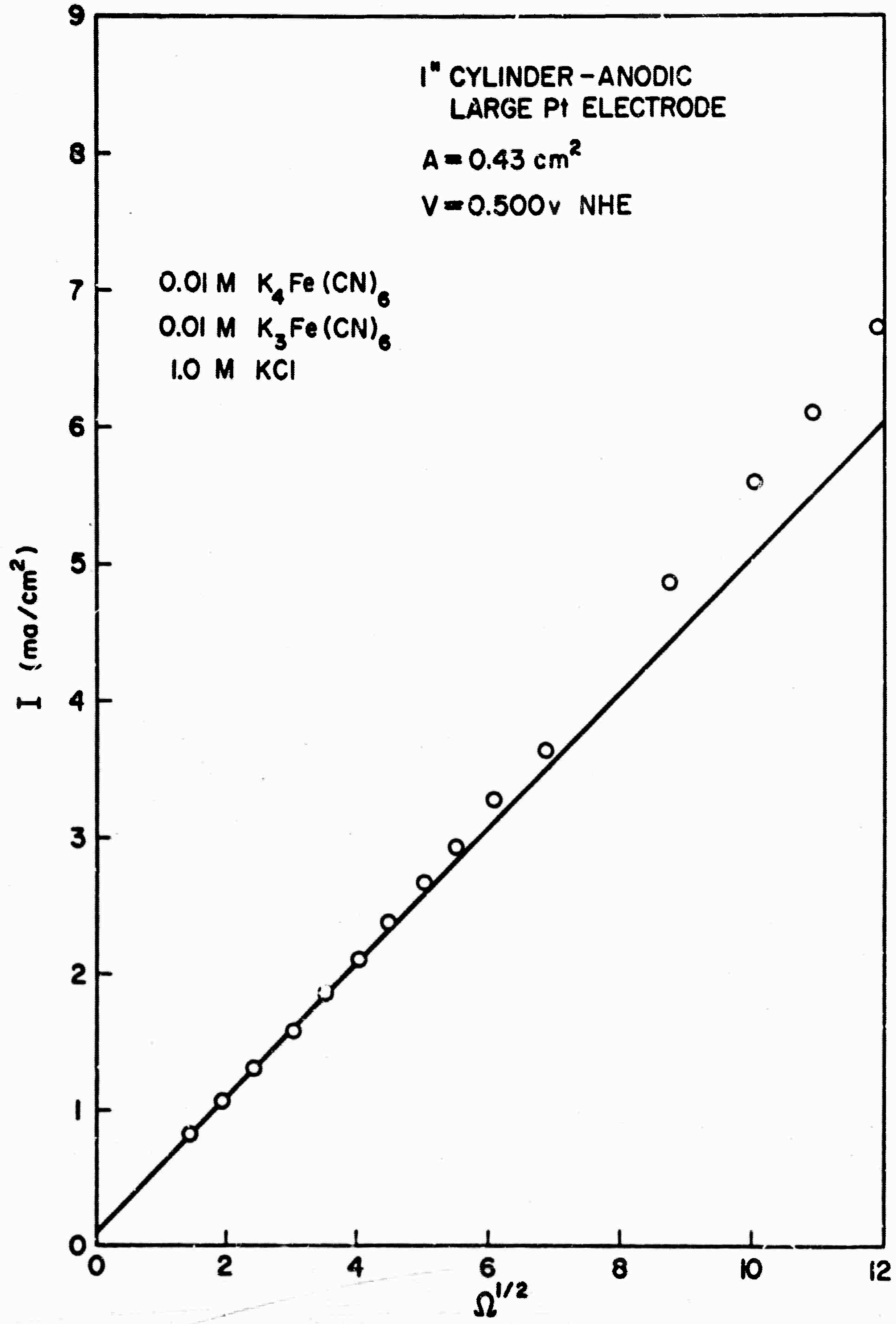

Figure 7 Current Density vs. Square Root of Rotational Speed

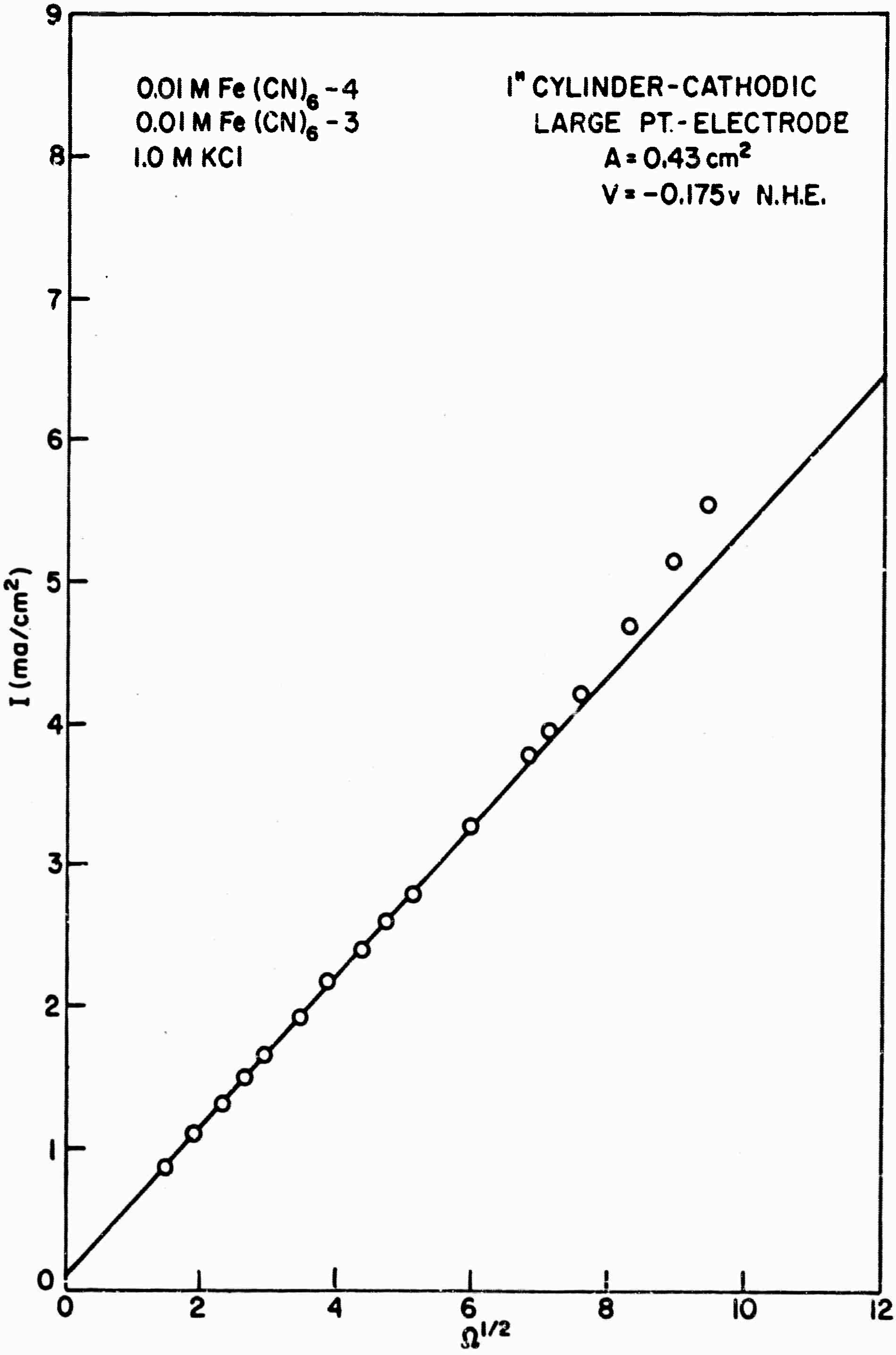

Figure 8 Current Density vs. Square Root of Rotational Speed

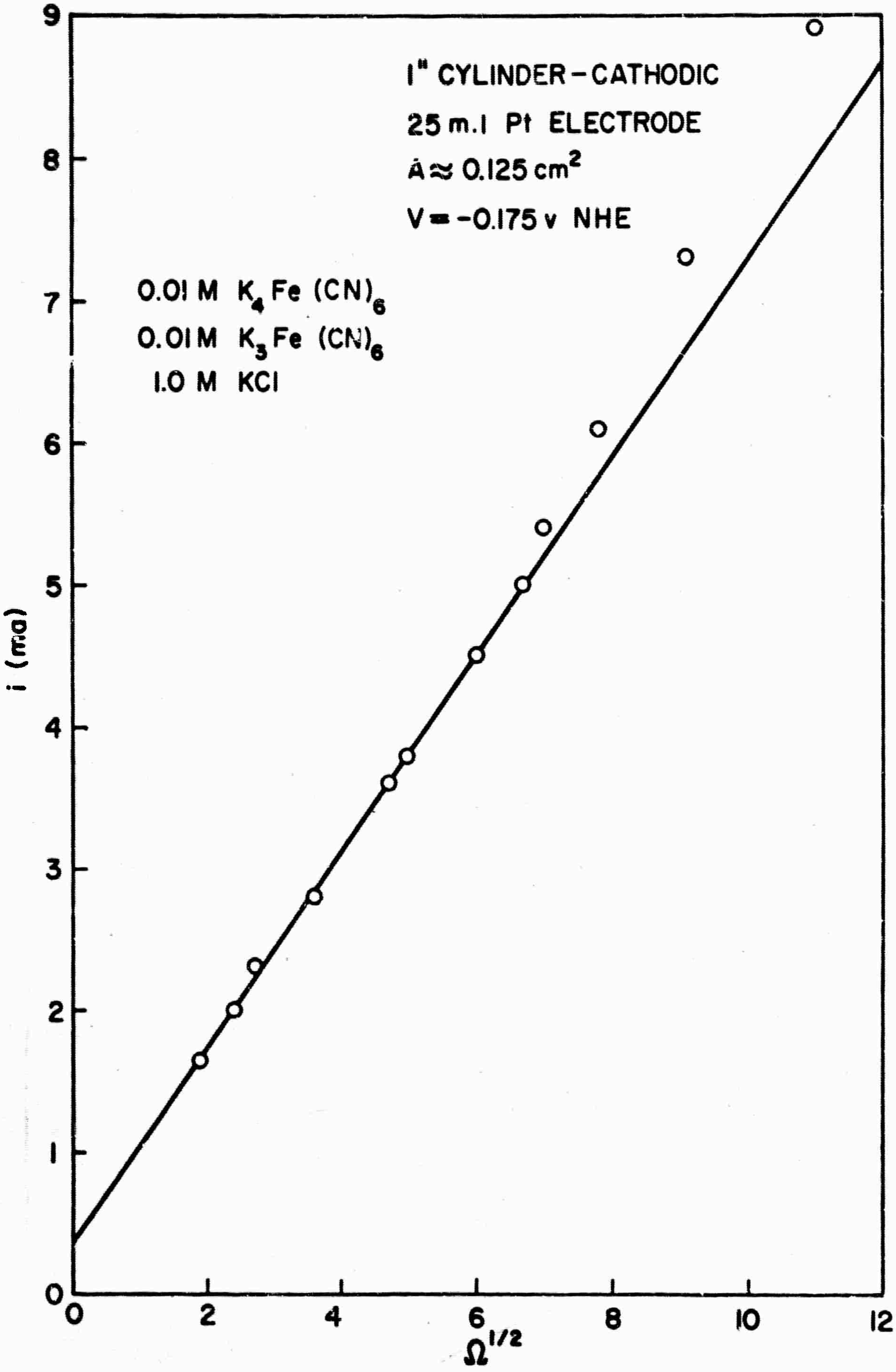

Figure 9 Current vs. Square Root of Rotational Speed

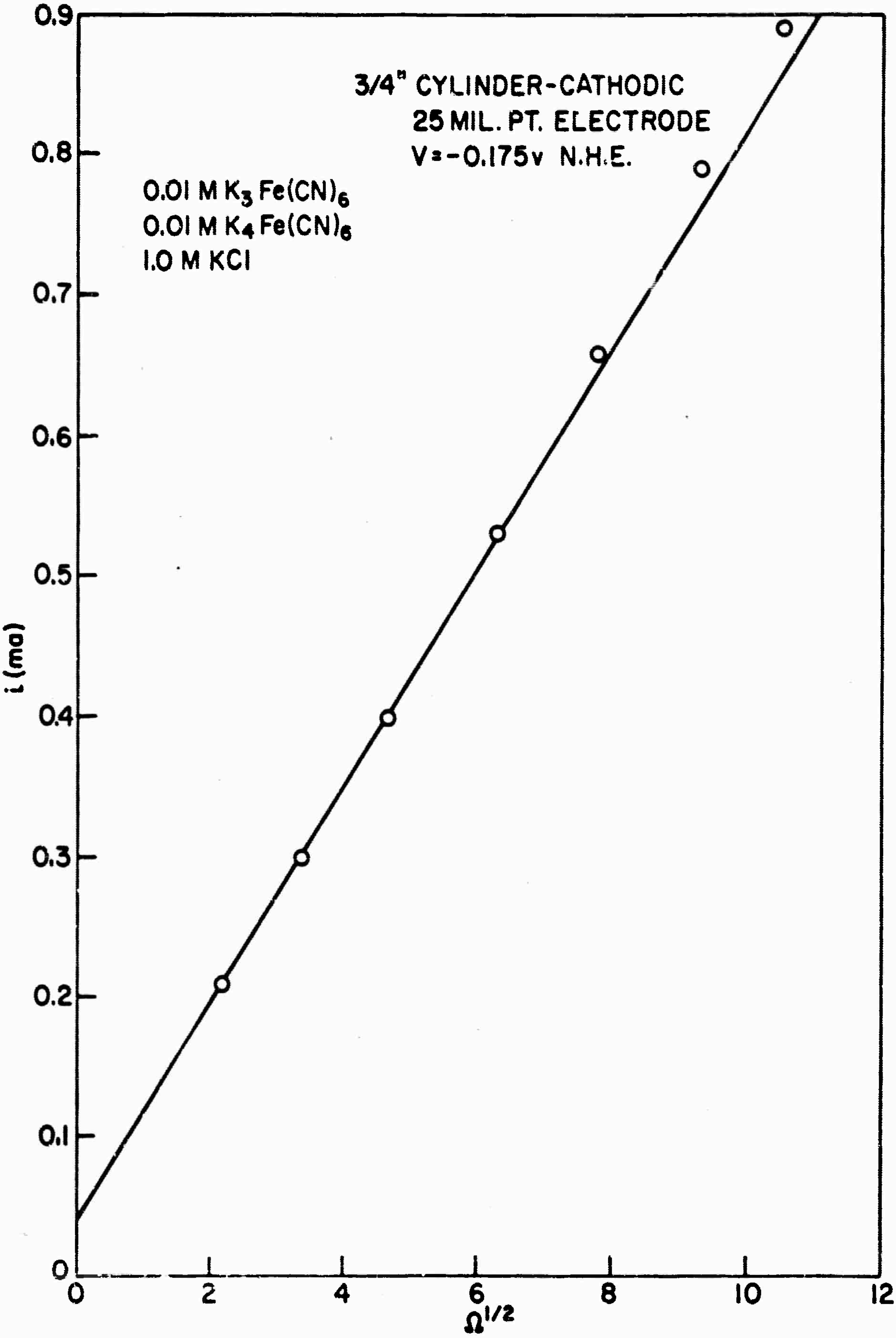

Figure 10 Current vs. Square Root of Rotational Speed

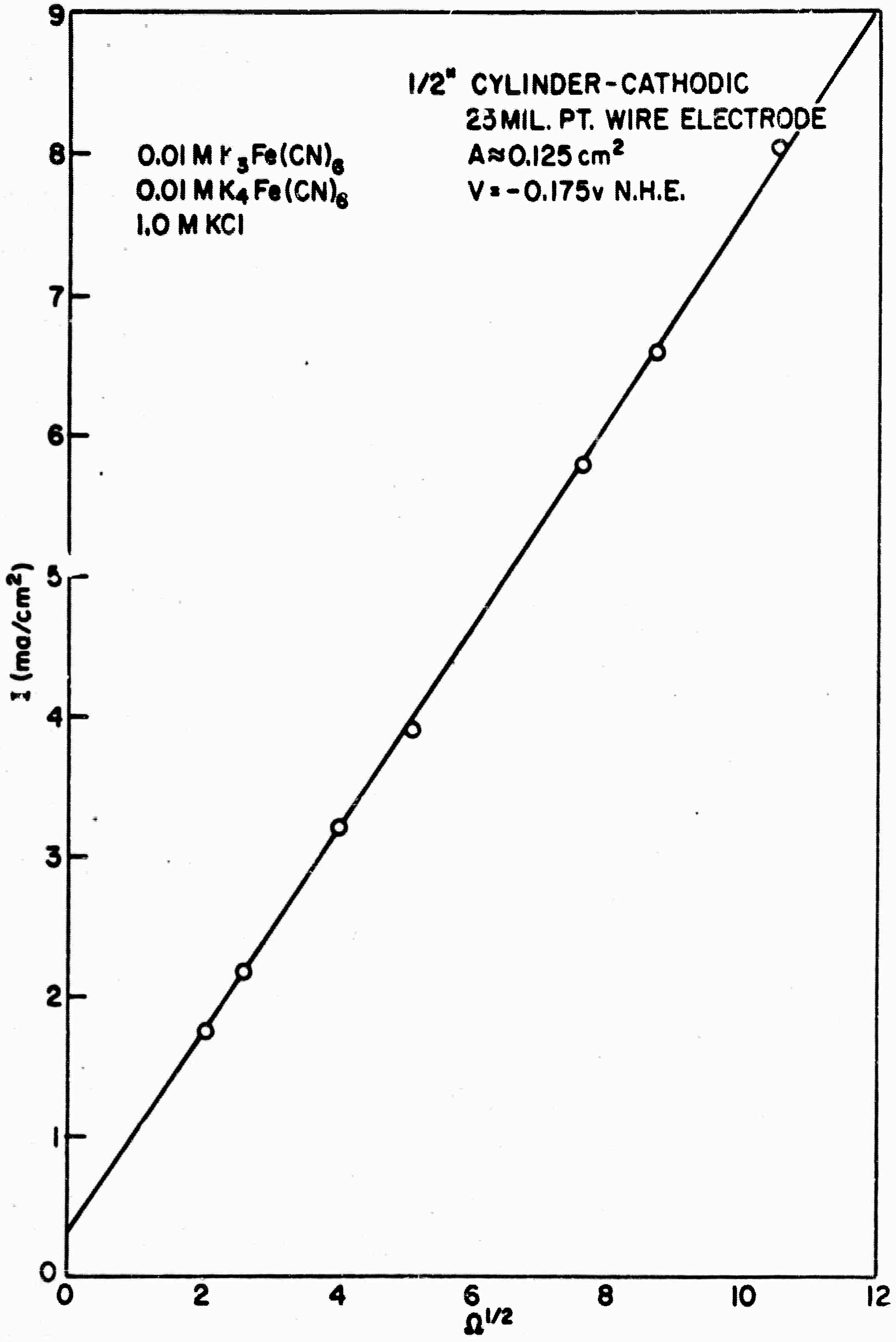

Figure 11 Current Density vs. Square Root of Rotational Speed

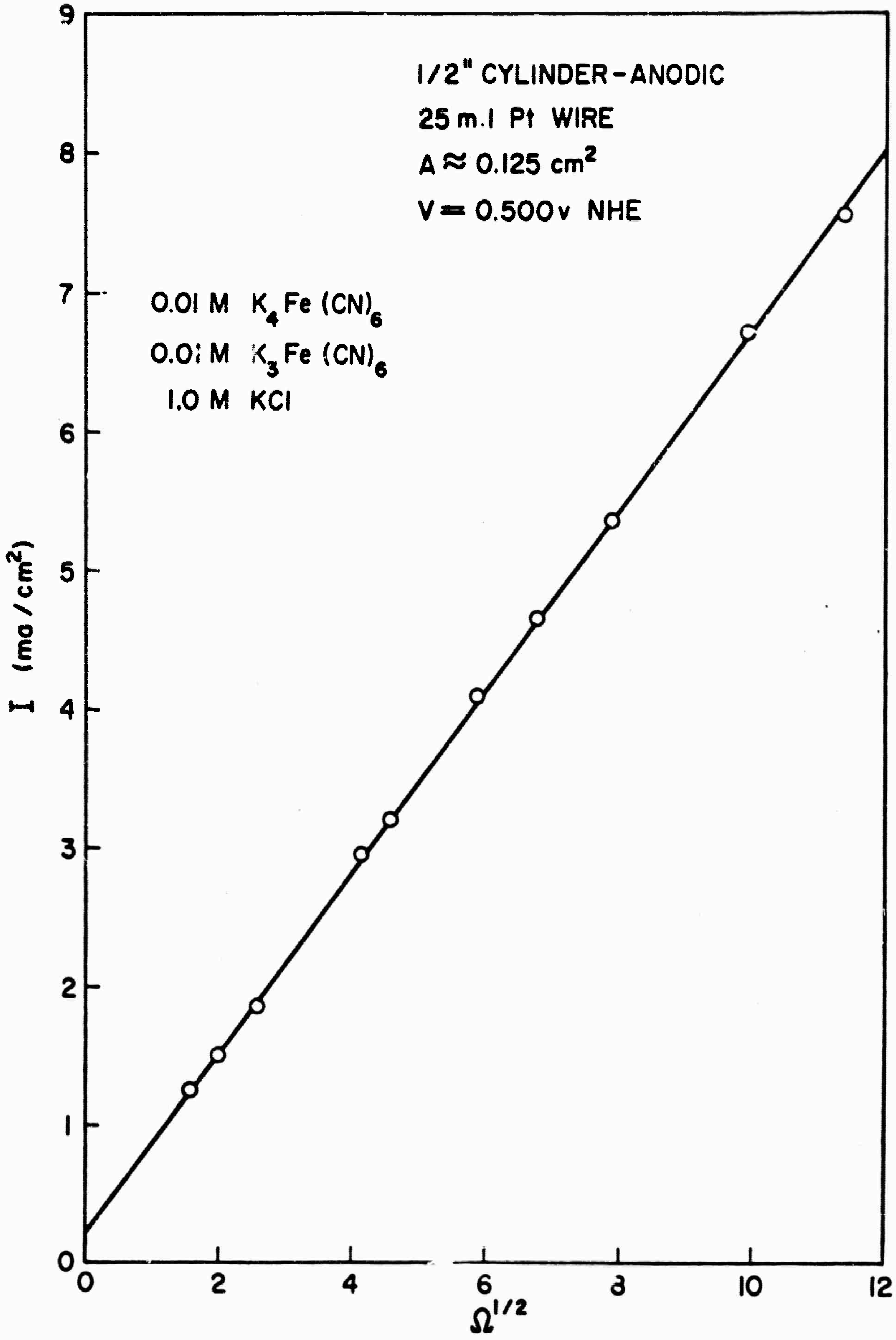

Figure 12 Current Density vs. Square Root of Rotational Speed

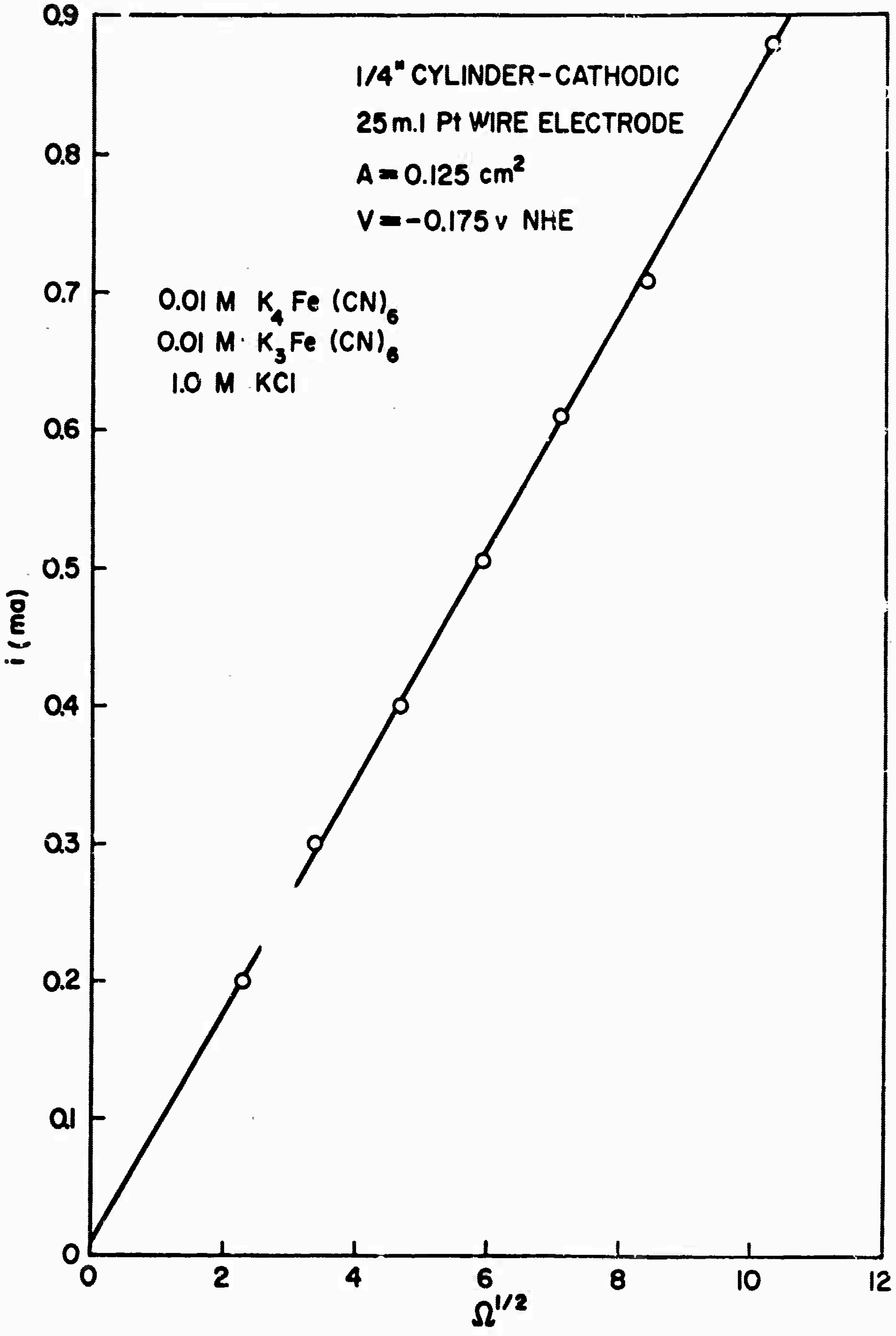

Figure 13 Current vs. Square Root of Rotational Speed

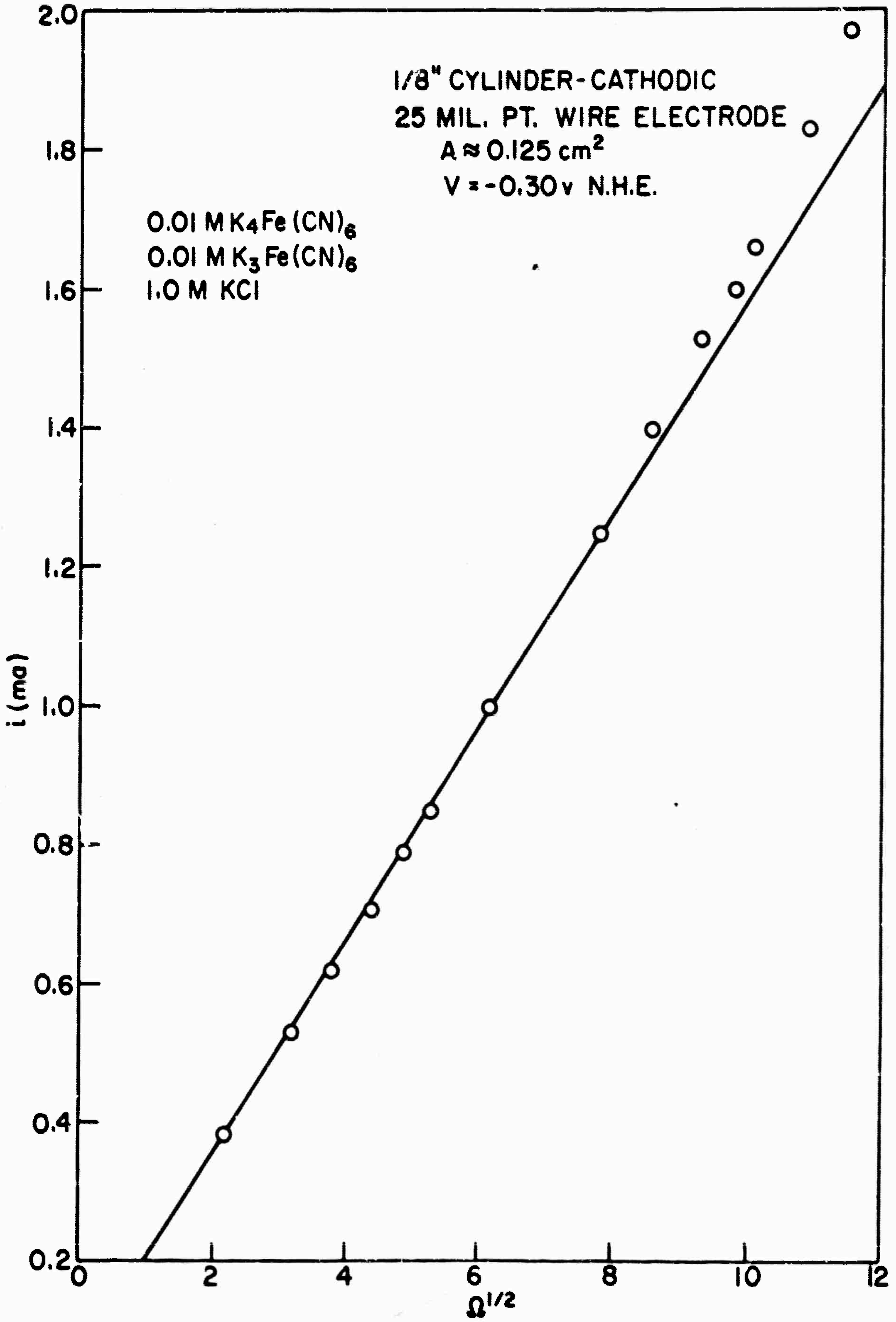

Figure 14 Current vs. Square Root of Rotational Speed

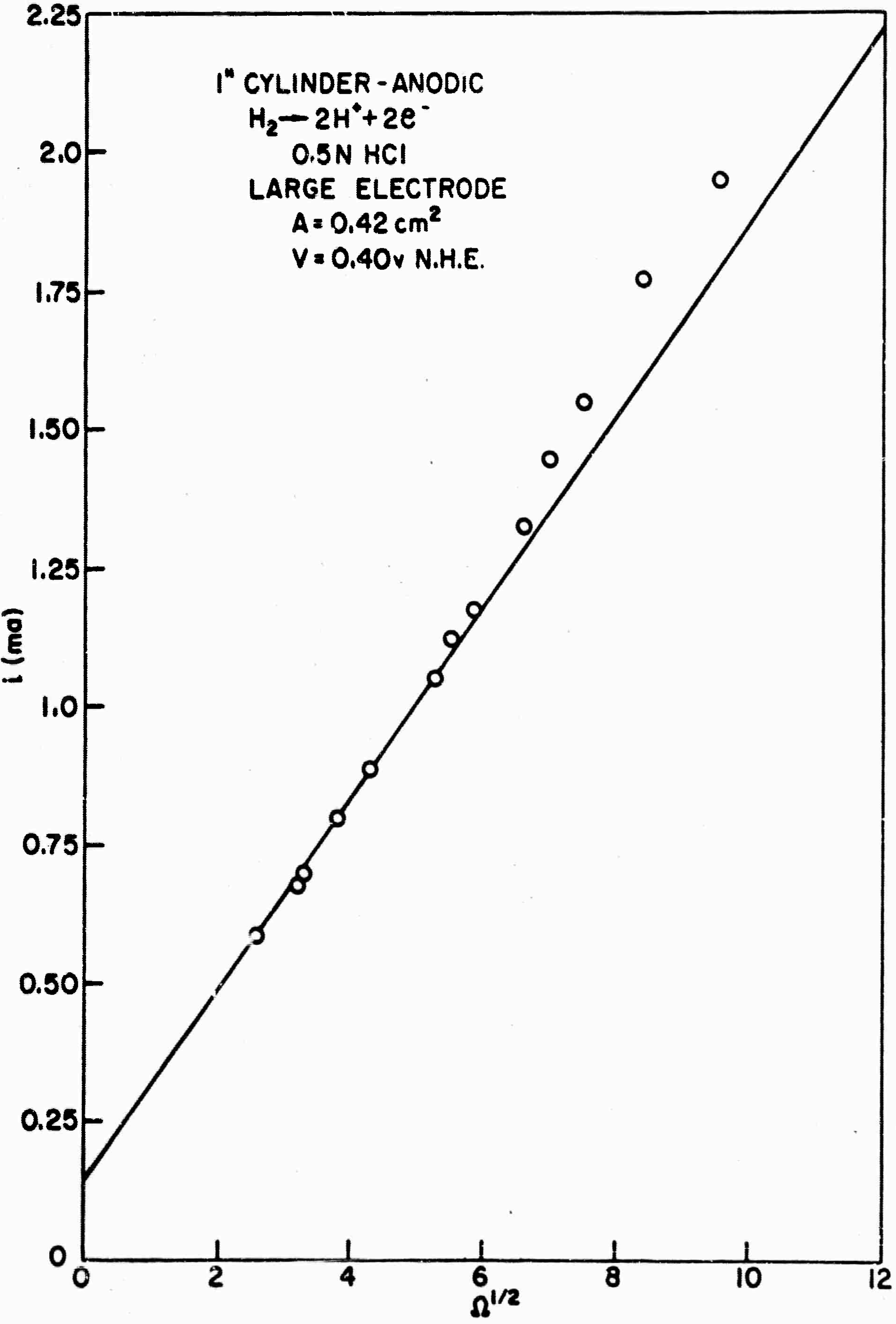

Figure 15 Current vs. Square Root of Rotational Speed

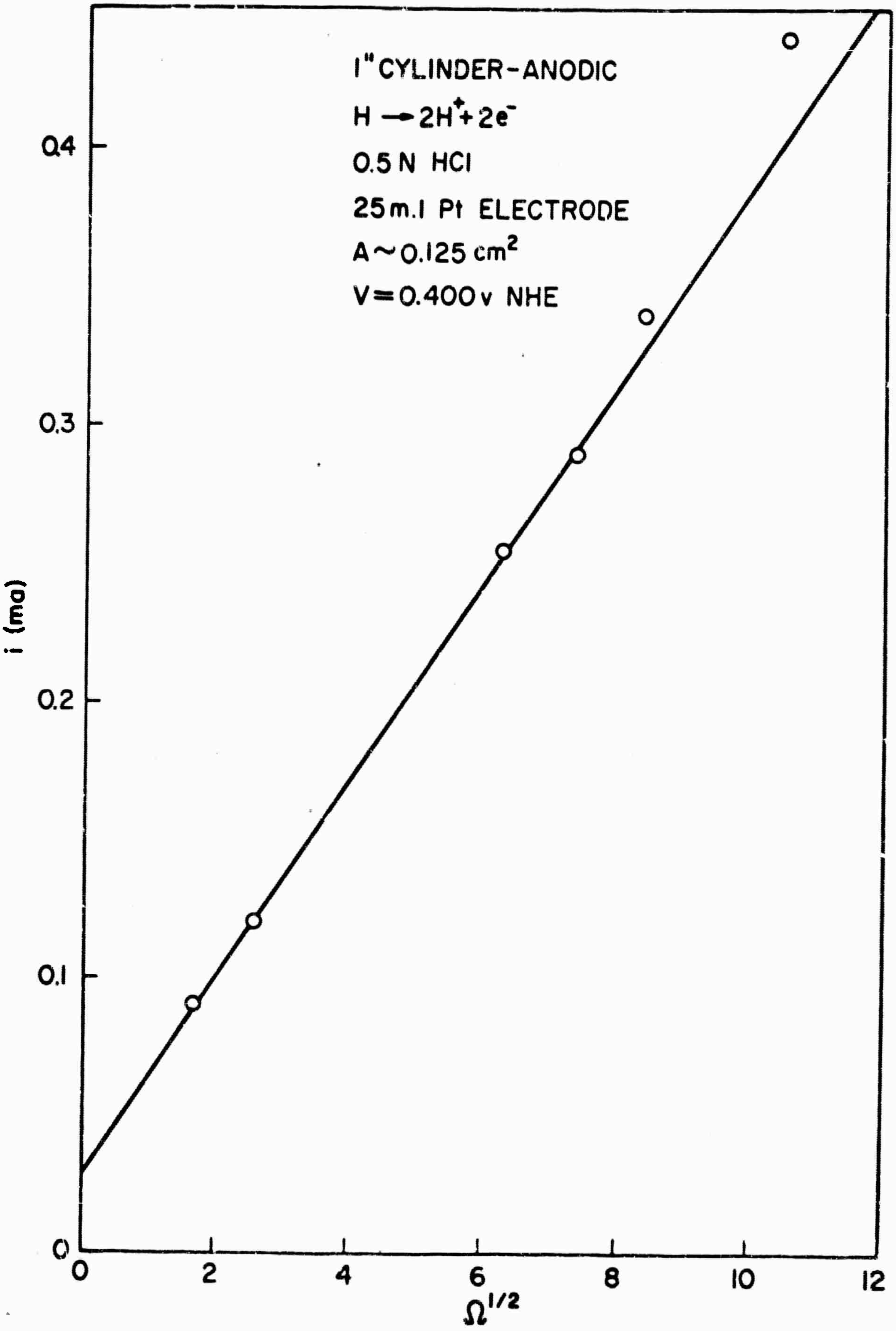

Figure 16 Current vs. Square Root of Rotational Speed